

12

LEVEL III

AD-E 300 664

DNA 5038T

ADA 081 552

# PREDICTIONS OF GPS X-SET PERFORMANCE DURING THE PLACES EXPERIMENT

D. L. Knepp  
R. L. Bogusch  
Mission Research Corporation  
P.O. Drawer 719  
Santa Barbara, California 93102

1 July 1979

Topical Report for Period July 1978—June 1979

CONTRACT No. DNA 001-78-C-0364

APPROVED FOR PUBLIC RELEASE;  
DISTRIBUTION UNLIMITED.

THIS WORK SPONSORED BY THE DEFENSE NUCLEAR AGENCY  
UNDER RDT&E RMSS CODE B322078462 I25AAXHX64202 H2590D.

Prepared for  
Director  
DEFENSE NUCLEAR AGENCY  
Washington, D. C. 20305

DTIC  
ELECTE  
MAR 12 1980  
S D B

80 2 5 363

Destroy this report when it is no longer needed. Do not return to sender.

PLEASE NOTIFY THE DEFENSE NUCLEAR AGENCY,  
ATTN: STTI, WASHINGTON, D.C. 20305, IF  
YOUR ADDRESS IS INCORRECT, IF YOU WISH TO  
BE DELETED FROM THE DISTRIBUTION LIST, OR  
IF THE ADDRESSEE IS NO LONGER EMPLOYED BY  
YOUR ORGANIZATION.



18 DNA, SBIE

UNCLASSIFIED

SECURITY CLASSIFICATION OF THIS PAGE (When Data Entered)

19 REPORT DOCUMENTATION PAGE		READ INSTRUCTIONS BEFORE COMPLETING FORM	
1. REPORT NUMBER DNA 5038T, AD-E300 604	2. GOVT ACCESSION NO.	3. RECIPIENT'S CATALOG NUMBER 9	
4. TITLE (and Subtitle) PREDICTIONS OF GPS X-SET PERFORMANCE DURING THE PLACES EXPERIMENT		5. TYPE OF REPORT & PERIOD COVERED Topical Report for Period July 1978-June 1979	
7. AUTHOR(s) D. L. Knepp R. L. Bogusch		6. PERFORMING ORG. REPORT NUMBER MRC-R-514	8. CONTRACT OR GRANT NUMBER(s) DNA 001-78-C-0364
9. PERFORMING ORGANIZATION NAME AND ADDRESS Mission Research Corporation P.O. Drawer 719 Santa Barbara, California 93102		10. PROGRAM ELEMENT, PROJECT, TASK AREA & WORK UNIT NUMBERS Subtask 125AAXH642-02	
11. CONTROLLING OFFICE NAME AND ADDRESS Director Defense Nuclear Agency Washington, D.C. 20305		12. REPORT DATE 1 July 1979	13. NUMBER OF PAGES 122
14. MONITORING AGENCY NAME & ADDRESS (if different from Controlling Office) 12-123		15. SECURITY CLASS (of this Report) UNCLASSIFIED	
16. DISTRIBUTION STATEMENT (of this Report) Approved for public release; distribution unlimited. 627184			
17. DISTRIBUTION STATEMENT (of the abstract entered in Block 20, if different from Report)			
18. SUPPLEMENTARY NOTES This work sponsored by the Defense Nuclear Agency under RDT&E RMSS Code B322078462 125AAXH64202 H2590D.			
19. KEY WORDS (Continue on reverse side if necessary and identify by block number) NAVSTAR Global Positioning System      Signal Dispersion GPS X-set Receiver                              Pseudonoise Code Tracking Signal Propagation                              Frequency-Selective Effects Signal Scintillation                              Costas Phase Tracking Scintillation Models                              Automatic Frequency Control			
20. ABSTRACT (Continue on reverse side if necessary and identify by block number) Preexperimental predictions of GPS X-set receiver performance during the PLACES barium release experiment are presented for carrier frequencies from 150 to 250 MHz. Detailed examples of the X-set phase, frequency and code tracking performance are shown. For mean carrier power-to-noise density ratios of 35 dB-Hz and less, erroneous Doppler aiding from the AFC/Costas loop can cause degradations to the otherwise adequate code tracking loop. All receiver performance results presented are obtained using numerical multiple			

DD FORM 1 JAN 73 1473 EDITION OF 1 NOV 65 IS OBSOLETE

UNCLASSIFIED SECURITY CLASSIFICATION OF THIS PAGE (When Data Entered)

400 548

over 115

## 20. ABSTRACT (Continued)

phase screen calculations of frequency-selective signal propagation through simulated barium clouds. These calculations are based upon a statistical model of a striated barium cloud developed from Fourier analysis of back-propagation data taken during the STRESS barium release series. This model includes representation of the important barium striation parameters derived from measured power spectral density (PSD) properties including phase standard deviation, spectral index, and outer scale.

## CONTENTS

	PAGE
ILLUSTRATIONS	3
TABLES	6
SECTION 1 - INTRODUCTION	7
1.1 BACKGROUND	7
1.2 APPROACH	9
REFERENCES	13
SECTION 2 - BARIUM CLOUD STRIATION MODEL	14
2.1 BACK-PROPAGATED PHASE	16
2.2 PHASE PSD ANALYSIS	19
2.3 BARIUM CLOUD MODELING VERIFICATION	31
REFERENCES	45
SECTION 3 - PN SPREAD SPECTRUM CODE CORRELATOR	46
3.1 PN CODE TRACKING	47
3.2 THEORETICAL DEVELOPMENT - RECEIVED WAVEFORM	52
3.3 X-SET PN CODE CORRELATION OPERATION	57
3.4 COMPUTATIONAL CONSIDERATIONS	65
REFERENCES	67
SECTION 4 - PROPAGATION AND X-SET PERFORMANCE	68
4.1 NUMERICAL BARIUM CLOUD MODEL	69
4.2 SIGNAL PROPAGATION	72
4.2.1 Propagation Results	72
4.2.2 Frequency-Selective Propagation Results	89
4.3 X-SET PERFORMANCE RESULTS	96
4.3.1 Receiver Design Parameters	96
4.3.2 X-Set Performance at 150 MHz	100

	PAGE
SECTION 4 - PROPAGATION AND X-SET PERFORMANCE (continued)	
4.3.3 X-Set Performance at 200 MHz	112
4.3.4 Summary of X-Set Performance	112
REFERENCES	114
SECTION 5 - SUMMARY AND RECOMMENDATIONS	115
REFERENCES	116

ACCESSION for		
NTIS	White Section	<input checked="" type="checkbox"/>
DDC	Buff Section	<input type="checkbox"/>
UNANNOUNCED		<input type="checkbox"/>
JUSTIFICATION _____		
BY _____		
DISTRIBUTION/AVAILABILITY CODES		
Dist.	Avail. and/or	SPECIAL
A		

## ILLUSTRATIONS

FIGURE		PAGE
2-1.	Back-propagated phase for Esther pass 10.	20
2-2.	Deterministic part of the back-propagated phase for Esther pass 10.	22
2-3.	Random component of the back-propagated phase for Esther pass 10.	23
2-4.	Power spectral density of the random component of the back-propagated phase for Esther pass 10.	24
2-5.	Power spectral density of the random component of the back-propagated phase for Esther pass 17.	27
2-6.	Power spectral density of the random component of the back-propagated phase for Fern pass 9.	28
2-7.	Phase screen generated numerically to model Esther pass 10.	32
2-8.	Experimentally measured received signal amplitude during Esther pass 10.	34
2-9.	Portion of the numerically generated signal amplitude after propagation through the phase screen of Figure 2-7.	35
2-10.	Experimentally measured signal phase corresponding to signal amplitude shown in Figure 2-8	36
2-11.	Numerically generated signal phase corresponding to signal amplitude shown in Figure 2-9.	37
2-12.	Back-propagated phase for Fern pass 9.	38
2-13.	Phase screen generated numerically to model Fern pass 9.	39
2-14.	Experimentally measured received signal amplitude during Fern pass 9.	41
2-15.	Portion of the numerically generated signal amplitude after propagation through the phase screen of Figure 2-13.	42
2-16.	Experimentally measured signal phase corresponding to signal amplitude shown in Figure 2-14.	43

FIGURE		PAGE
2-17.	Numerically generated signal phase corresponding to signal amplitude shown in Figure 2-15.	44
3-1.	Envelope of the PN code autocorrelation function, infinite bandwidth, no scintillation or dispersion.	47
3-2.	PN code autocorrelation function in a no-selective fading environment.	49
3-3.	PN code autocorrelation function in a frequency-selective environment.	50
3-4.	X-set AFC/Costas loop implementation.	58
3-5.	X-set PN code tracking loop implementation.	59
3-6.	Simplified block diagram of code correlator operation and I-Q sampling.	60
4-1.	Phase screen representation of Esther at 150 MHz with no deterministic barium cloud.	73
4-2.	Signal amplitude and phase at a propagation distance of 1 km.	75
4-3.	Signal amplitude and phase at a propagation distance of 4 km.	76
4-4.	Signal amplitude and phase at a propagation distance of 10 km.	77
4-5.	Signal amplitude and phase at a propagation distance of 30 km.	78
4-6.	Signal amplitude and phase at a propagation distance of 50 km.	79
4-7.	Signal amplitude and phase at a propagation distance of 100 km.	80
4-8.	Signal amplitude and phase due to deterministic Esther barium cloud at 150 MHz.	82
4-9.	Signal amplitude for complete model of Esther at a frequency of 150 MHz.	83
4-10.	Signal amplitude for complete model of Esther at a frequency of 200 MHz.	84
4-11.	Signal amplitude for complete model of Esther at a frequency of 250 MHz.	85
4-12.	Signal amplitude for complete model of Fern at a frequency of 150 MHz.	86
4-13.	Signal amplitude for complete model of Fern at a frequency of 200 MHz.	87

FIGURE		PAGE
4-14.	Signal amplitude for complete model of Fern at a frequency of 250 MHz.	88
4-15.	PN code correlator output envelope for Esther at a carrier frequency of 150 MHz (inner scale of 0.58 m).	90
4-16.	PN code correlator output envelope for Esther at a carrier frequency of 150 MHz (inner scale of 10 m).	92
4-17.	PN code correlator output envelope for Esther at a carrier frequency of 150 MHz.	94
4-18.	PN code correlator output envelope for Esther at a carrier frequency of 200 MHz.	95
4-19.	Received signal amplitude and phase for Esther at a carrier frequency of 150 MHz.	101
4-20.	Esther at 150 MHz: phase tracking error time history.	102
4-21.	Esther at 150 MHz: AFC/Costas loop Doppler frequency estimate.	103
4-22.	Esther at 150 MHz: PN code loop time delay estimate.	104
4-23.	Esther at 150 MHz: X-set code correlator amplitude time history.	107
4-24.	Esther at 150 MHz: PN code envelope and code tracking history for simulation time from 6.60 to 7.33 seconds.	108
4-25.	Esther at 150 MHz: PN code envelope and code tracking history for simulation time from 10.26 to 10.99 seconds.	109
4-26.	Esther at 150 MHz: PN code envelope and code tracking history for simulation time from 13.93 to 14.66 seconds.	110

## TABLES

TABLE		PAGE
2-1.	PSD measurements for STRESS events.	26
4-1.	Barium cloud parameters used in predictions for the PLACES experiment.	70
4-2.	Nominal design values used in X-set simulation.	97

## SECTION 1 INTRODUCTION

### 1.1 BACKGROUND

The objective of the proposed PLACES<sup>\*</sup> barium release experiment is to help determine the effects of propagation disturbances produced by striated plasma regions on the performance of phase-coherent satellite systems, with emphasis on the Global Positioning System (GPS). To relate experimental results as directly as possible to GPS receiver performance, one would prefer tests using actual GPS L-band navigation signals if interesting levels of propagation disturbances could be produced in the field experiment. In this context "interesting" means disturbance levels comparable to those expected in nuclear environments. Previous calculations of propagation disturbances (Reference 1-1) predict that GPS L-band signals are likely to be driven into saturated Rayleigh-like scintillation in striated nuclear environments. It is interesting to note that a Wideband Satellite pass at Ancon on 30 March 1977 shows that saturated L-band scintillation is occasionally observed in the equatorial ionosphere (Reference 1-2). Significant UHF scintillation was produced by STRESS barium releases (Reference 1-3). However, it is unlikely that significant scintillation will occur at L-band in barium clouds. Thus it is natural to consider the use of somewhat lower frequencies in the PLACES experiment.

---

\* PLACES is the acronym for Position Location and Communication Effects Simulation.

Because of the wide bandwidth GPS pseudo-noise spread-spectrum navigation signals, selection of an appropriate frequency requires consideration of frequency-selective propagation mechanisms including angular scattering, dispersive effects, fading spectra and scintillation intensity. These disturbances are functions of the spectra of the ionization irregularity structures, as well as propagation geometry, frequency, and signal spectrum. For example, integrated phase variance is sensitive to the effective outer scale size, whereas angular scattering is sensitive to the effective inner scale size (which may be limited by the receiver antenna aperture). Scintillation intensity is sensitive to the magnitude of the irregularity spectrum near the Fresnel size, which depends on frequency and propagation geometry. The point here is that the potential propagation disturbances are sufficiently numerous and their relationships to plasma properties sufficiently complicated to warrant detailed calculations to establish proper scaling with carrier frequency and signal spectrum.

## 1.2 APPROACH

The goal of this report is to provide pre-experimental predictions of the GPS X-set receiver performance after signal propagation through a disturbed barium environment. This goal is accomplished here through the following steps:

1. A detailed statistical model for a striated barium cloud is developed based on back-propagated results provided by ESL, Inc., from measurements made during the STRESS test series. As discussed in Section 2, measurements made during three aircraft passes beneath the striated STRESS barium clouds are analyzed to obtain the integrated phase power spectral density (PSD) including rms phase fluctuations, outer scale size, and spectral index.
2. This statistical model is utilized to obtain frequency-selective multiple phase screen (MPS) calculations of signal propagation over signal bandwidths required for the GPS pseudo-noise spread-spectrum navigation signals. Carrier frequencies range from 150 to 250 MHz.
3. The previously existing GPS X-set receiver simulation was modified to include the received signal spectrum and the receiver code correlation operation. As discussed in Section 3, these modifications are the only changes in the receiver simulation required for frequency-selective effects.
4. The frequency-selective propagation calculations called out in Item 2 above are then used as direct input to the X-set receiver simulation to measure the receiver performance after signal propagation through a barium environment. In Section 4 the frequency-selective propagation results and the X-set receiver performance characteristics are discussed.

It is important to note that all results presented in this report are based on the detailed X-set receiver simulation discussed in Reference 1-1. This simulation is a direct, sampled-data digital implementation of the GPS X-set receiver initially designed by Cahn (Reference 1-4) and described in Reference 1-5. With the exception of a reduced carrier frequency and restoration of the 250/sec AFC/Costas iteration rate, it is assumed that there are no changes in the X-set design. Thus even with a carrier frequency as low as 150 MHz, it is assumed that the PN code chip rate remains at the nominal value of 10.23 Mbps. This assumption is important for the interpretation of both experimental and simulation results for receiver performance in terms of actual GPS performance in a nuclear environment. An unmodified receiver allows for a direct study of GPS X-set operation in a nuclear environment. Of course, if receiver modifications were instituted (for example, a lower code chip rate), the numerical simulations could be easily modified accordingly.

Step 1, above, involves the analysis of data taken from three aircraft passes in the shadow of two barium clouds, Esther and Fern. The coherently received aircraft data was then numerically back-propagated\* to the point where amplitude scintillations were minimal at the barium cloud locations. The phase of the signal at this location can then be directly interpreted as electron-density fluctuations integrated along the line of sight through the barium cloud. This phase was then detrended and Fourier analyzed to obtain measurements of integrated electron-density power spectra, including spectral index, phase standard deviation, and outer scale.

The integrated electron-density power spectral density (PSD) is then used as the basis of a statistical model of barium cloud striations. The model includes a large gaussian shape to represent the mean or deterministic (unstriated) portion of a barium cloud plus a random part based, in part, on the measured PSD parameters discussed above. The inner scale is included as

---

\* Dr. C. W. Prettie of ESL, Inc., provided the back-propagation results.

an additional adjustable parameter. Inclusion of the large gaussian profile to represent the mean barium cloud, while providing a good model of the actual barium propagation environment, causes difficulty in interpretation of the propagation results and related receiver simulation results because of the inhomogeneous propagation environment. For this reason, some simulations were made without the deterministic portion of the barium cloud model. In Section 4 propagation results are presented which show the effect of both the deterministic and random portions of the model.

The receiver simulation here is a direct digital implementation of the X-set receiver and includes implementation of the local reference generator/correlator and signal conditioner, AFC/Costas carrier loop, PN code loop, AGC loop, and rate multiplier/incremental phase modulators. Also included are time-shared PN code tracking and data demodulation and decoding. This digital simulation approach provides the only practical method of accurately analyzing the operation of complex nonlinear receivers in the presence of signal propagation disturbances.

No effort is made in this work to simulate the operation of the GPS navigation data processing system. Rather, we limit consideration to the study of an X-set receiver operating in a disturbed barium environment—that is, only propagation disturbances on a single channel of the navigation processor are considered. To determine the effects of disturbed propagation paths on the GPS navigation processor, our X-set receiver model would have to be incorporated into a larger simulation which included navigation data processing.

In Section 4 of this report several detailed examples of X-set receiver operation at a carrier frequency of 150 MHz are presented. These examples graphically illustrate the phase, frequency, and code tracking performance of the X-set operating in a striated barium environment.

Work is currently in progress to relate propagation results presented in this report to analytical results for mean signal arrival time, time delay jitter and pulse broadening of the received waveform. These issues will be addressed in a separate report.

## REFERENCES

- 1-1. Bogusch, R. L., and D. L. Knepp, Propagation Effects on GPS Receiver Model X, Mission Research Corporation, January 1978 (Unpublished).
- 1-2. Fremouw, E. J., R. L. Leadabrand, R. C. Livingston, M. D. Cousins, C. L. Rino, B. C. Fair, and R. A. Long, "Early Results from the DNA Wideband Satellite Experiment," Radio Science, 13, pp. 167-188, 1978.
- 1-3. Prettie, C. W., and J. M. Marshall, "Satellite Link Measurements" in Proceedings of the STRESS Data Review Meeting, 29-30 November 1977, DNA 4620T, SRI International, Compiled by D. R. McDaniel, June 1978.
- 1-4. Cahn, C. R., A Composite AFC/Costas Loop for Transition Between Frequency and Phase Tracking, Magnavox Research Laboratories Technical Report, MX-TM-3165-75, 24 January 1975.
- 1-5. Stonestreet, W. M., A Functional Description of the NAVSTAR GPS Receiver Model X, R-981, The Charles Stark Draper Laboratory, Inc., Final Report for SAMS0 Contract F04701-75-C-0212, Volume I, 26 April 1976, Revised February 1977.

## SECTION 2

### BARIUM CLOUD STRIATION MODEL

The multiple phase screen (MPS) propagation simulation provides a numerical solution for the propagation of a plane wave through a disturbed environment characterized by index-of-refraction fluctuations. By modeling a barium cloud as a random phase screen, it is possible to use the simulation to generate signal realizations which serve as direct input to the GPS X-set receiver simulation.

This section describes the barium cloud striation models which were developed to serve as input to the MPS propagation simulation. Results for the equivalent phase (integrated electron-density) power spectral density (PSD), outer scale, and spectral index are presented. Under the assumption of a 10 km propagation distance through the striated barium cloud, values of the rms electron-density fluctuation are also given.

The multiple phase screen propagation simulation represents the disturbed region by a number of phase screens located between the satellite and the receiver. Random phase fluctuations in each screen are generated using the statistical properties of the electron-density fluctuations as determined by the electron-density power spectral density. A wave (initially plane as it enters the disturbed region) is then propagated numerically from one screen to the next by use of the Fresnel-Kirchhoff integral equation until a solution is obtained for the complex electric field in the receiver plane. This technique is equivalent to a solution of the parabolic wave equation and is thus able to account for multiple scattering (Reference 2-1). Since the phase screens are random, the signal propagated to the

receiver is random and, if desired, statistical results may be obtained by averaging a number of different simulations, each based on a different sequence of random numbers.

The random phase screens are chosen in a statistical manner and are characterized by a phase power spectral density (PSD) identical to the PSD of the electron-density fluctuations integrated along the direction of propagation. For this work, the phase PSD used to represent a striated barium cloud was obtained from analysis of observations taken during the STRESS barium release experiments Esther and Fern (Reference 2-2).

## 2.1 BACK-PROPAGATED PHASE

This section describes a portion of the propagation experiments performed during the STRESS test series which were designed to obtain information on the integrated electron density fluctuations produced by barium clouds. Dr. C. W. Prettie of ESL, Incorporated has kindly provided the back-propagated phase data discussed below.

In order to observe signal scintillation during the STRESS experiment, an aircraft was flown so that the line-of-sight from the aircraft to the geosynchronous LES 8 satellite intersected the striated cloud. The aircraft velocity was perpendicular to the projection of the earth's magnetic field to observe the small scale signal fluctuations caused by field-aligned striations. The propagation experiments involved either uplink or downlink signals at different frequencies. In the uplink experiment, a 340 MHz CW signal was transmitted from the aircraft, up through the barium cloud to LES 8, then was relayed along an undisturbed path to a rooftop receiving station. In the downlink experiment, a 250 MHz CW signal was transmitted from the rooftop station, up to LES 8, then down through the barium cloud to the aircraft. For both the uplink and the downlink experiments, a coherent K-band signal was used as a phase reference so that the two quadrature components of the lower frequency signals could be measured and recorded.

During the three aircraft passes of interest here, the received signal exhibited Rayleigh fading characteristics with many deep fades and a measured  $S_4$  scintillation index close to unity. The recorded received signal was then used by Dr. Prettie as the input to a numerical propagation simulation where the signal was propagated from the receiver back up towards the barium cloud (Reference 2-2). This "backwards" propagation in free space was repeated for a number of propagation distances until a minimum  $S_4$  scintillation index was obtained for the back-propagated electric field.

Under ideal circumstances, where the barium-produced phase fluctuations are perfectly represented as a thin phase screen, then the fluctuations of the amplitude of the electric field will decrease as the location of the barium cloud is approached. (Equivalently, in the normal forward propagation sense, a thin phase screen is modeled as producing instantaneous phase changes, but no amplitude fluctuations. The amplitude fluctuations develop as the wave propagates away from the phase screen location (Reference 2-3)). Now when a minimum  $S_4$  scintillation index is obtained for a particular back-propagation distance, then the back-propagated phase at this distance is assumed to be directly related to the integrated electron-density fluctuations caused by the barium cloud. Reciprocity permits the same back-propagation scheme for both uplink and downlink signals. In the three cases discussed here the  $S_4$  scintillation index obtained after back-propagation is approximately 0.5.

The usefulness of the back-propagation technique described here is dependent on a number of factors. First of all, both received amplitude and phase must be measured sufficiently accurately. Secondly, since the numerical propagation simulation here is two-dimensional, allowing for variation perpendicular to the magnetic field but permitting no variation along the magnetic field, the technique is limited in the geometry that can be considered. Fortunately, the experimental geometry was such that most of the scattering was caused by irregularities perpendicular to the magnetic field direction. In general, however, the effects of noise and finite-sized correlation lengths along the magnetic field have not been investigated here.

Other assumptions implicit in this analysis are that the barium cloud is relatively stationary during the aircraft passes and that very little evolution of the striations occurs over the pass duration. The first assumption is reasonable since observations of cloud motion for the

two clouds considered show that the maximum velocity component perpendicular to the projection of the magnetic field line on the earth's surface was approximately 18 m/sec with an equal velocity component in the orthogonal direction along the earth's surface. The second assumption also seems reasonable since the duration of the three aircraft passes are 70 seconds (Esther pass 10 at 48 minutes after release), 130 seconds (Esther pass 17 at 117 minutes after release), and 60 seconds (Fern pass 9 at 43 minutes after release).

## 2.2 PHASE PSD ANALYSIS

This section describes the details of the analysis of three measurements of back-propagated phase from the STRESS series. The phase measurements were provided to us by Dr. Cliff Prettie\* of ESL, Incorporated (Reference 2-4). As stated in the previous section, it is assumed that the back-propagated phase is directly proportional to the integrated electron-density fluctuations caused by the barium cloud striations.

Figure 2-1 shows the signal phase determined from the ESL back-propagation technique observed during an aircraft pass in the shadow of the barium cloud Esther at 48 minutes after release.

The back-propagated phase data, measured as a function of time during the aircraft pass, was converted to the spatial scale shown on Figure 2-1 by obtaining the aircraft velocity perpendicular to the plane containing the line-of-sight and the magnetic field direction, both measured at the location of the intersection of the line-of-sight with the barium cloud. According to Reference 2-5, if the striations are axisymmetric with an arbitrary axial ratio, then the scale size perpendicular to the magnetic field direction can be obtained by considering scintillations only along this particular direction. For Esther pass 10, the actual aircraft velocity was 235 m/sec with the aircraft travelling at a constant altitude along a direction 225° clockwise from north. The aircraft was located at 29°N latitude and 85°W longitude. LES 8 was in a synchronous orbit at 21°N latitude and 107°W longitude at an altitude of 36000 km. At the barium location (180 km altitude, 29°N latitude, 86°W longitude),

---

\* Dr. Prettie also provided data on the link geometry during STRESS.

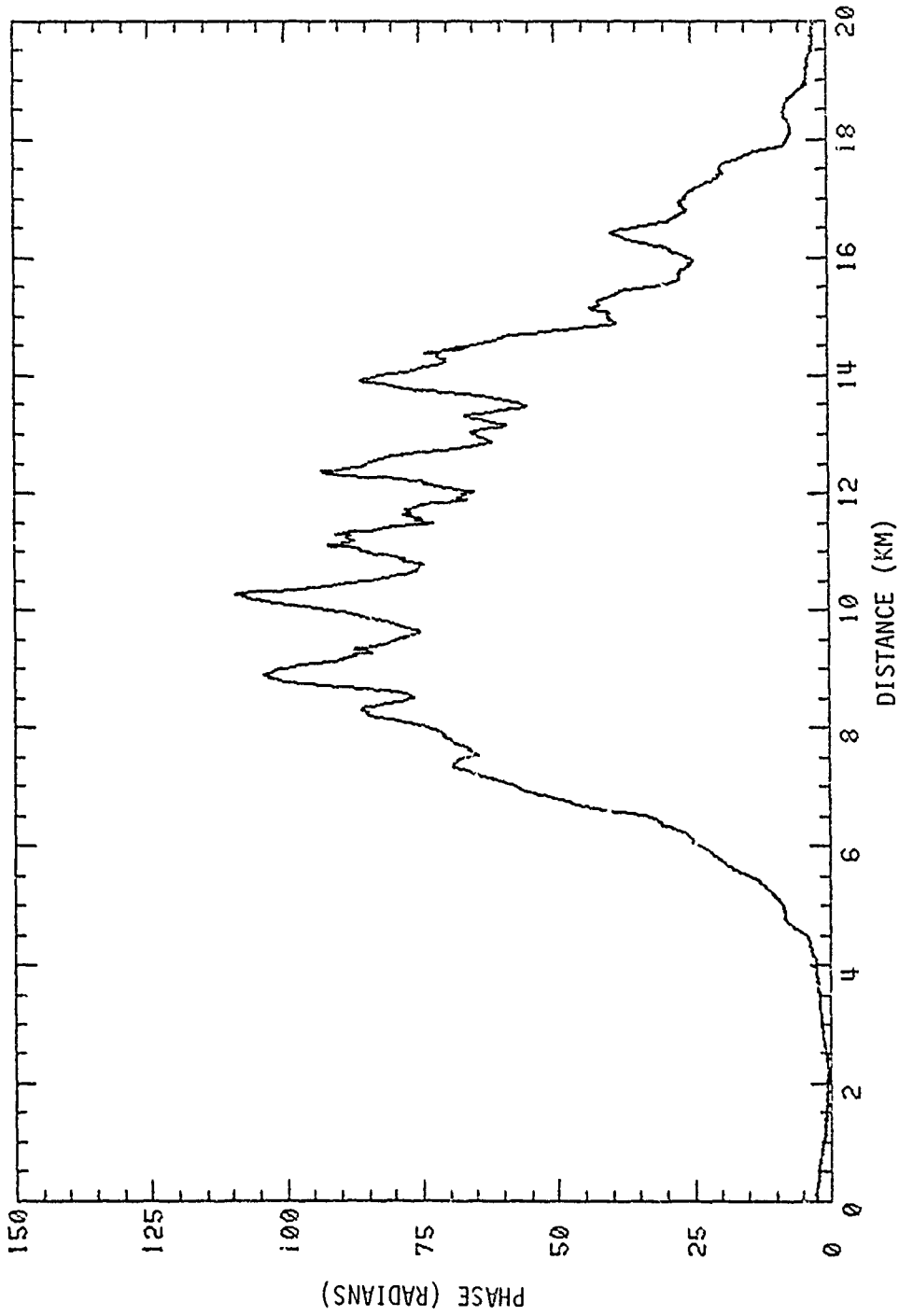


Figure 2-1. Back-propagated phase for Esther pass 10.  
 (Data provided by ESL, Incorporated.)

the magnetic field dip angle was  $59^\circ$  and the angle between the line-of-sight and the magnetic field direction was  $30^\circ$ . The angle between the aircraft direction and the normal to the plane containing the line-of-sight and the magnetic field direction was  $67^\circ$ . By design, the aircraft velocity was in the same direction as the horizontal projection of the vector perpendicular to the plane containing the magnetic field direction and the line-of-sight.

The phase data is easily detrended or separated into a "deterministic" or non-striated gaussian-like part and a "random" or striated part. Figure 2-2 shows the deterministic part which is obtained from the data of Figure 2-1 by constructing a running average over a 3-kilometer interval. The random part is then obtained by subtracting the running average from the original data. This procedure of separating out the deterministic part of the phase is quite reasonable here since aircraft passes at earlier times after release quite clearly show the smooth gaussian-like unstriated barium cloud, quite similar to that shown in Figure 2-2.

Once the random part of the phase shown in Figure 2-3 was obtained, the central portion, from 6 km to 18 km on the figure was then selected as best representing the homogeneous or uniform striation region of the cloud where the noticeably different appearance of the edges was absent. The variance of the phase,  $\sigma_\phi^2$ , was obtained from this portion by computing the necessary averages directly from the data. The power spectrum shown in Figure 2-4 was also obtained from this uniform portion of the data, where the "raw" spectrum was smoothed by forming a running average over a  $\pm 5\%$  bandwidth.

Another important consideration should be mentioned regarding the choice of the uniform striation region from the random part of the phase. In addition to choosing that region from the center where the phase

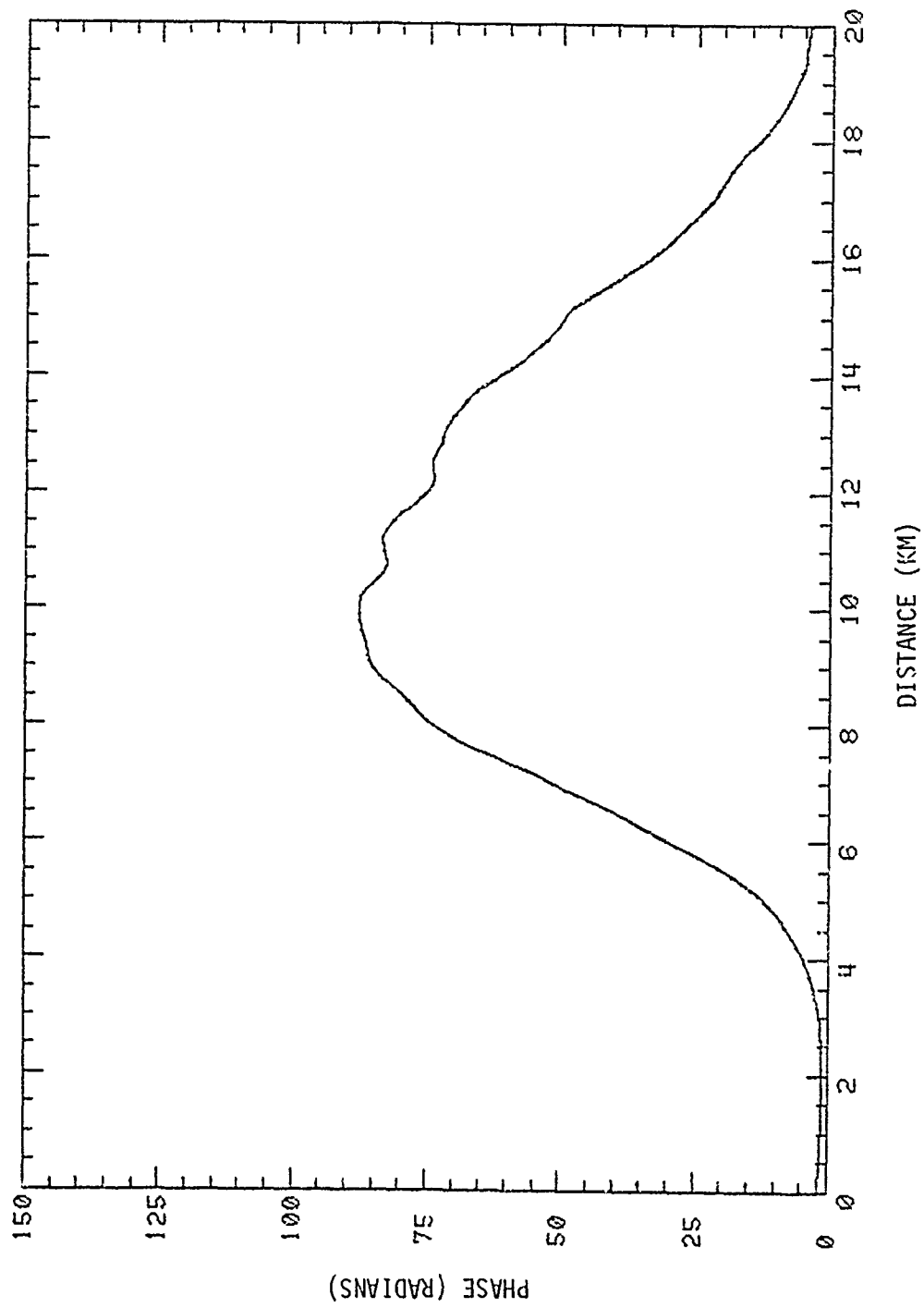


Figure 2-2. Deterministic part of the back-propagated phase for Esther pass 10.

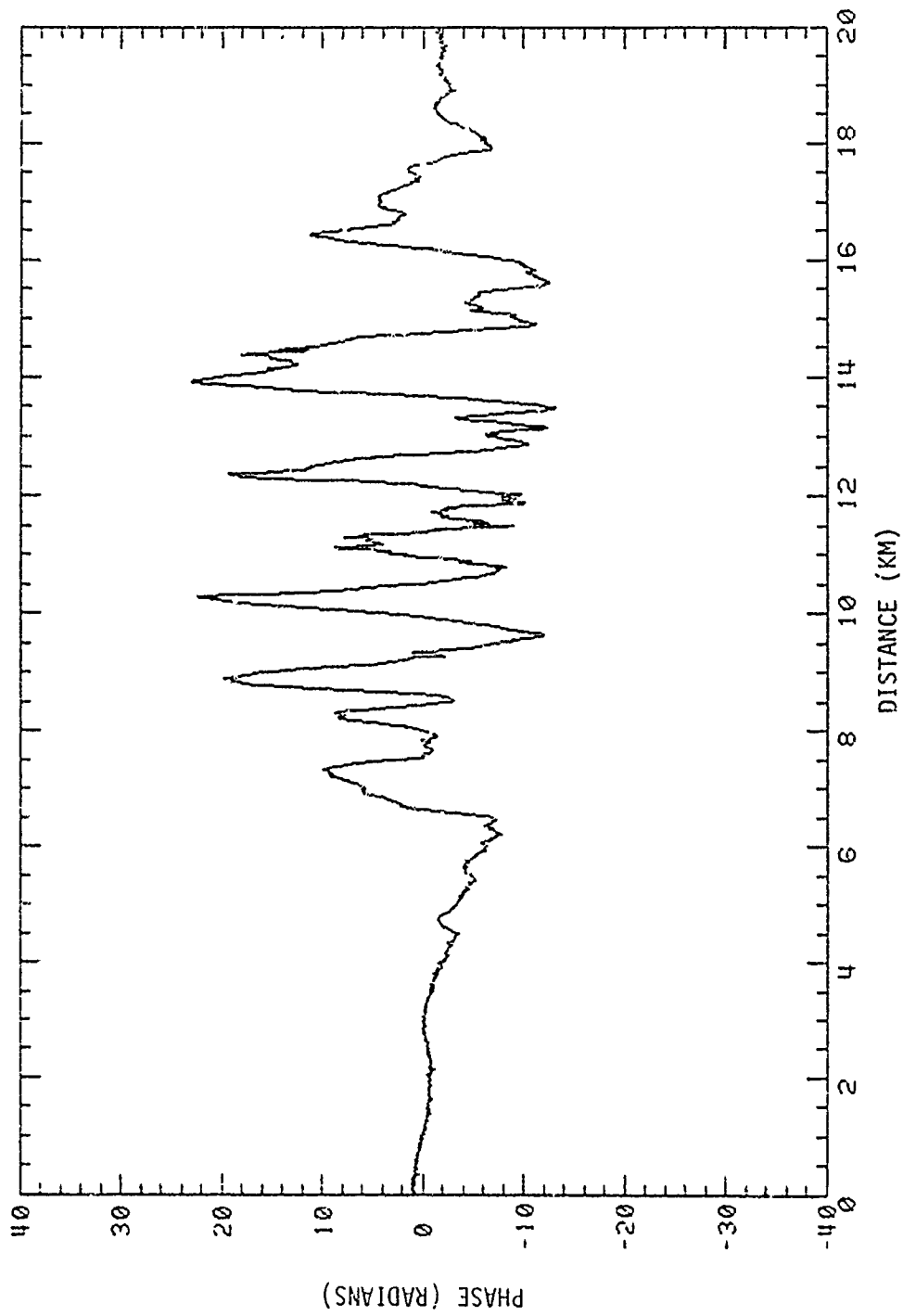


Figure 2-3. Random component of the back-propagated phase for Esther pass 10.

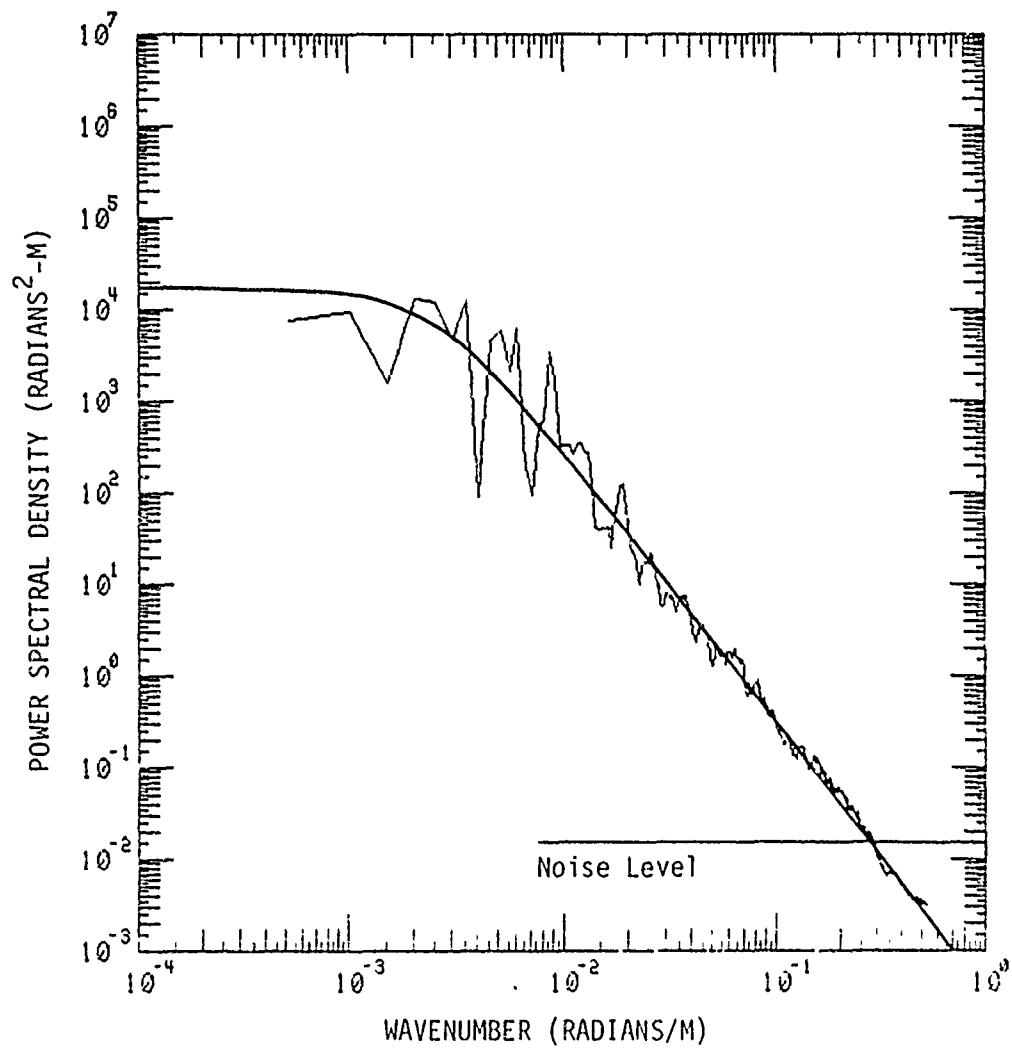


Figure 2-4. Power spectral density of the random component of the back-propagated phase for Esther pass 10.

fluctuations appear homogeneous, it is also convenient to choose the end points carefully so that no discontinuity exists. Elimination of any discontinuity at this stage of the analysis facilitates a cleaner use of a digital Fourier transform algorithm to compute the power spectral density. No windowing is needed and any difficulties involving rescaling of the variance because of windowing effects are avoided. As a check on the results, the PSD's computed from the carefully chosen uniform regions were compared to the PSD's of the original data before removal of the deterministic parts. Agreement was noted for the portion of the PSD unaffected by the detrending.

The noise level noted on Figure 2-4 was obtained from consultations with Dr. Prettie of ESL (Reference 2-4). Also shown in Figure 2-4 is the best fit one-dimensional power spectral density (PSD) of the form

$$S(K) = \frac{\sigma_{\phi}^2 \Gamma\left(\frac{m}{2}\right) L_0}{\sqrt{\pi} \Gamma\left(\frac{m-1}{2}\right) (1+K^2 L_0^2)^{m/2}} \quad (2-1)$$

where  $\sigma_{\phi}^2$  is the variance, obtained as explained above.  $\Gamma$  is the gamma function,  $L_0$  is the outer scale and  $K$  is the spatial wavenumber. The form of the PSD is chosen so that the normalization is

$$\sigma_{\phi}^2 = \int_{-\infty}^{\infty} S(K) dK \quad (2-2)$$

The fit shown was obtained by determining the spectral index  $m$  by a least square fit of the smoothed PSD between  $K = 10^{-2}$  and  $10^{-1}$  radians/m. In obtaining the spectral index, points chosen from the smoothed PSD were equally spaced on the wavenumber axis shown so that the results were not driven by the large number of data points at the higher wavenumber end of the spectral interval over which the least squares fit was performed.

Once the spectral index,  $m$ , and the variance,  $\sigma_{\phi}^2$ , were both obtained, the value of the outer scale was obtained by solving Equation 2-1 at  $K = 0.1$  radians/m with  $S(K)$  obtained from the least squares fit.

The same analysis procedure was used for two other aircraft passes during releases Esther and Fern. Table 2-1 shows the results for the spectral index and outer scale for all three passes analyzed. As stated previously, the phase from Esther pass 10 was detrended by subtracting a running average obtained over a 3 km interval. For Esther pass 17 the interval chosen was 6 km; for Fern pass 9, the appropriate interval was 2 km. Figures 2-5 and 2-6 show the PSD's of the random parts of the back-propagated phase obtained from Esther pass 17 and Fern pass 9. The link geometry for Esther pass 17 and Fern pass 9 was very similar to the geometry of Esther pass 10 and similar scaling of the recorded back-propagated phase was used to obtain the distance scales.

Table 2-1. PSD measurements for STRESS events.

STRESS Event	Link	$\sigma_{\phi}$	Spectral Index	Outer Scale
Esther pass 10 (Release + 48 min)	Uplink 340 MHz	9.7 radians	3	390 meters
Esther Pass 17 (Release + 117 min)	Downlink 250 MHz	11.4 radians	3.4	470 meters
Fern pass 9 (Release + 43 min)	Uplink 340 MHz	4.9 radians	3.2	350 meters

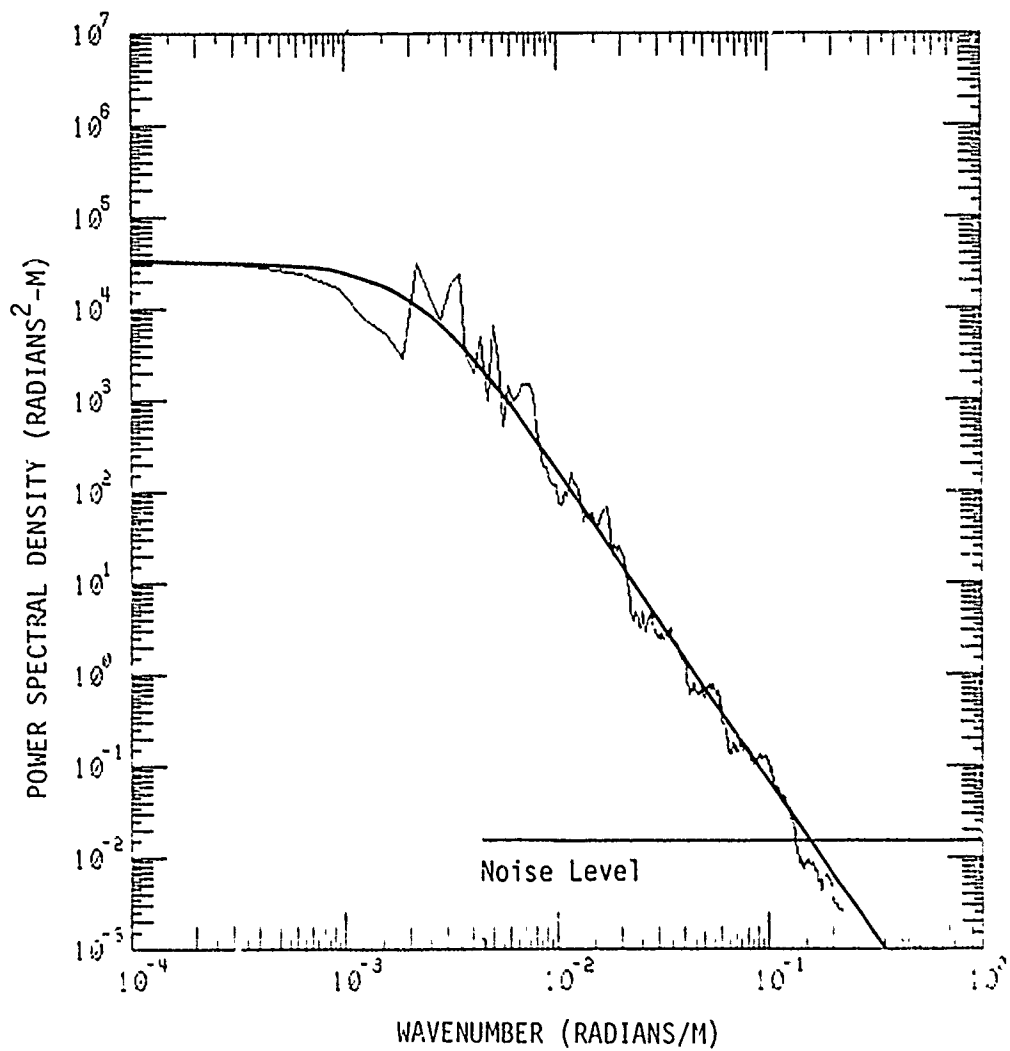


Figure 2-5. Power spectral density of the random component of the back-propagated phase for Esther pass 17.

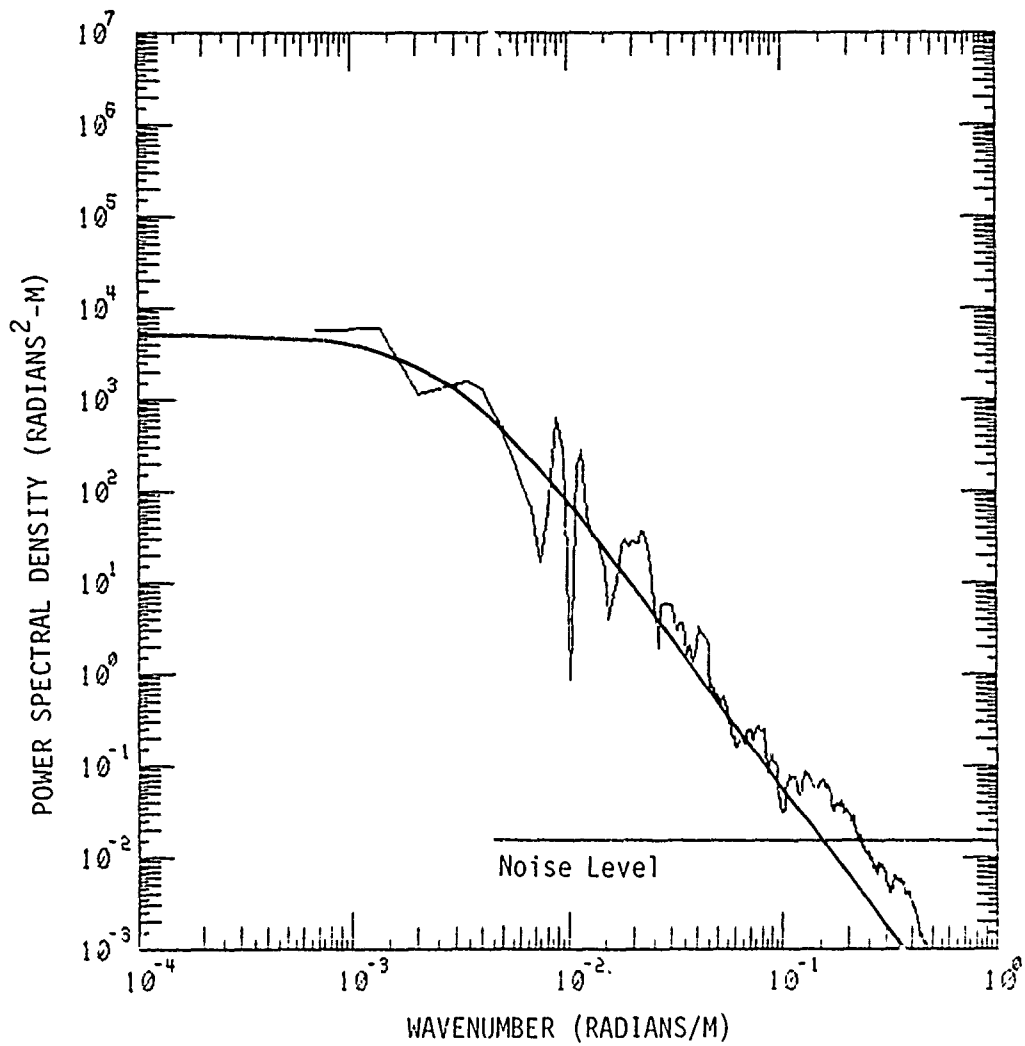


Figure 2-6. Power spectral density of the random component of the back-propagated phase for Fern pass 9.

Note that none of the three PSD's shown in Figures 2-4 to 2-6 show any evidence of an inner scale cutoff. It is well known that the inner scale plays an important role in cutting off angular scattering—particularly for phase PSD's with a spectral index of 3 or less (References 2-6 and 2-7).

It should be noted that the results in Table 2-1 include the effects of a careful consideration of the actual experimental geometry (aircraft position and heading, satellite location, magnetic field direction). Earlier results, based on less detailed information on the experiment and a slightly simpler analysis technique (visual instead of least squares curve fitting) were used in the rest of this report to provide statistical models of the important features of Esther pass 10 and Fern pass 9. These results differ only slightly from those presented in Table 2-1. For Esther pass 10 the original value of  $L_o$  was 360 m with a spectral index of 3. For Fern pass 9, the original value obtained for  $L_o$  was 270 meters with a spectral index of 3.5.

Measurements taken during the STRESS test (Reference 2-8) indicate that the thickness of the striated barium clouds range from 5 to 10 kilometers perpendicular to the magnetic field lines. Of course elevation angles other than  $90^\circ$  (vertical propagation) will give a larger propagation distance through the striations. For simplicity, assume that the combined effect of cloud thickness and elevation angles gives a propagation distance of 10 km through the barium striations. It is possible to deduce the mean-square electron density fluctuations from the relationship

$$\sigma_\phi^2 = 2(r_e \lambda)^2 \sqrt{\pi} \Gamma\left(\frac{m-1}{2}\right) L_o L \langle \Delta N_e^2 \rangle / \Gamma\left(\frac{m-2}{2}\right) \quad (2-3)$$

where  $r_e$  is the classical electron radius,  $\lambda$  the wavelength,  $L_o$  the outer scale size, and  $L$  the propagation distance through the striated

layer (assumed to be 10 km). Using the results shown in Table 2-1 with Equation 2-3 the values obtained for the rms electron density fluctuations are  $1.4 \times 10^6 \text{ cm}^{-3}$  for Esther pass 10,  $9.8 \times 10^5 \text{ cm}^{-3}$  for Esther pass 17 and  $7.0 \times 10^5 \text{ cm}^{-3}$  for Fern Pass 9. These values are within the ranges measured by radar (Reference 2-9) and by in-situ rocket probes (Reference 2-10).

### 2.3 BARIUM CLOUD MODELING VERIFICATION

As a check on the barium cloud striation modeling, early results from the back-propagation phase analysis of Esther pass 10 were used in the multiple phase screen simulation to generate signals to compare to the actual received signals measured experimentally. These early results differed from those in Table 2-1 in that the slopes were obtained by a visual fit to the PSD's. For Esther pass 10 the early value of the outer scale was 360 m (as compared to 390 m obtained by the least squares process). The spectral index of  $K^{-3}$  did not change with the more accurate analysis.

Figure 2-7 shows the phase screen generated to model Esther pass 10 and is to be compared to the back-propagated phase data shown in Figure 2-1. The phase screen shown in Figure 2-7 is composed partly of a gaussian shape whose size is chosen to match the deterministic barium cloud. To this deterministic gaussian is added a random phase characterized by a  $K^{-3}$  PSD with an outer scale of 360 m. The random phase is windowed or cutoff on the edges so that no phase perturbations occur outside the deterministic gaussian cloud. A pseudo-random sequence of coefficients actually determines the details of the random phase screen so that the phase screen realization shown in Figure 2-7 is one of many possible. To obtain statistically significant results, other pseudo-random sequences could be used and the results for the received signal could be averaged.

To model Esther pass 10, a plane wave is propagated through the phase screen, down to a ground based receiver. 16384 points were used to represent the phase shown in Figure 2-7 over a distance of 30 km, of which only 20 km is shown in the figure. Thus, the distance between points on the grid is 1.831 m. In the absence of an explicit inner scale in the PSD, the minimum separation between grid points controls the effective inner scale in the MPS code. Here the effective inner scale is  $\Delta x/\pi$  or 0.58 m, according to the Nyquist sampling theorem.

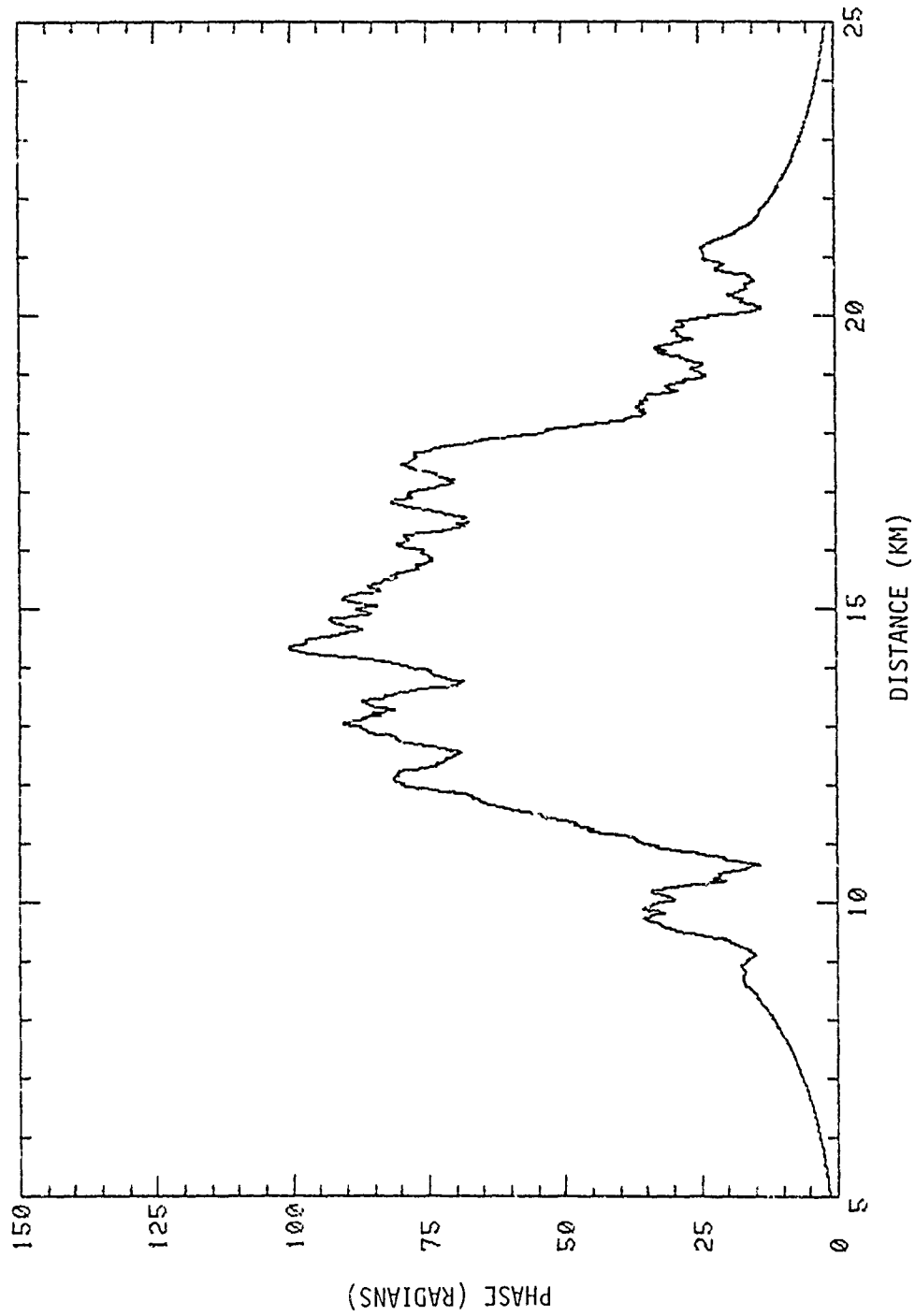


Figure 2-7. Phase screen generated numerically to model Esther pass 10.

Figures 2-8 and 2-9 show a comparison of the numerically generated signal amplitude (plotted in decibels relative to the mean amplitude) to the actual experimentally received data. Figure 2-8 shows 23 seconds (4.6 km at a velocity of 220 m/sec) of received data taken during the STRESS test. Figure 2-9 shows a 5 km portion of the signal realization generated numerically. The 15 km point on the abscissa of Figure 2-9 corresponds to the point directly below the center of the cloud. A visual comparison of the two figures indicates reasonably good agreement of the numerical results with the observed experimental results. The major difference appears to be that the numerical results have a higher percentage of fades below 20 dB. The distance between fades appears similar. No statistical comparison was possible here since the experimental data was available only in the graphical form shown.

Figures 2-10 and 2-11 compare the numerical and measured signal phases corresponding to the previous signal amplitudes. Note a slight discrepancy in the ordinate axes where the two scales differ in length by  $2\pi$  radians. A visual comparison again indicates relatively good agreement between overall appearances of the numerical and experimental results.

Figures 2-12 and 2-13 compare the experimental back-propagated phase for Fern pass 9<sup>\*</sup> with the numerical phase screen model of this pass. Figure 2-12 shows the back-propagated phase data provided by Dr. Prettie of ESL. By a visual fitting process an outer scale of 270 meters and a spectral index of 3.5 were originally obtained for the phase PSD. (More detailed analysis indicates that a better fit is obtained for an outer scale of 350 m and a spectral index of 3.2 as shown in Table 2-1.)

---

\* A velocity of 220 m/sec was originally used to convert the time domain data of Fern pass 9 to the spatial domain. More careful attention to the actual geometry later resulted in a value of 200 m/sec which was used to obtain the more accurate results shown in Table 2-1.

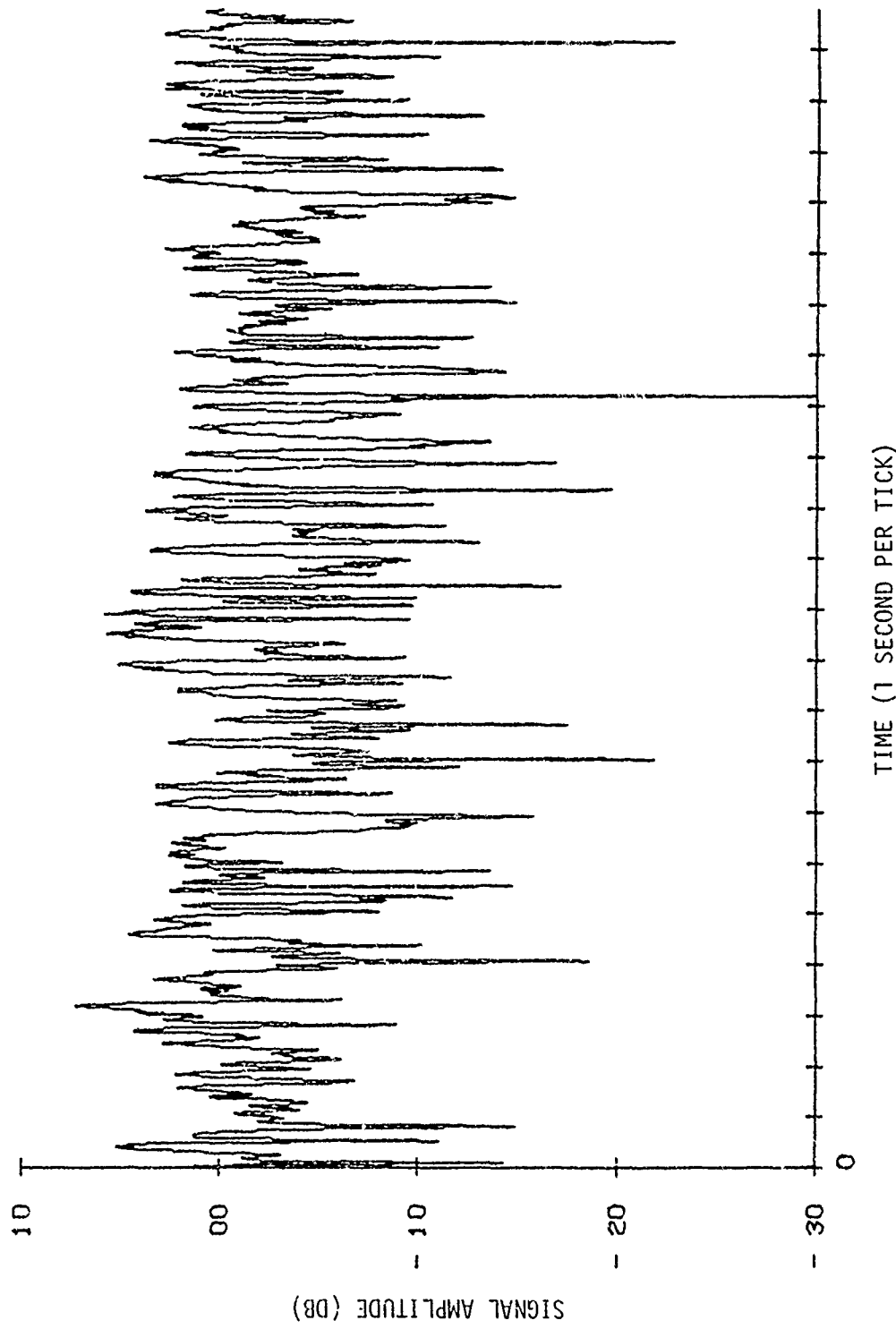


Figure 2-8. Experimentally measured received signal amplitude during Esther pass 10.  
(Figure provided by ESL, Incorporated.)

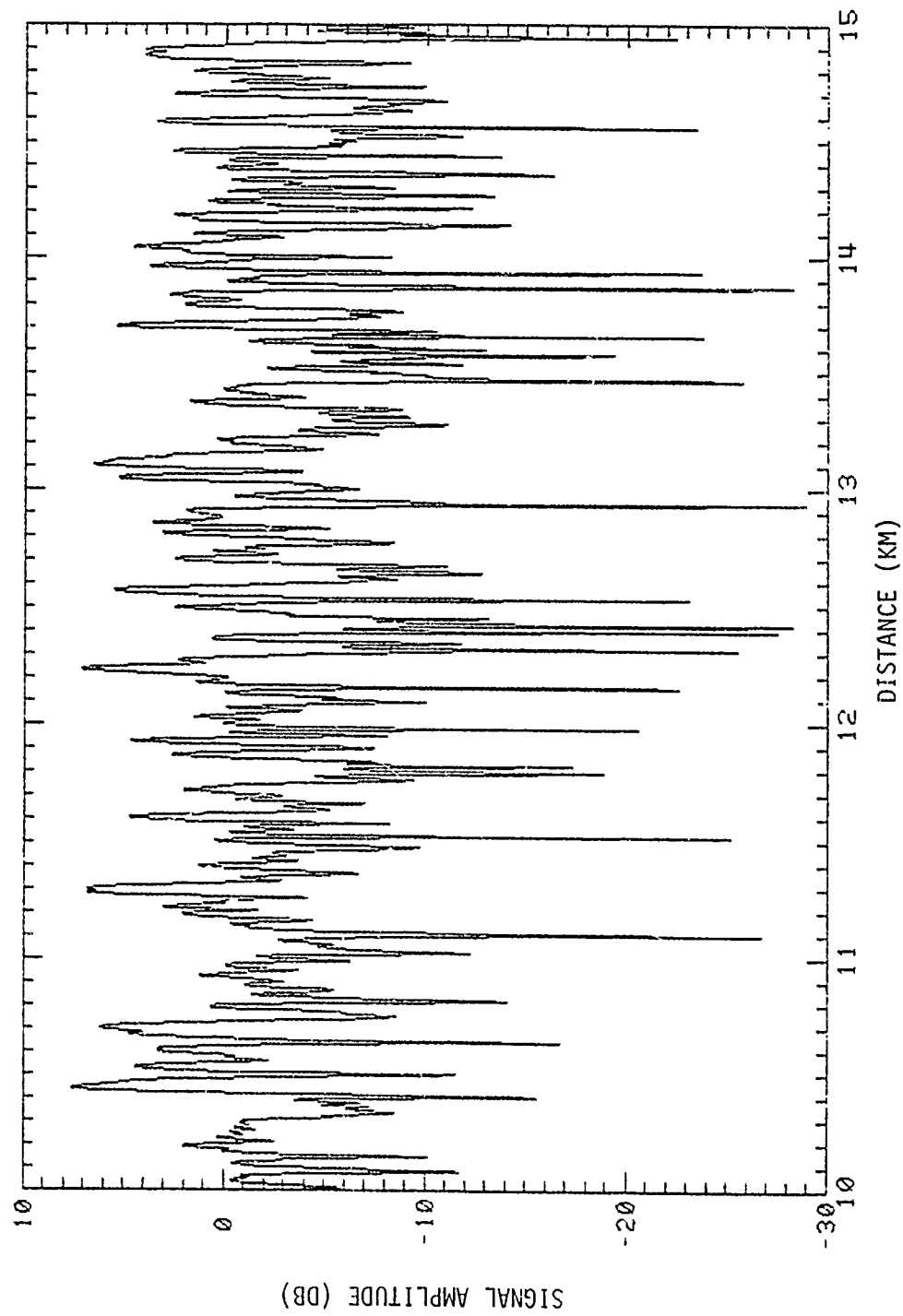


Figure 2-9. Portion of the numerically generated signal amplitude after propagation through the phase screen of Figure 2-7.

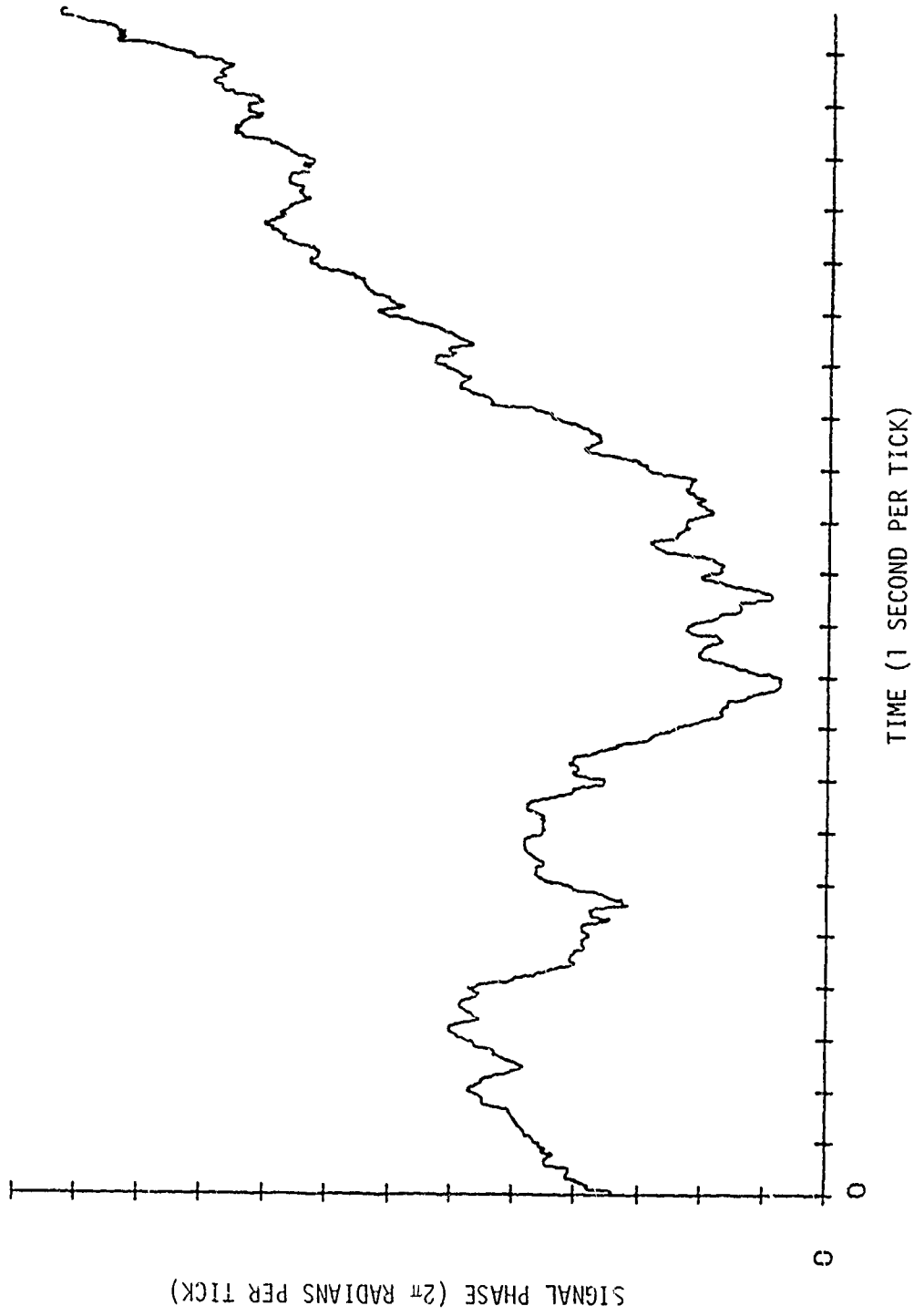


Figure 2-10. Experimentally measured signal phase corresponding to signal amplitude shown in Figure 2-8. (Figure provided by ESL, Incorporated.)

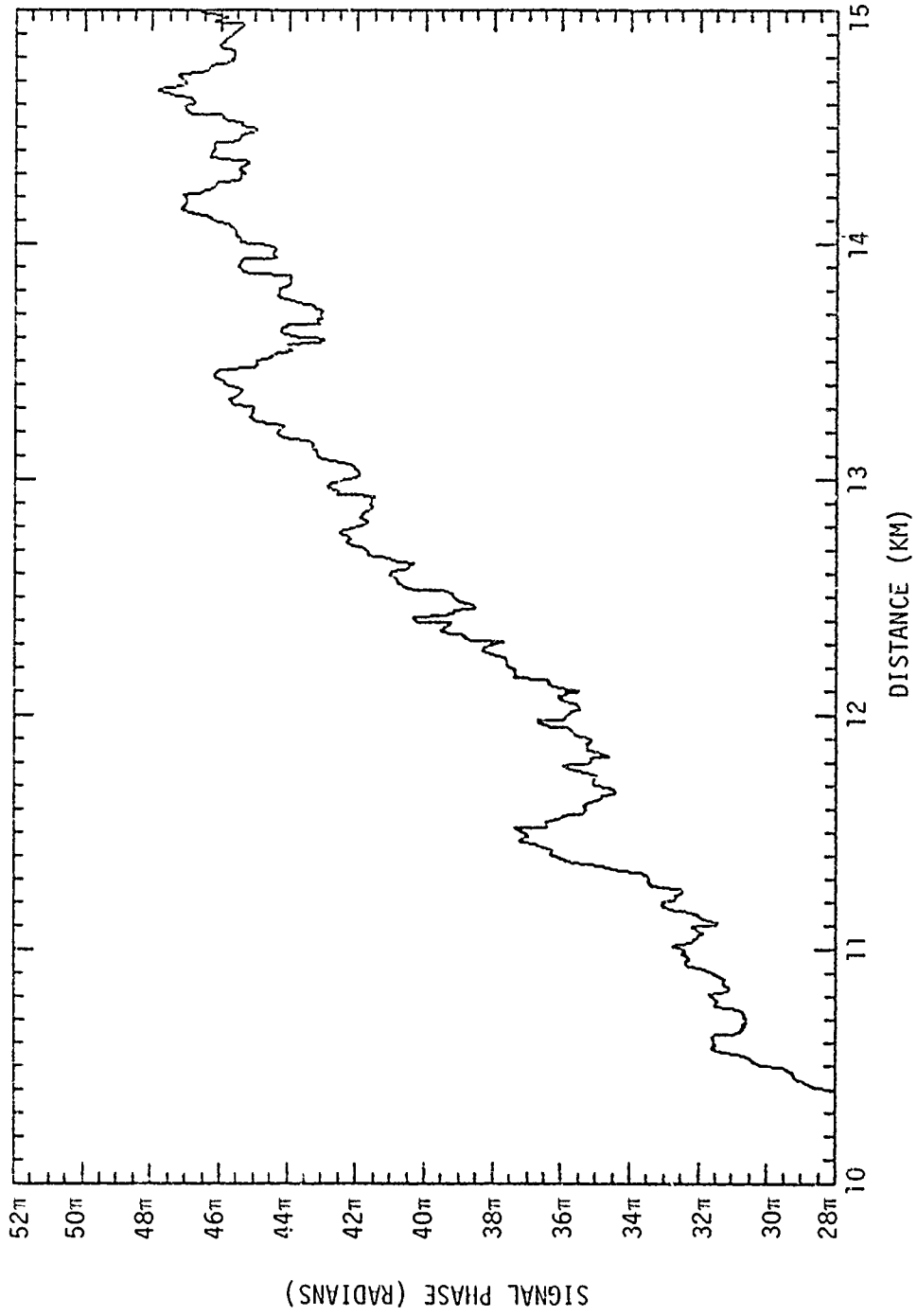


Figure 2-11. Numerically generated signal phase corresponding to signal amplitude shown in Figure 2-9.

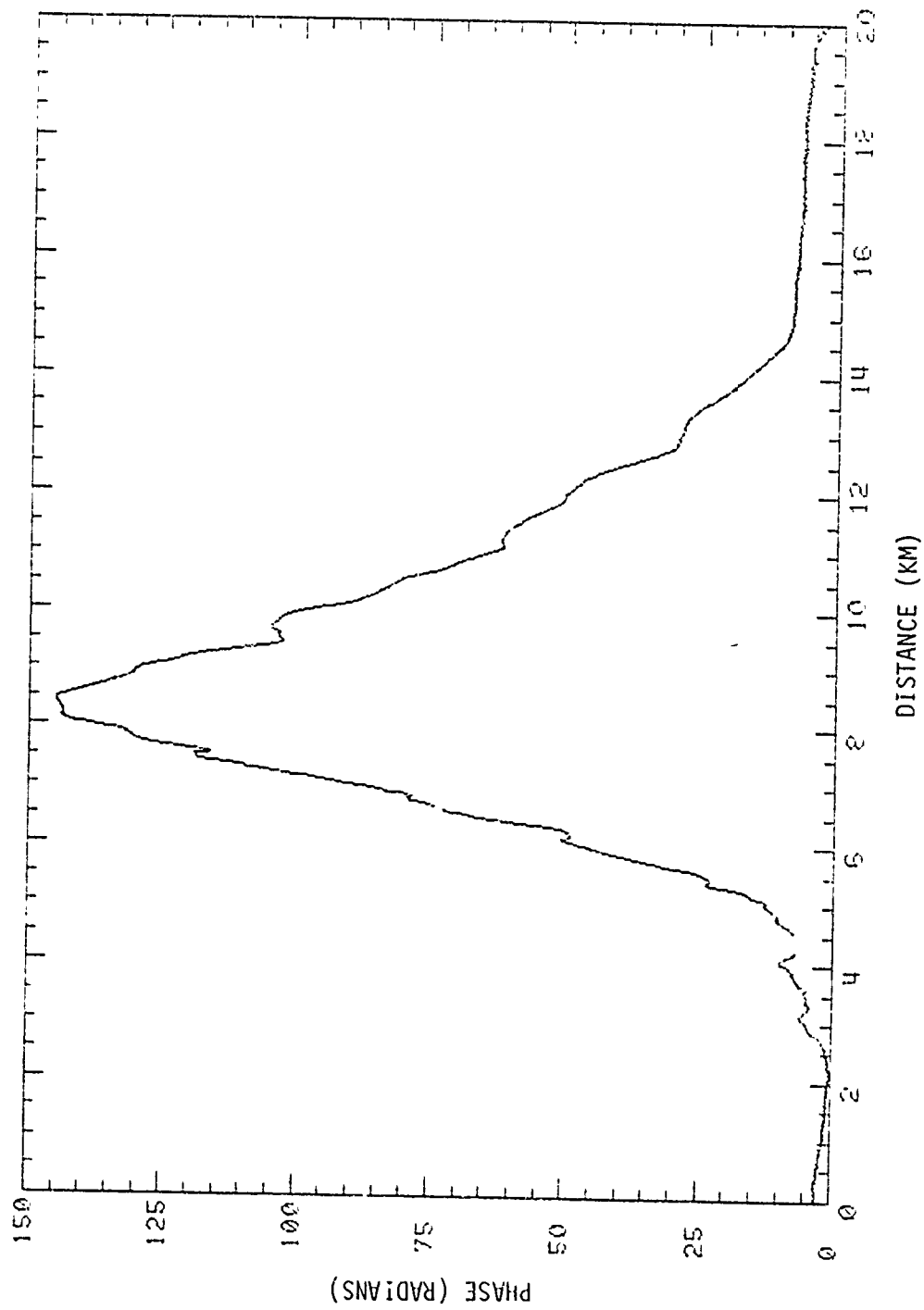


Figure 2-12. Back-propagated phase for Fern pass 9.  
(Data provided by ESL, Incorporated.)

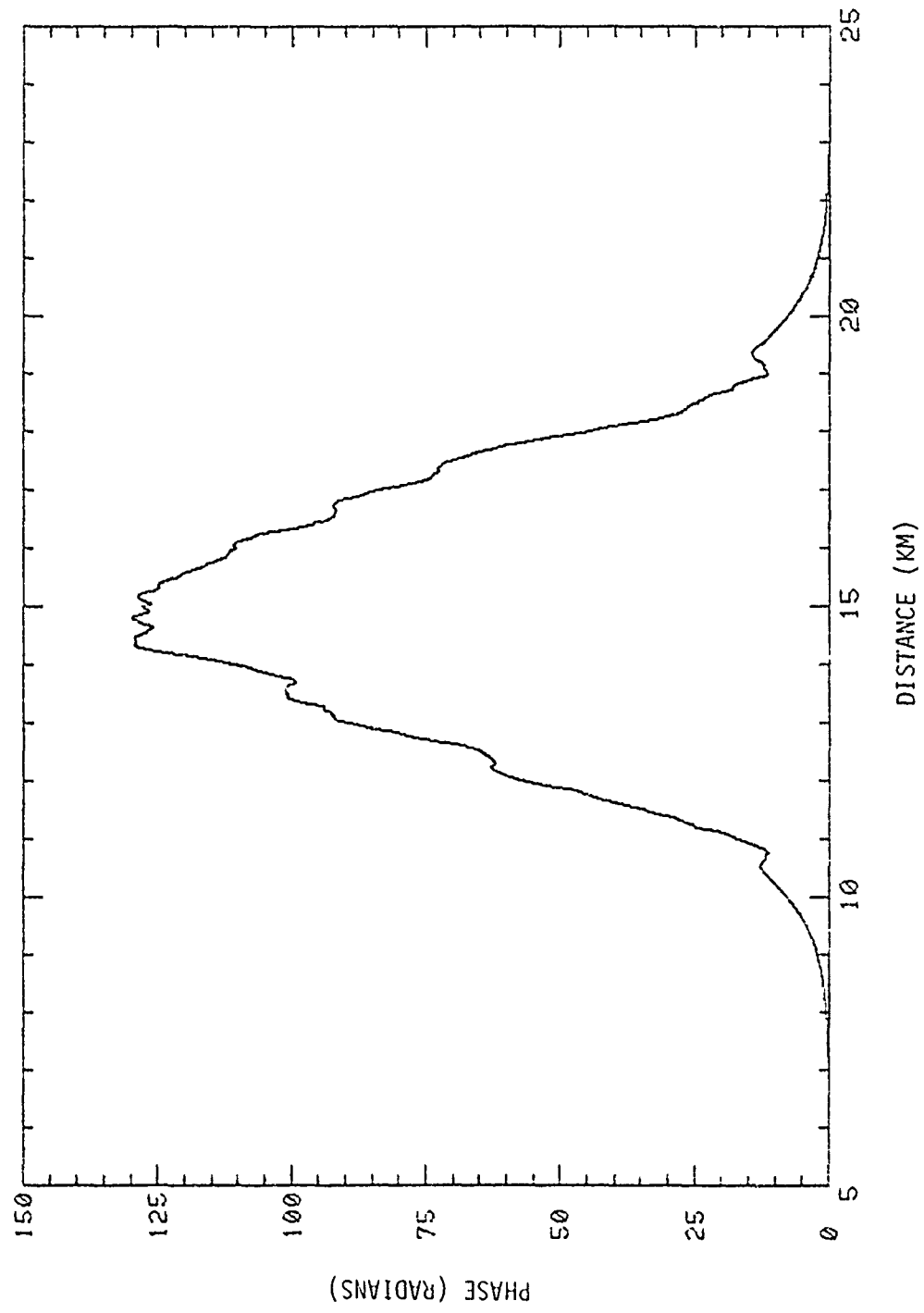


Figure 2-13. Phase screen generated numerically to model Fern pass 9.

Again using 16384 points to represent a grid 30 km long, the original PSD parameters were used to generate the phase screen shown in Figure 2-13 as a match to the experimental data. A comparison of Figures 2-12 and 2-13 demonstrates the reasonableness of the original fit to the PSD.

Figures 2-14 and 2-15 compare the experimentally measured received signal amplitude for Fern pass 9 with the amplitude obtained after numerical propagation through the phase screen shown in Figure 2-13. A visual comparison of Figures 2-14 and 2-15 again show the reasonableness of the phase PSD analysis and of the numerical propagation procedure.

Figures 2-16 and 2-17 compare the corresponding experimentally measured received phase with the numerically determined received phase. Comparison of these two figures also indicates reasonably good agreement between data and simulated signal characteristics.

Thus, this section demonstrates the general adequacy of the results of the back-propagated phase analysis. When the back-propagated phase PSD is used as input to the MPS propagation simulation, the results for the received signal amplitude and phase are in good agreement with the experimental results. With the exception of the inner scale values and the actual propagation geometry, Table 2-1 lists all the necessary parameters to utilize the MPS propagation simulation to generate signal structures characteristic of propagation through a barium cloud for the PLACES experiment.

In Section 4, the original results for the back-propagated phase PSD analysis of Esther pass 10 and Fern pass 9 are used to generate signal structures to represent propagation through the barium clouds at carrier frequencies from 150 to 250 MHz.

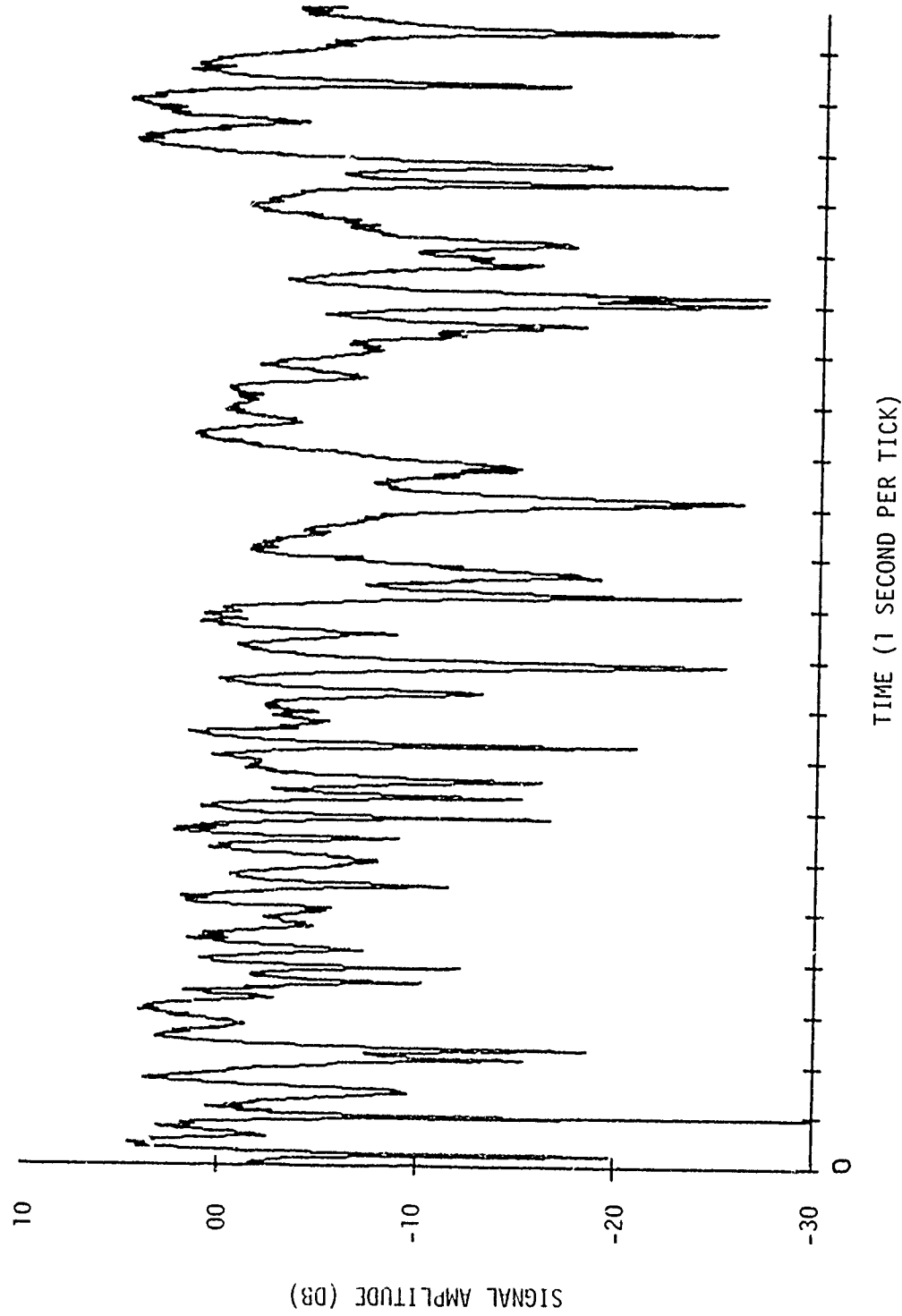


Figure 2-14. Experimentally measured received signal amplitude during Fern pass 9.  
(Figure provided by ESL, Incorporated.)

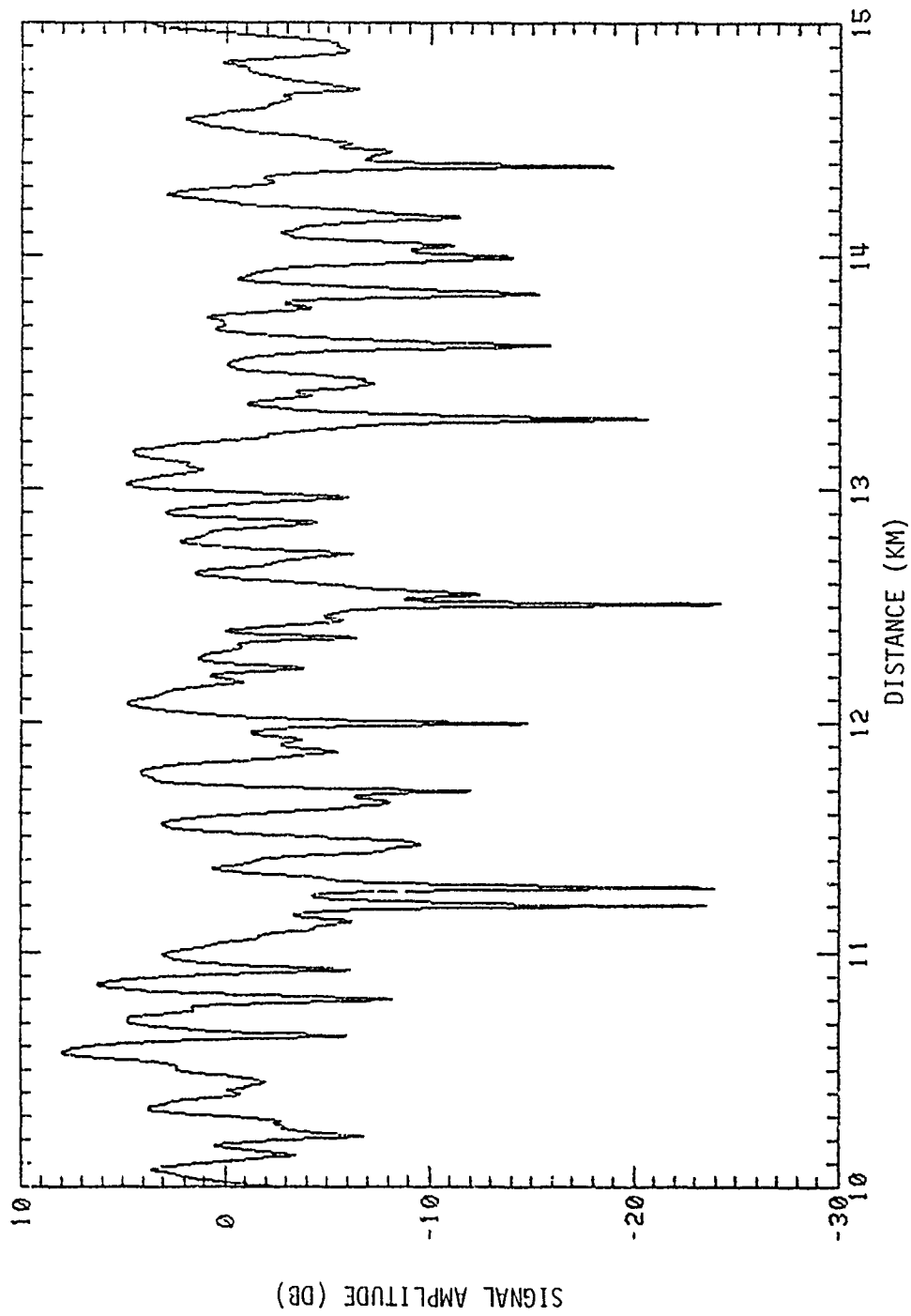


Figure 2-15. Portion of the numerically generated signal amplitude after propagation through the phase screen of Figure 2-13.

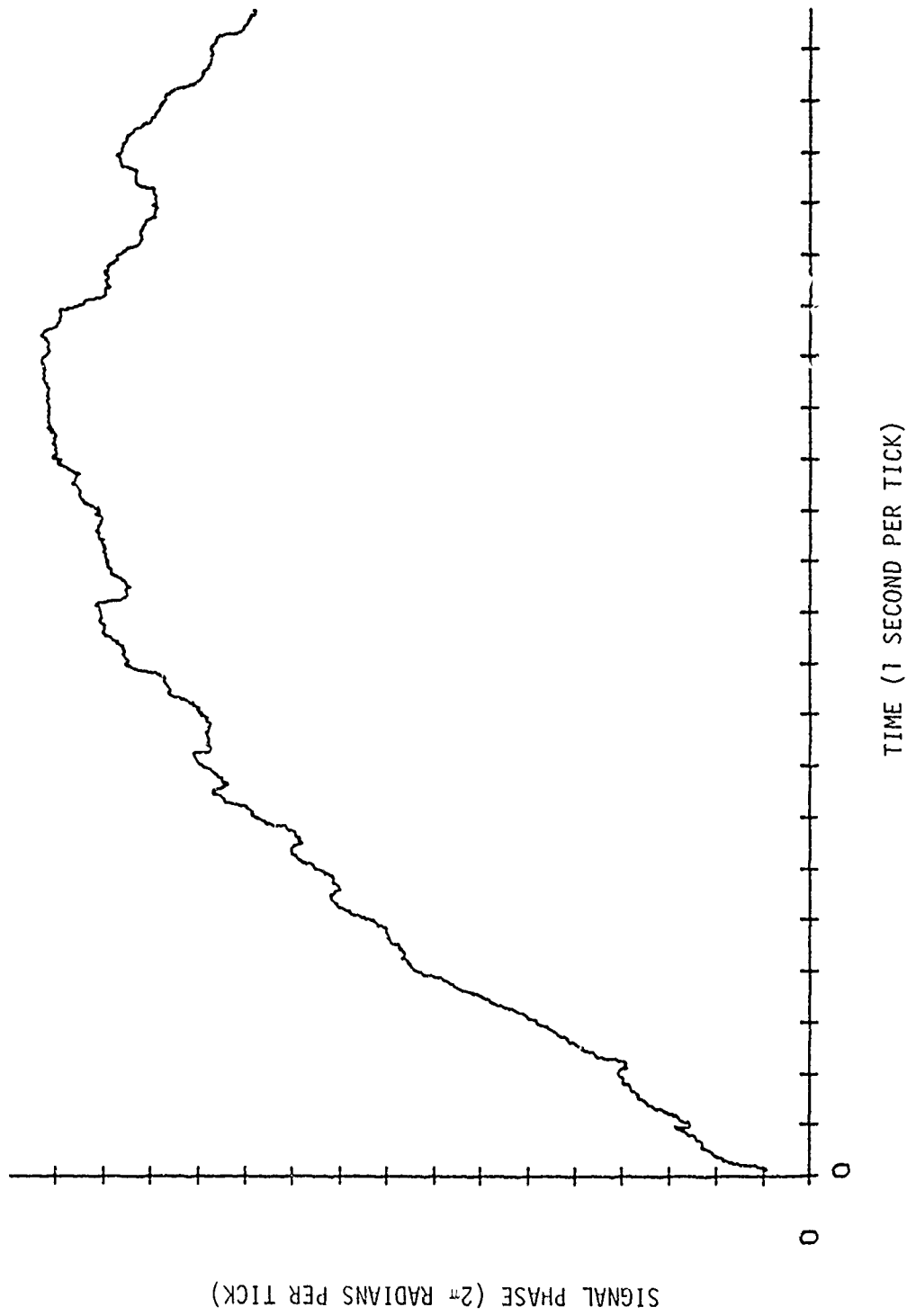


Figure 2-16. Experimentally measured signal phase corresponding to signal amplitude shown in Figure 2-14. (Figure provided by ESL, Incorporated.)

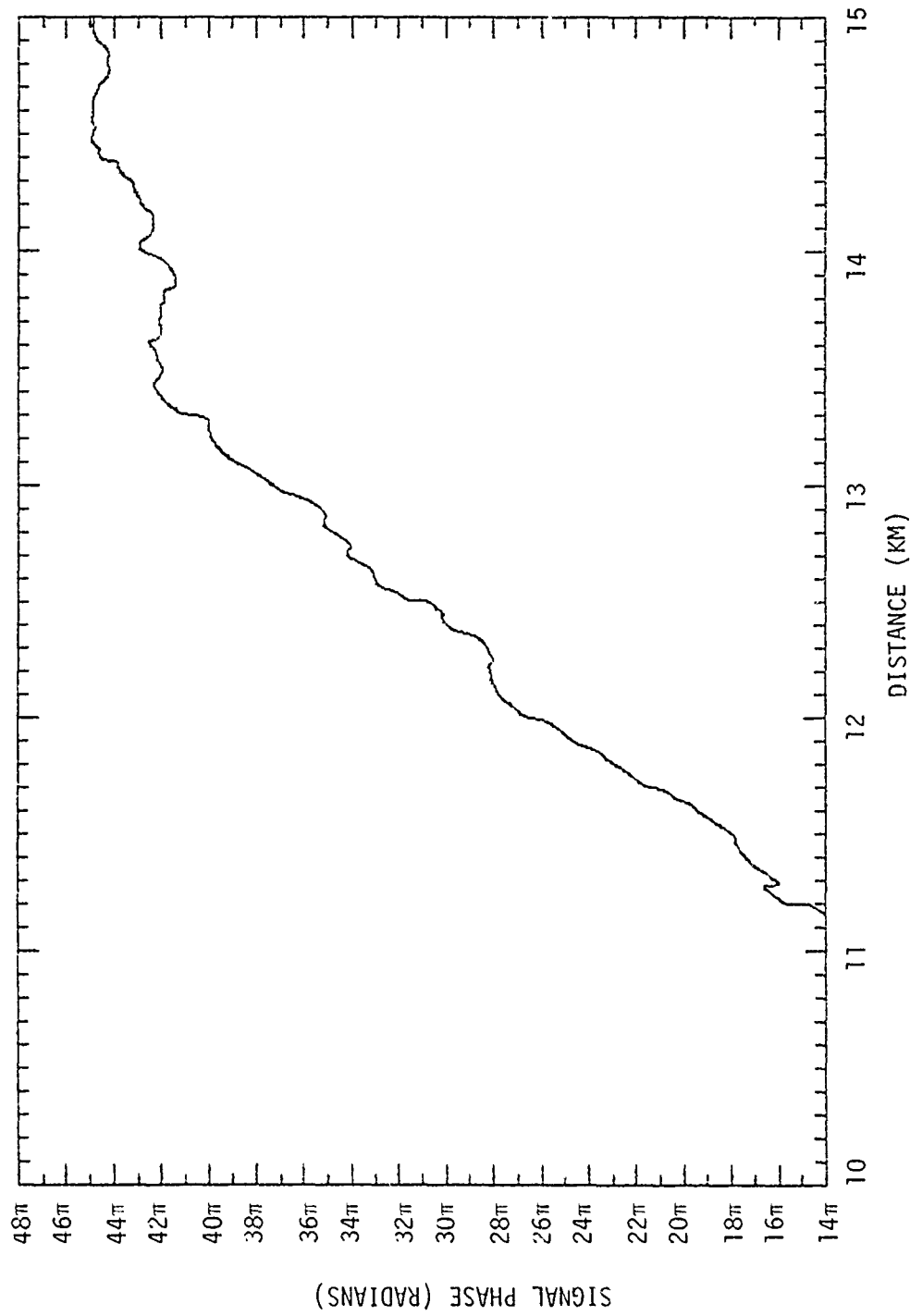


Figure 2-17. Numerically generated signal phase corresponding to signal amplitude shown in Figure 2-15.

## REFERENCES

- 2-1. Knepp, D.L., Multiple Phase-Screen Propagation Analysis for Defense Satellite Communications System, DNA 4424T, MRC-R-332, Mission Research Corporation, September 1977.
- 2-2. Prettie, C.W., and J.M. Marshall, "Satellite Link Measurements" in Proceedings of the STRESS Data Review Meeting, 29-30 November 1977, DNA 4620T, SRI International, compiled by D.R. McDaniel, June 1978.
- 2-3. Salpeter, E.E., "Interplanetary Scintillations. I. Theory," Astrophys. J., Vol. 147, pp. 433-448, 1967.
- 2-4. Prettie, C.W., ESL Incorporated. Numerous personal communications, August 1978 to April 1979.
- 2-5. Briggs, B.H. and I.A. Parkin, "On the Variation of Radio Star and Satellite Scintillations with Zenith Angle", J. Atmos. Terr. Phys., Vol. 25, pp. 339-365, 1963.
- 2-6. Yeh, K.C. and C.H. Liu, "An Investigation of Temporal Moments of Stochastic Waves", Radio Science, Vol. 12, No. 5, pp. 671-680, September-October 1977.
- 2-7. Knepp, D.L., "Variance and Bias of Angle Estimation Radars", IEEE Trans. Antennas Prop., Vol AP-24, No. 4, pp. 518-521, July 1976.
- 2-8. Linson, L.M. and D.C. Baxter, "Size, Shape and Age of Ion Clouds", from Proceedings of the STRESS Data Review Meeting, 29-30 November, 1977, DNA 4620T, SRI International, compiled by D.R. McDaniel, June 1978.
- 2-9. Gonzalez, V.H., "UHF Radar Data Analysis", from Proceedings of the STRESS Data Review Meeting, 29-30 November, 1977, DNA 4620T, SRI International, compiled by D.R. McDaniel, June 1978.
- 2-10. Kelley, M., D.L. Knepp, K.D. Baker and C. W. Prettie, "Direct Comparison of In-situ Plasma Density and VHF/UHF Phase Scintillation Measurements," to be submitted for publication.

### SECTION 3

#### PN SPREAD SPECTRUM CODE CORRELATOR

In this section a technique is derived to accurately simulate the operation of the pseudonoise (PN) code correlator in the X-set spread spectrum receiver. With the addition of the algorithm presented here, the X-set simulation described in Reference 3-1 is capable of fully simulating X-set receiver performance in all types of conditions, including severe, frequency-selective environments. In the next section, frequency-selective multiple phase screen (MPS) calculations of signal propagation through barium clouds are used as direct input to the X-set receiver simulation and results presented for receiver performance.

Frequency-selective effects can degrade the performance of the PN code tracking loop in a spread spectrum receiver. Signal transmission through a striated region can cause time delay, time delay jitter, and distortion of the received waveform, all of which affect the code tracking performance. Before describing the technique to model the X-set code correlator, it is useful to discuss receiver code tracking in a frequency-selective environment.

### 3.1 PN CODE TRACKING

The X-set receiver employs a noncoherent delay-lock loop for pseudonoise code tracking. In the code loop the incoming signal plus noise is alternately correlated with early and late codes from the receiver code generator. This is known as tau-dithering, with the amount of time dither set at one-half the chip duration in this case. The dithering loop is basically a delay-lock loop in which the early and late local references share the correlator and detector.

The receiver estimates of time-delay error are obtained by subtracting measurements of late power (obtained by correlation of the late code with the received code) from measurements of early power (obtained by correlation of the early code with the received code).

For infinite bandwidth, and no scintillation, dispersion or noise, the envelope of the PN code correlation function formed by correlating the received code with the internal reference code is a perfect triangle as shown in Figure 3-1. For perfect code tracking, the early power is obtained from Figure 3-1 at a time advance of one-half chip ( $\tau = -0.5$ ) and the late power is obtained from the figure at a time delay of one-half chip ( $\tau = 0.5$ ). Since these values are identical, subtracting the late power from the early power yields zero time-delay error, as it should for perfect code tracking.

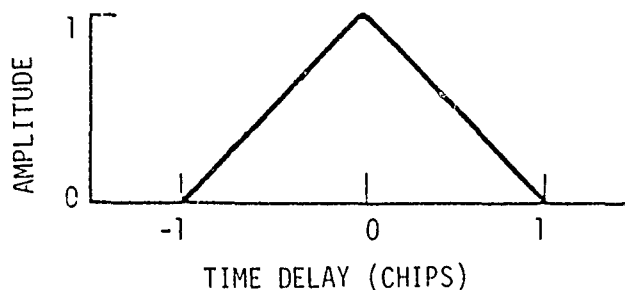


Figure 3-1. Envelope of the PN code autocorrelation function, infinite bandwidth, no scintillation or dispersion.

Figure 3-2 shows a three-dimensional plot of the PN code autocorrelation function envelope for nonselective fading conditions. That is, all frequency components across the bandwidth of the PN spread spectrum signal fade identically in this example. The PN code chip rate is much larger than the fading rate here so that propagation conditions remain unchanged during the many chip durations required to calculate one of the PN code autocorrelation functions shown. As time progresses, fading occurs and subsequent measurements of the autocorrelation function are shown plotted behind previous measurements in the figure. For nonselective fading, the shape of the autocorrelation function remains triangular although the peak and sharp edges are rounded because of the finite signal bandwidth. Fading effects are shown in Figure 3-2, by noting the progression of the envelope peaks with time.

Frequency-selective fading conditions caused by severe electron-density fluctuations can cause notable time delay jitter for wide bandwidth systems in two ways. First, striations can cause frequency-dependent angular scattering where stronger scattering occurs for the lower frequency components. Secondly, during propagation through an ionized medium, lower frequency signal components will experience a greater time delay than higher frequency components.

Both frequency-selective propagation mechanisms contribute to the results in Figure 3-3 which shows the PN code autocorrelation function behavior over a time interval of several seconds. As can be seen in this example, the PN code correlation function is severely distorted with signal energy delayed up to four code chips.

Figure 3-3 also shows a rather unusual, although interesting, example of this severe, frequency-selective environment on the operation of the PN code-tracking function. The arrows in Figure 3-3 show the estimated code time delay as it is tracked in the receiver delay-lock loop.

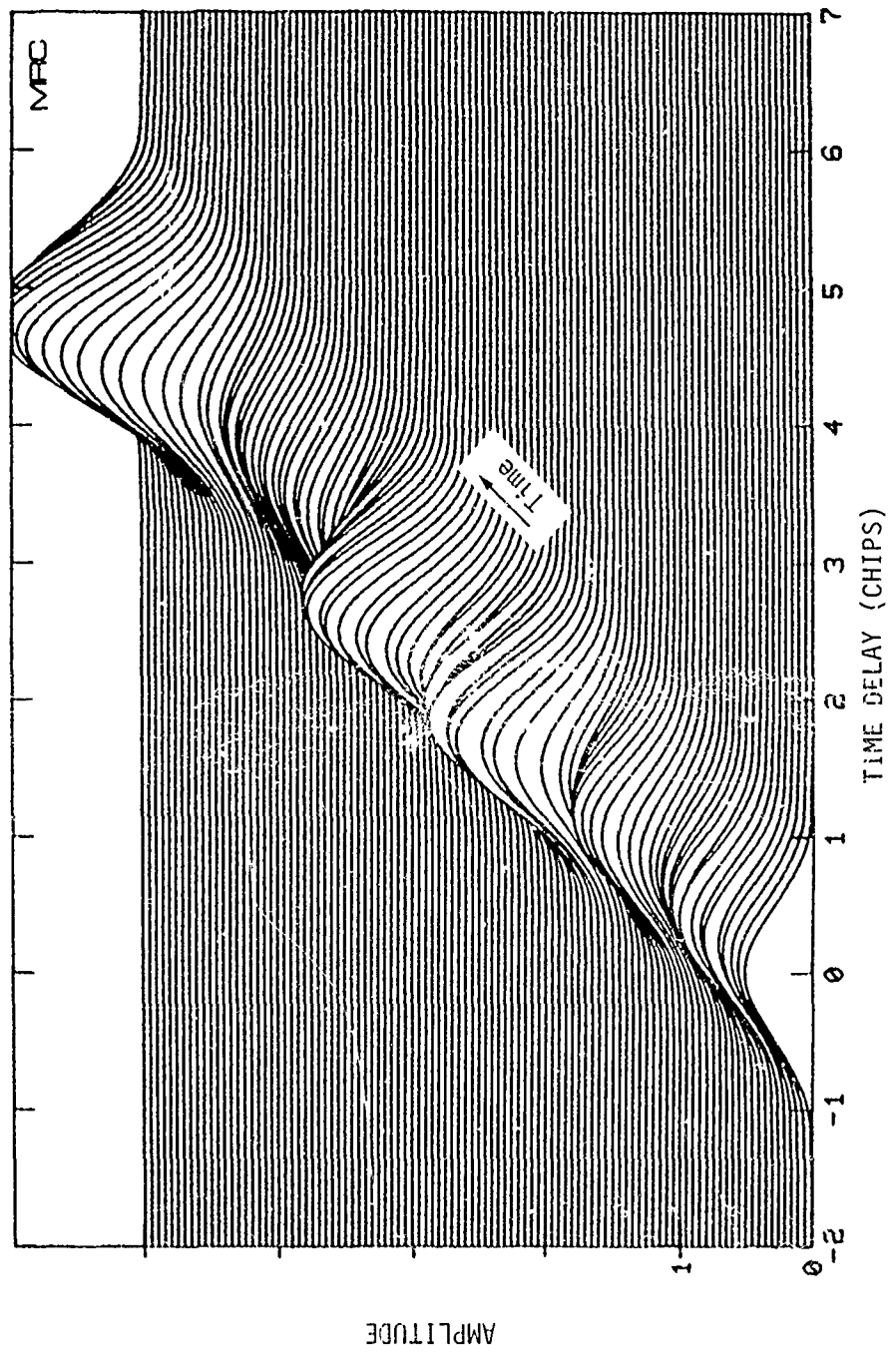


Figure 3-2. PN code autocorrelation function in a nonselective fading environment.

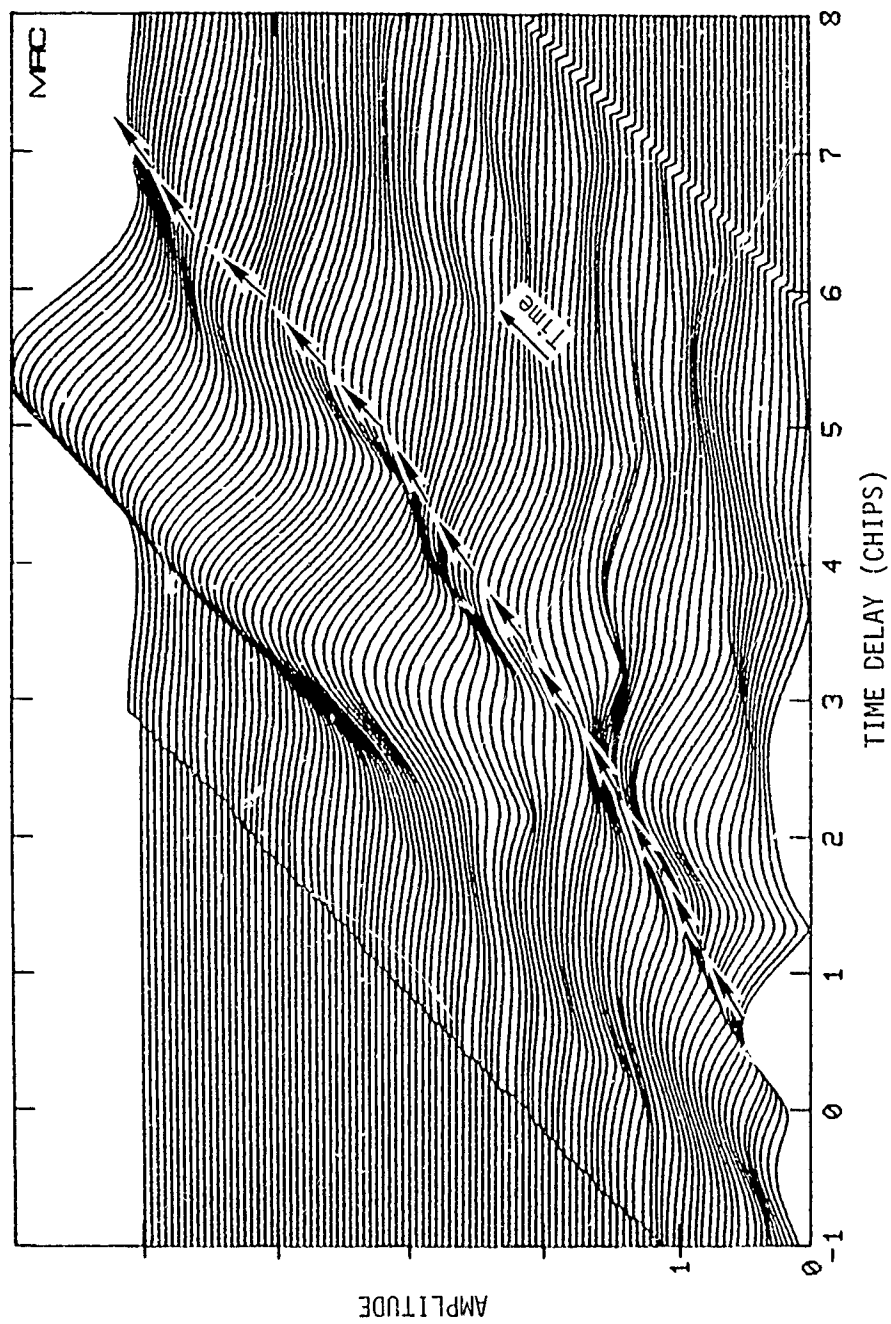


Figure 3-3. PN code autocorrelation function in a frequency-selective environment. The arrows show the locus of the peak tracked by the receiver code loop.

Near the front of the figure, the time delay estimate is about one-half chip with the receiver code loop correctly tracking the peak of the code correlator output. However, in this example, the details of the code correlation function time development cause the code loop to follow a misleading path, indicated by the arrows in the three-dimensional plot, so that the time delay error increases to about two chips during the brief time interval shown. At this point, the code loop is no longer tracking the main peak of the code correlation function, but rather it is following an extended side-lobe. (Later in this particular simulation the delay estimate drops back to around one-half chip.)

As can be seen from the discussion above, accurate calculation of the PN code correlator output is necessary to adequately simulate the operation of the X-set receiver. In the following, a method is given to realistically model the X-set PN code correlation operation in the presence of frequency-selective scintillation and dispersion.

### 3.2 THEORETICAL DEVELOPMENT - RECEIVED WAVEFORM

Let the real waveform transmitted by the satellite be expressed as

$$\begin{aligned} x(t) &= \operatorname{Re} \left\{ m(t) e^{j\omega_0 t} \right\} \\ &= \frac{1}{2} m(t) e^{j\omega_0 t} + \frac{1}{2} m^*(t) e^{-j\omega_0 t} \end{aligned} \quad (3-1)$$

where  $\omega_0$  is the carrier angular frequency and  $m(t)$  is the modulation waveform. For a pseudonoise (PN) code,  $m(t)$  consists of a long sequence of pseudorandom polarity changes (binary PSK-modulated signal). The frequency-domain representation of the transmitted waveform is given by

$$\begin{aligned} X(\omega) &= \int_{-\infty}^{\infty} x(t) e^{-j\omega t} dt \\ &= \frac{1}{2} \int_{-\infty}^{\infty} m(t) e^{j(\omega_0 - \omega)t} dt + \frac{1}{2} \int_{-\infty}^{\infty} m^*(t) e^{-j(\omega_0 + \omega)t} dt \\ &= \frac{1}{2} M(\omega - \omega_0) + \frac{1}{2} M^*(-\omega - \omega_0) \end{aligned} \quad (3-2)$$

where  $M(\omega)$  is the Fourier transform of the modulation waveform:

$$M(\omega) = \int_{-\infty}^{\infty} m(t) e^{-j\omega t} dt \quad (3-3)$$

Now after propagation through an ionized medium for a distance  $z_t$ , the signal spectrum is given by

$$V(\omega) = X(\omega) e^{j\psi(\omega)} \quad (3-4)$$

where the term  $\exp[j\theta(\omega)]$  is the transfer function of the ionized medium. For a "smooth" plasma, with no striations and negligible electron collisions, the transfer function is

$$\theta(\omega) = -\frac{\omega}{c} \int_0^{z_t} \left(1 - \frac{\omega_p^2}{\omega^2}\right)^{1/2} dz \quad (3-5)$$

where  $z_t$  is the propagation distance through the ionized medium,  $c$  is the speed of light, and  $\omega_p$  is the plasma frequency. In terms of the mean electron density  $N_e$

$$\omega_p^2 = 4\pi c^2 r_e N_e \quad (3-6)$$

where  $r_e$  is the classical electron radius ( $2.82 \times 10^{-15}$  m). Thus after propagation through a smooth plasma, the spectrum of the received waveform is obtained from Equations 3-2 and 3-4 as

$$V(\omega) = \frac{1}{2} M(\omega - \omega_0) e^{j\theta(\omega)} + \frac{1}{2} M^*(-\omega - \omega_0) e^{j\theta(\omega)} \quad (3-7)$$

Now in the first term of Equation 3-7 expand  $\theta(\omega)$  in a Taylor series about  $\omega_0$ :

$$\theta_+(\omega) = \theta(\omega_0) + (\omega - \omega_0)\theta'(\omega_0) + \frac{(\omega - \omega_0)^2 \theta''(\omega_0)}{2!} + \dots \quad (3-8)$$

where the subscripted plus sign signifies the expansion about a positive carrier frequency and the primes denote differentiation with respect to  $\omega$ . From Equation 3-5

$$\theta(\omega_0) = -\frac{\omega_0}{c} \int_0^{z_t} \left(1 - \frac{\omega_p^2}{\omega_0^2}\right)^{1/2} dz \quad (3-9)$$

$$\theta'(\omega_0) = -\frac{1}{c} \int_0^{z_t} \left(1 - \frac{\omega_p^2}{\omega_0^2}\right)^{-1/2} dz \quad (3-10)$$

$$\theta''(\omega_0) = \frac{1}{c\omega_0^3} \int_0^{z_t} \left(1 - \frac{\omega_p^2}{\omega_0^2}\right)^{-3/2} \omega_p^2 dz \quad (3-11)$$

$$\theta'''(\omega_0) = -\frac{3}{c\omega_0^4} \int_0^{z_t} \left(1 - \frac{\omega_p^2}{\omega_0^2}\right)^{-5/2} \omega_p^2 dz \quad (3-12)$$

In the second term of Equation 3-7, expand  $\theta(\omega)$  in a Taylor series about  $-\omega_0$ :

$$\begin{aligned} \theta_-(\omega) &= \theta(-\omega_0) + (\omega + \omega_0)\theta'(-\omega_0) + \frac{(\omega + \omega_0)^2 \theta''(-\omega_0)}{2!} + \dots \\ &= -\theta(\omega_0) - (-\omega - \omega_0)\theta'(\omega_0) - \frac{(-\omega - \omega_0)^2 \theta''(\omega_0)}{2!} + \dots \quad (3-13) \end{aligned}$$

For notational simplicity, let  $\theta(\omega_0) = \theta_0$ ,  $\theta'(\omega_0) = \theta'_0$  and so forth. Retaining the first four terms in the Taylor series, the received waveform for smooth plasma effects is

$$\begin{aligned} v(t) &= \frac{1}{2\pi} \int_{-\infty}^{\infty} V(\omega) e^{j\omega t} d\omega \\ &= \frac{1}{4\pi} \int_{-\infty}^{\infty} M(\omega - \omega_0) e^{j\theta_+(\omega)} e^{j\omega t} d\omega + \frac{1}{4\pi} \int_{-\infty}^{\infty} M^*(-\omega - \omega_0) e^{j\theta_-(\omega)} e^{j\omega t} d\omega \\ &= \frac{1}{4\pi} \int_{-\infty}^{\infty} M(\omega - \omega_0) e^{j\theta_0} e^{j(\omega - \omega_0)\theta'_0} e^{j\frac{1}{2}(\omega - \omega_0)^2 \theta''_0} e^{j\frac{1}{6}(\omega - \omega_0)^3 \theta'''_0} e^{j\omega t} d\omega \\ &\quad + \frac{1}{4\pi} \int_{-\infty}^{\infty} M^*(-\omega - \omega_0) e^{-j\theta_0} e^{-j(-\omega - \omega_0)\theta'_0} e^{-j\frac{1}{2}(-\omega - \omega_0)^2 \theta''_0} e^{-j\frac{1}{6}(-\omega - \omega_0)^3 \theta'''_0} e^{j\omega t} d\omega \quad (3-14) \end{aligned}$$

In the first integral use the substitution  $v = \omega - \omega_0$ . In the second integral let  $v = -\omega - \omega_0$ . Then Equation 3-14 becomes

$$v(t) = \frac{e^{j(\omega_0 t + \theta_0)}}{4\pi} \int_{-\infty}^{\infty} M(v) e^{j(\frac{1}{2}\theta_0'' v^2 + \frac{1}{6}\theta_0''' v^3)} e^{jv(t-t_0)} dv + \frac{e^{-j(\omega_0 t + \theta_0)}}{4\pi} \int_{-\infty}^{\infty} M^*(v) e^{-j(\frac{1}{2}\theta_0'' v^2 + \frac{1}{6}\theta_0''' v^3)} e^{-jv(t-t_0)} dv \quad (3-15)$$

where  $\theta_0$  can be seen to be the total mean phase shift at the carrier frequency and  $t_0$  is the mean group time delay (i.e., the group delay at the carrier frequency):

$$\theta_0 = -\frac{\omega_0 z}{c} \int_0^z \left( i - \frac{\omega_p^2}{\omega_0^2} \right)^{1/2} dz \quad (3-9)$$

$$t_0 \triangleq -\theta_0' = \frac{1}{c} \int_0^z \left( 1 - \frac{\omega_p^2}{\omega_0^2} \right)^{-1/2} dz \quad (3-16)$$

For cases of interest where  $\omega_0^2 \gg \omega_p^2$  (otherwise the wave cannot propagate without severe attenuation),  $\theta_0$  and  $t_0$  can be expressed as:

$$\theta_0 = -\frac{\omega_0 z t}{c} + \frac{2\pi e r}{\omega_0} \int_0^z N_e dz \quad (3-17)$$

$$t_0 = \frac{z t}{c} + \frac{2\pi e r}{\omega_0^2} \int_0^z N_e dz \quad (3-18)$$

where the first terms above are the free-space contribution, and the second terms are proportional to the total electron content. Note that the second term in Equation 3-15, arising from the negative frequency spectral components, is the complex conjugate of the first term. Thus the received waveform  $v(t)$  is real, as it should be.

Now consider the possible frequency-selective effects of a striated plasma. Let  $H(\nu)$ , where  $\nu = \omega - \omega_0$ , denote the complex signal received after propagation of a plane wave at a positive frequency  $\omega$  through the striated plasma. As illustrated in Reference 3-2,  $H(\nu)$  is the received signal computed from a multiple phase screen (MPS) calculation of propagation through an ionized region. It is clear from Equation 3-15 that  $H(\nu)$  modifies the positive frequency spectral components and that  $H^*(\nu)$  modifies the negative frequency spectral components. Thus the received waveform including both smooth and striated plasma disturbances is given by

$$\begin{aligned}
 v(t) = & \frac{e^{j(\omega_0 t + \theta_0)}}{4\pi} \int_{-\infty}^{\infty} M(\nu) H(\nu) e^{j\left(\frac{1}{2}\theta_0'' \nu^2 + \frac{1}{6}\theta_0''' \nu^3\right)} e^{j\nu(t-t_0)} d\nu \\
 & + \frac{e^{-j(\omega_0 t + \theta_0)}}{4\pi} \int_{-\infty}^{\infty} M^*(\nu) H^*(\nu) e^{-j\left(\frac{1}{2}\theta_0'' \nu^2 + \frac{1}{6}\theta_0''' \nu^3\right)} e^{-j\nu(t-t_0)} d\nu
 \end{aligned}
 \tag{3-19}$$

This waveform at the receiver input can be written in terms of a complex modulation envelope,

$$\begin{aligned}
 v(t) = & \frac{1}{2} E(t-t_0) e^{j(\omega_0 t + \theta_0)} + \frac{1}{2} E^*(t-t_0) e^{-j(\omega_0 t + \theta_0)} \\
 = & \operatorname{Re} \left\{ E(t-t_0) e^{j(\omega_0 t + \theta_0)} \right\}
 \end{aligned}
 \tag{3-20}$$

where the complex modulation envelope is

$$E(t-t_0) = \frac{1}{2\pi} \int_{-\infty}^{\infty} M(\nu) H(\nu) e^{j\left(\frac{1}{2}\theta_0'' \nu^2 + \frac{1}{6}\theta_0''' \nu^3\right)} e^{j\nu(t-t_0)} d\nu
 \tag{3-21}$$

Note that Equation 3-20 has the same general form as Equation 3-1 — a wave modulated on a carrier at angular frequency  $\omega_0$  with an additional time delay and phase shift as given by Equations 3-17 and 3-18.

### 3.3 X-SET PN CODE CORRELATION OPERATION

The X-set receiver simulation documented in Reference 3-1 is a direct sampled-data digital implementation of the GPS X-set receiver described in Reference 3-3. The simulation includes implementation of the local reference generator/correlator and signal conditioner, AFC/Costas carrier loop, PN code loop, AGC loop, and rate multiplier/incremental phase modulators. Figures 3-4 and 3-5 show functional diagrams of the implementation of the AFC/Costas loop and the PN code tracking loop, respectively.

The details of the various frequency conversions preceding the inphase and quadrature channel product detectors are treated in Reference 3-1 but are unimportant to the analysis here. For the following development, the simple block diagram of Figure 3-6 will suffice.

In the X-set spread spectrum receiver, the received waveform  $v(t)$  is multiplied by a time-shifted replica of the PN modulation waveform  $m(t)$ , which has been modulated onto a local reference carrier. The locally generated real PN waveform is represented by

$$u_1(t) = m(t-t_1) e^{j(\omega_1 t + \theta_1(t))} + m^*(t-t_1) e^{-j(\omega_1 t + \theta_1(t))} \quad (3-22)$$

where  $t_1$  is the receiver estimate of the propagation time delay,  $\theta_1(t)$  is the receiver estimate of signal phase shift, and  $\omega_1$  is the local oscillator frequency ( $\omega_1 < \omega_0$ ).

The output of the multiplier (mixer) whose inputs are  $v(t)$  and  $u_1(t)$  is

$$\begin{aligned} v(t)u_1(t) &= \frac{1}{2} E(t-t_0) m^*(t-t_1) e^{j(\omega_2 t + \phi(t))} \\ &+ \frac{1}{2} E^*(t-t_0) m(t-t_1) e^{-j(\omega_2 t + \phi(t))} = w(t) \end{aligned} \quad (3-23)$$



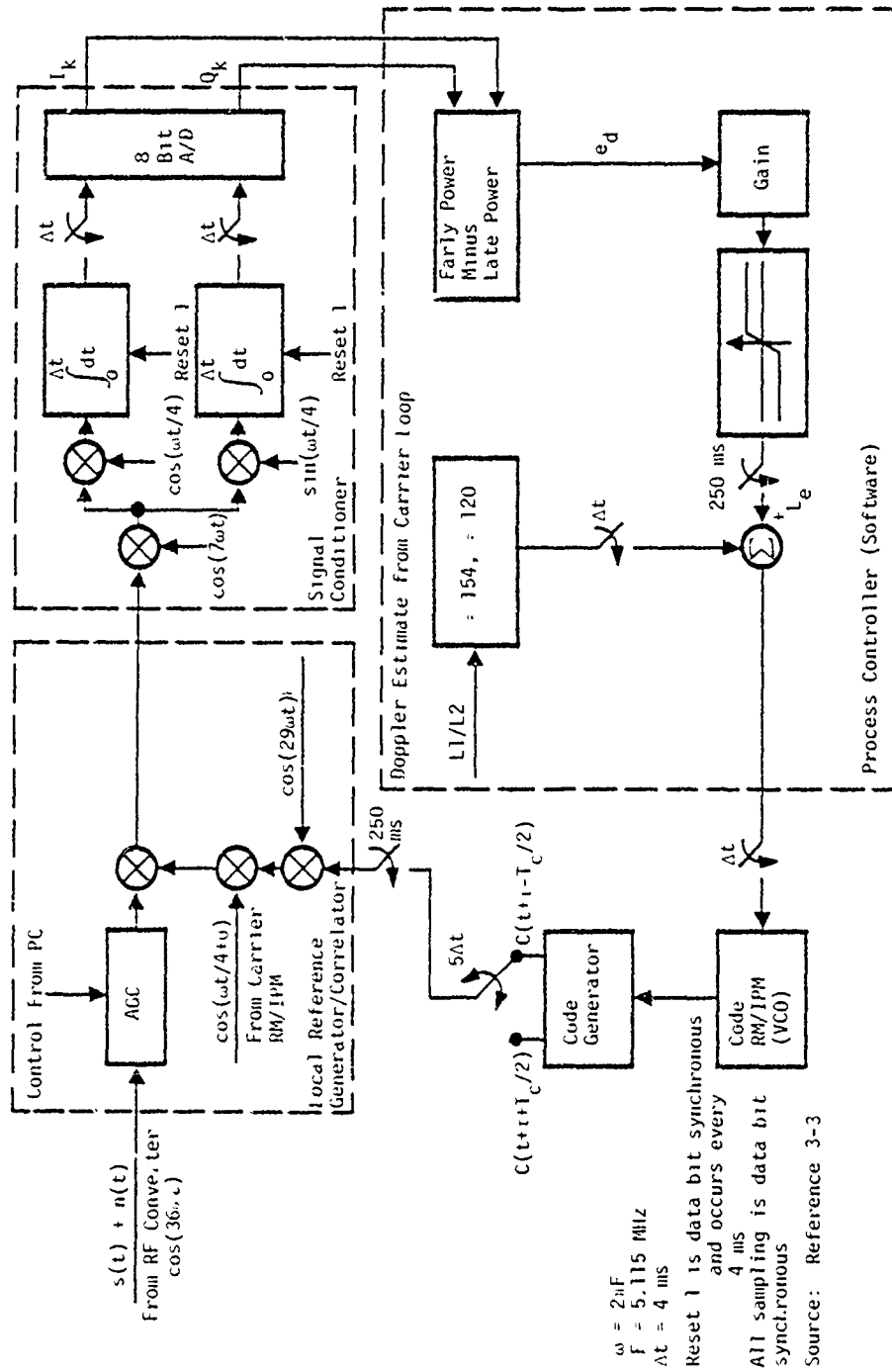


Figure 3-5. X-set PN code tracking loop implementation.

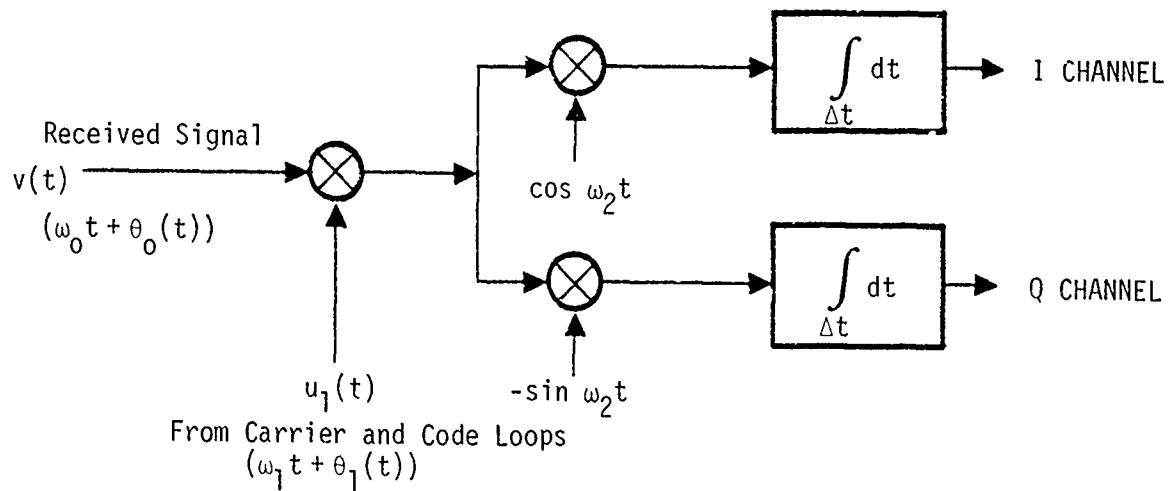


Figure 3-6. Simplified block diagram of code correlator operation and I-Q sampling.

where the sum-frequency components have been removed by filtering, leaving only the difference-frequency components. The difference frequency is given by

$$\omega_2 = \omega_0 - \omega_1 \quad (3-24)$$

and  $\phi$  is the error in the receiver estimate of carrier phase:

$$\phi \triangleq \phi(t) = \theta_0(t) - \theta_1(t) \quad (3-25)$$

The waveform  $w(t)$  is now mixed with two quadrature sinusoids,  $\cos\omega_2 t$  and  $-\sin\omega_2 t$ , to form two baseband channels in the receiver. After double-frequency components are filtered out, these baseband voltages are given by:

$$i(t) = \frac{1}{2} \left[ E(t-t_0) m^*(t-t_1) e^{j\phi} + E^*(t-t_0) m(t-t_1) e^{-j\phi} \right] \quad (3-26)$$

$$q(t) = \frac{1}{2j} \left[ E(t-t_0) m^*(t-t_1) e^{j\phi} - E^*(t-t_0) m(t-t_1) e^{-j\phi} \right] \quad (3-27)$$

These two quadrature channel signals can be rewritten as

$$i(t) = \text{Re} \left\{ E(t-t_0) m^*(t-t_1) e^{j\phi} \right\} \quad (3-28)$$

$$q(t) = \text{Im} \left\{ E(t-t_0) m^*(t-t_1) e^{j\phi} \right\} \quad (3-29)$$

The two baseband voltages are integrated over a time interval  $\Delta t$  to form  $I$  and  $Q$  samples for subsequent digital processing in the receiver. Since integration is a linear process it is clear that the  $I$  and  $Q$  samples are given by the real and imaginary parts of the integral:

$$\begin{aligned} \rho(t_0, t_1) &= \int_{t_1 - \frac{\Delta t}{2}}^{t_1 + \frac{\Delta t}{2}} E(t-t_0) m^*(t-t_1) e^{j\phi} dt \\ &= \int_{-\frac{\Delta t}{2}}^{\frac{\Delta t}{2}} E(t'+\tau) m^*(t') e^{j\phi} dt' \end{aligned} \quad (3-30)$$

where  $t' = t - t_1$  references the time to the receiver, and  $\tau$  is the error in the receiver estimate of propagation time delay through the medium,  $\tau = t_1 - t_0$ . As stated earlier,  $t$  is the satellite or transmitter time,  $t_1$  is the receiver estimate of propagation time delay, and  $t_0$  is the actual propagation time delay.

Using Equation 3-21 in Equation 3-30, the equation for  $\rho$  becomes

$$\rho(\tau) = \int_{-\frac{\Delta t}{2}}^{\frac{\Delta t}{2}} \left[ \frac{1}{2\pi} \int_{-\infty}^{\infty} M(\nu) F(\nu) e^{j\nu(t'+\tau)} d\nu \right] m^*(t') e^{j\phi} dt' \quad (3-31)$$

where  $F(\nu)$  is the total plasma frequency-selective transfer function, including both smooth and striated plasma components:

$$F(\nu) = H(\nu) e^{j\left(\frac{1}{2} \theta_0'' \nu^2 + \frac{1}{6} \theta_0''' \nu^3\right)} \quad (3-32)$$

If the propagation disturbances do not vary significantly with time over the receiver sampling period, that is, if  $F(\nu)$  and  $\phi$  are essentially constant over the time interval  $\Delta t$ , then Equation 3-32 can be rewritten as

$$\rho(\tau) \approx \frac{e^{j\phi}}{2\pi} \int_{-\infty}^{\infty} M(\nu) F(\nu) e^{j\nu\tau} \int_{-\frac{\Delta t}{2}}^{\frac{\Delta t}{2}} m^*(t') e^{j\nu t'} dt' d\nu \quad (3-33)$$

In the X-set, the integration period  $\Delta t$  is 4 ms which encompasses 40,920 chips of the PN code sequence. In this case, the limits on the  $t'$  integral can be set to infinity with little error. Thus

$$M^*(\nu) = \lim_{\Delta t \rightarrow \infty} \int_{-\frac{\Delta t}{2}}^{\frac{\Delta t}{2}} m^*(t') e^{j\nu t'} dt' \quad (3-34)$$

and Equation 3-33 reduces to

$$\rho(\tau) = \frac{e^{j\phi}}{2\pi} \int_{-\infty}^{\infty} |M(\nu)|^2 F(\nu) e^{j\nu\tau} d\nu \quad (3-35)$$

$|M(\nu)|^2$ , the squared magnitude of the Fourier transform of the modulation waveform, is the power spectrum of the PN sequence, given by the Fourier transform of the PN code autocorrelation function  $(1 - |\tau|/T_c)$ , where  $T_c$  is the PN code chip period (Reference 3-4, p. 341). Thus

$$|M(\nu)|^2 = T_c \left( \frac{\sin \nu T_c / 2}{\nu T_c / 2} \right)^2 \quad (3-36)$$

As a check for nonselective cases (no scintillation and no dispersion),  $F(\nu)$  is unity, and the use of Equation 3-36 in Equation 3-35 yields.

$$\rho(\tau) = e^{j\phi} \left( 1 - \frac{|\tau|}{T_c} \right) \quad (3-37)$$

as it should.

In general,  $F(v)$  is not unity because of fading, dispersion and frequency-selective scintillation disturbances. Equation 3-35 is a general expression that provides the PN code correlation output amplitude and phase (I and Q baseband channels) for any type of propagation condition.

### 3.4 COMPUTATIONAL CONSIDERATIONS

Equation 3-35 can be evaluated by discrete Fourier transform techniques. The X-set receiver requires the value of the code correlator output at only one (or two) specified values of time delay (or advance) at a given simulation time (Reference 3-1). Thus the use of a simple discrete Fourier transform (DFT) algorithm is more efficient than the use of fast Fourier transform (FFT) techniques. Since DFT's do not assume a fixed sampling interval (as do FFT's), this procedure is more general than FFT techniques and requires less CPU time for this particular application.

At each simulation time, an array of Fourier coefficients is formed at a set of  $N$  discrete frequencies across the PN signal bandwidth. Each Fourier coefficient consists of three multiplicative factors: the PN signal power spectrum  $|M(\nu)|^2$  computed from Equation 3-36, frequency-selective propagation factors  $H(\nu)$  computed using the MPS technique, and dispersive effects due to the mean total electron content (TEC) computed from Equations 3-9 through 3-12. The phase shift and time delay due to the mean TEC are given in Equations 3-17 and 3-18. The corresponding higher-order dispersive terms are found from Equations 3-11 and 3-12 to be

$$\frac{1}{2} \theta_0'' = \frac{2\pi c r_e}{\omega_0^3} \int_0^{z_t} N_e dz \quad (3-38)$$

$$\frac{1}{6} \theta_0''' = - \frac{2\pi c r_e}{\omega_0^4} \int_0^{z_t} N_e dz \quad (3-39)$$

where it has again been assumed that  $\omega_0^2 \gg \omega_p^2$ , which is valid in all cases of interest here.

Once the array of frequency-selective Fourier coefficients  $C(n)$  has been computed at a given simulation time, the following DFT algorithm

is used to compute the PN code correlator output amplitude and phase at any specified value of time delay:

$$\rho(\tau) = \sum_{n=-N/2+1}^{N/2-1} C(n)e^{jn2\pi\Delta f\tau} + C(N/2)\cos(N\pi\Delta f\tau) \quad (3-40)$$

where  $\Delta f$  is the frequency spacing between each of the  $N$  frequencies ( $N$  even). The corresponding unambiguous range of time delay  $\tau$  (DFT computational window) is equal to  $1/\Delta f$ .

Frequency-selective propagation disturbances introduce additional mean time delay, in excess of that given by Equation 3-18, and cause  $\rho(\tau)$  to be generally asymmetrical and shifted toward positive  $\tau$  (increased delay). Therefore the DFT computational window is not centered about  $\tau=0$  but rather is shifted to larger values of delay and centered around a positive value of  $\tau$ . For example, with 32 frequencies in a bandwidth of  $2/T_c$ , where  $T_c$  is the PN chip period, the DFT window is set at  $-2T_c \leq \tau \leq 14 T_c$ .

## REFERENCES

- 3-1. Bogusch, R. L., and D. L. Knepp, Propagation Effects on GPS Receiver Model X, Mission Research Corporation, January 1978 (Unpublished).
- 3-2. Knepp, D. L., Multiple Phase-Screen Propagation Analysis for Defense Satellite Communications System, DNA 4424T, MRC-R-332, Mission Research Corporation, September 1977.
- 3-3. Stonestreet, W. M., A Functional Description of the NAVSTAR GPS Receiver Model X, R-981, The Charles Stark Draper Laboratory, Inc., Final Report for SAMSO Contract F04701-75-C-0212, Volume I, 26 April 1976, Revised February 1977.
- 3-4. Papoulis, A., Probability, Random Variables, and Stochastic Processes, McGraw-Hill, New York, 1965.

## SECTION 4 PROPAGATION AND X-SET PERFORMANCE

In this section, examples of signal scintillation are presented for propagation through barium clouds at frequencies of 250, 200, and 150 MHz. These propagation calculations are based on the barium cloud models discussed in Section 2 and represent the propagation environment for two different barium clouds (Esther and Fern) observed at 48 and 43 minutes after barium release, respectively.

Detailed examples of propagation conditions are given which show the development of the received signal with propagation distance, the effect of the deterministic barium cloud, and the effects of inner scale size. Examples are presented showing the distortion of the PN code correlator output for carrier frequencies of 150 and 200 MHz.

This section also includes several detailed examples of the performance of the X-set receiver operating at a carrier frequency of 150 MHz for two values of the mean carrier power-to-noise density ratio. The examples graphically illustrate the phase, frequency, and code tracking performance of the X-set in a striated barium environment.

#### 4.1 NUMERICAL BARIUM CLOUD MODEL

As discussed in Section 2, a statistical phase screen model for barium clouds Esther (48 minutes after release) and Fern (43 minutes after release) was developed to use as input to the propagation simulation. The model consists of a deterministic mean barium cloud represented by a large gaussian shape to which is added random phase irregularities generated using previously developed algorithms (Reference 4-1). The random phase is cutoff by a smooth window so that no phase irregularities appear outside the large gaussian phase structure. This phase screen representation for a barium cloud is described by the equation

$$\begin{aligned} \phi_0(x) = & \phi_0 e^{-\frac{(x-x_m)^2}{r_0^2}} \\ & + \phi(x) e^{-\frac{(x-x_m+\ell_c)^2}{r_c^2}} U(x_m-\ell_c-x) \\ & + \phi(x) e^{-\frac{(x-x_m-\ell_c)^2}{r_c^2}} U(x-x_m-\ell_c) \\ & + \phi(x) [U(x-x_m+\ell_c) - U(x-x_m-\ell_c)] \end{aligned} \quad (4-1)$$

$$U(x) = \begin{cases} 1 & , \quad x \geq 0 \\ 0 & , \quad x < 0 \end{cases} \quad (4-2)$$

where the first term represents the deterministic barium cloud with a maximum phase of  $\phi_0$  and a half-width of  $r_0$ . The barium cloud is centered at  $x_m$  which is always chosen as the middle of the MPS grid.  $\phi(x)$  is a random phase structure which is generated using the statistical properties of the phase fluctuations as determined in the analysis described in Section 2. Since the propagation algorithm generates  $\phi(x)$  as a homogeneous function over the entire MPS grid, simply adding  $\phi(x)$  to the first term in Equation 4-1 would yield a structural barium cloud with striations off to the side. Thus the last three terms in Equation 4-1 are included to add a windowed version of  $\phi(x)$  to the mean gaussian phase representing the

deterministic barium cloud. As is evident from Equation 4-1 the window is unity from  $x_m - \ell_c$  to  $x_m + \ell_c$ , and is cutoff by gaussian functions of half-width  $r_c$  beginning at  $x = x_m - \ell_c$  and  $x = x_m + \ell_c$ . Figures 2-7 and 2-13 show examples of the phase screen models of Esther at 48 minutes after barium release and Fern at 43 minutes after barium release. Table 4-1 lists the parameters necessary to generate phase screen models of barium clouds with the MPS propagation simulation.

Table 4-1. Barium cloud parameters used in predictions for the PLACES experiment.

Barium Cloud	$\sigma_\phi^*$	$L_0$	m	$\phi_0^*$	$r_0$	$\ell_c$	$r_c$
Esther (48 min)	9.7 rad	360 m	3	82 rad	5 km	5 km	1 km
Fern (43 min)	4.9 rad	270 m	3.5	125 rad	3 km	4 km	0.3 km

\*  $\sigma_\phi$  and  $\phi_0$  as listed correspond to a frequency of 340 MHz.

As discussed above, the phase fluctuations are represented by a power-law PSD of the form

$$S(K) = \frac{\sigma_\phi^2 \Gamma(\frac{m}{2}) L_0 \exp(-K^2 \ell_i^2)}{\sqrt{\pi} \Gamma(\frac{m-1}{2}) (1+K^2 L_0^2)^{m/2}} \quad (4-3)$$

where  $\Gamma$  is the gamma function,  $K$  is the spatial wavenumber,  $m$  is the spectral index and  $L_0$  is the outer scale. The inner scale,  $\ell_i$ , is here used explicitly to cutoff the spectrum. In some cases, the value  $\ell_i$  is set to zero. Under this circumstance, the value of the inner scale is effectively set by the minimum distance between points on the MPS grid. As discussed in Section 2.3, this minimum distance of 1.831 m corresponds to an effective inner scale of 0.58 m.

We have found that utilization of the complete barium cloud model, including the mean barium cloud, although more appropriate for actual experimental predictions, complicates a systematic comparison of numerical results to theoretical results. This problem arises because current theoretical formulations demand a homogeneous environment while the barium cloud model consists of a striated cloud-like formation with free space to either side—an inhomogeneous environment. For this reason, a number of different simulations have been utilized, with and without the mean barium cloud, and are presented in the succeeding sections.

## 4.2 SIGNAL PROPAGATION

To model the proposed geometry of the PLACES experiment, a single phase screen representation of the barium cloud is used. A plane wave is then propagated through the phase screen to a receiver plane 100 km away. For a thin scattering medium along the direction of propagation, this plane wave geometry is equivalent to a spherical wave geometry where the random medium lies between the transmitter and receiver such that

$$\frac{1}{100 \text{ km}} = \frac{1}{z_t} + \frac{1}{z_r} \quad (4-4)$$

where  $z_t$  and  $z_r$  are the distances of the transmitter and receiver from the barium cloud.\* Equation 4-4 is simply the result of the added angular spreading of the spherical wave (Reference 4-2).

### 4.2.1 Propagation Results

Detailed examples of the numerical propagation results are presented in this subsection. For Esther at 150 MHz, the signal amplitude and phase are shown as a function of propagation distance from the barium cloud. The effect of the mean barium cloud is shown as well as the effect of inner scale size variation. Results for the received signal amplitude at 100 km propagation distance are presented for both Esther and Fern at frequencies of 150, 200, and 250 MHz.

Figure 4-1 shows a phase screen representation of Esther where the mean barium cloud part of the model has been deliberately omitted. This representation was generated using the PSD parameters listed in Table 4-1 along with an assumed inner scale of 10 m. The phase shown has both positive and negative portions and represents a portion of a zero mean random process.

---

\* Current experimental plans call for transmission from a rocket borne transmitter through a striated barium cloud to a ground based receiver.

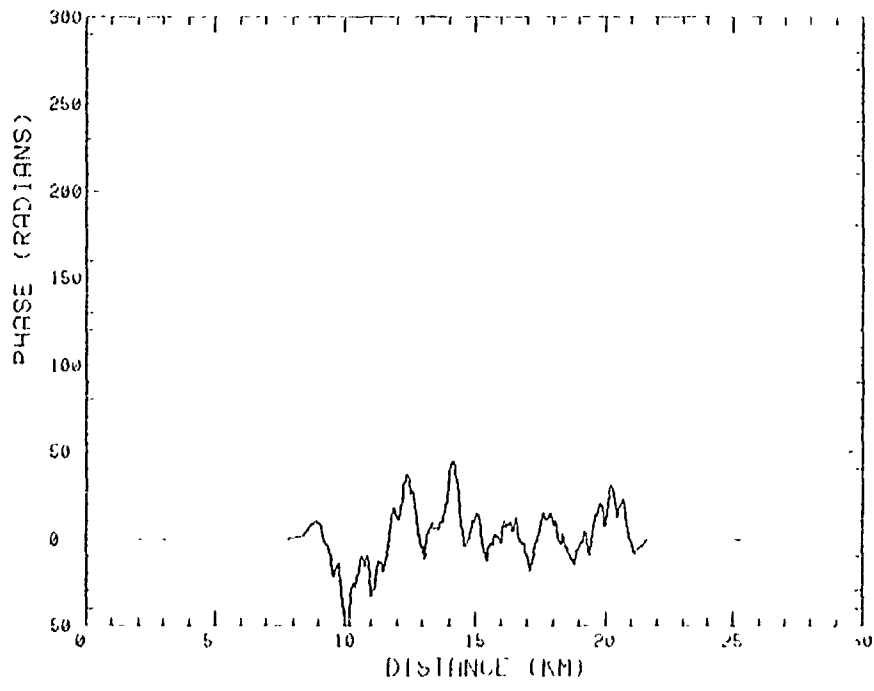


Figure 4-1. Phase screen representation of Esther at 150 MHz with no deterministic barium cloud.

Note that the MPS propagation simulation is two-dimensional with no variation perpendicular to the page. This is often a reasonable assumption in ionospheric propagation cases where there is little variation parallel to the magnetic field direction. A wave (initially plane as it enters the striated region) is then propagated numerically downwards to the receiver by the use of the Fresnel-Kirchhoff integral equation. As the wave propagates, it is possible to trace the signal development.

Figure 4-2 shows the amplitude (in decibels relative to the mean amplitude) and phase resulting after propagating a distance of 1 km from the striation location. At this point severe amplitude fluctuations have already developed. At the 1 km propagation distance, however, the signal phase still resembles the phase at the striation location, although there is a tendency for the dominance of positive values of phase. These increasing signal phase values correspond to increasing signal time delay due to propagation along longer paths resulting from angular scattering by the random striations.

Figures 4-3 to 4-7 show the development of the signal amplitude and phase as the propagation distance gradually increases to 100 km. In the phase plots, the values shown correspond to additional phase increments after the free space phase delay ( $e^{-jk_0z}$ ) is removed. Thus only the effects of the striations are shown. When the propagation distance is small, energy reaching a particular point can originate only from a relatively small portion of the striations and hence cause only a relatively small time delay. As the propagation distances increases, energy from a larger portion of the barium cloud can reach a particular observer by angular scattering. Larger time delay and the associated greater phase advance shown in the figures arise because of these angular scattering effects.

Also note the increased spreading of the signal due to angular scattering which becomes more important as the propagation distance increases. This is particularly evident in the amplitude behavior at the larger propagation distances shown.

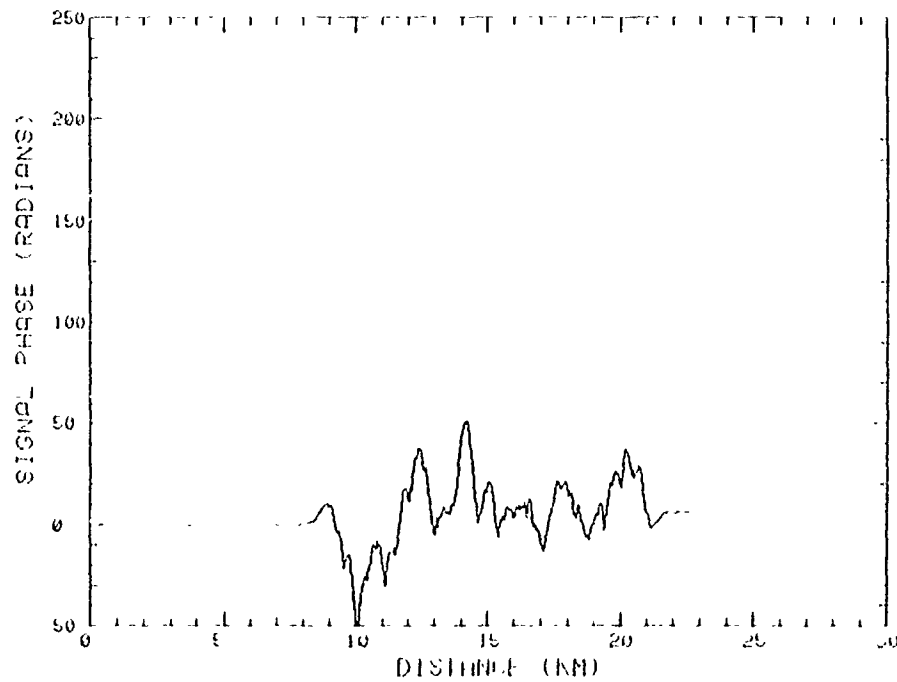
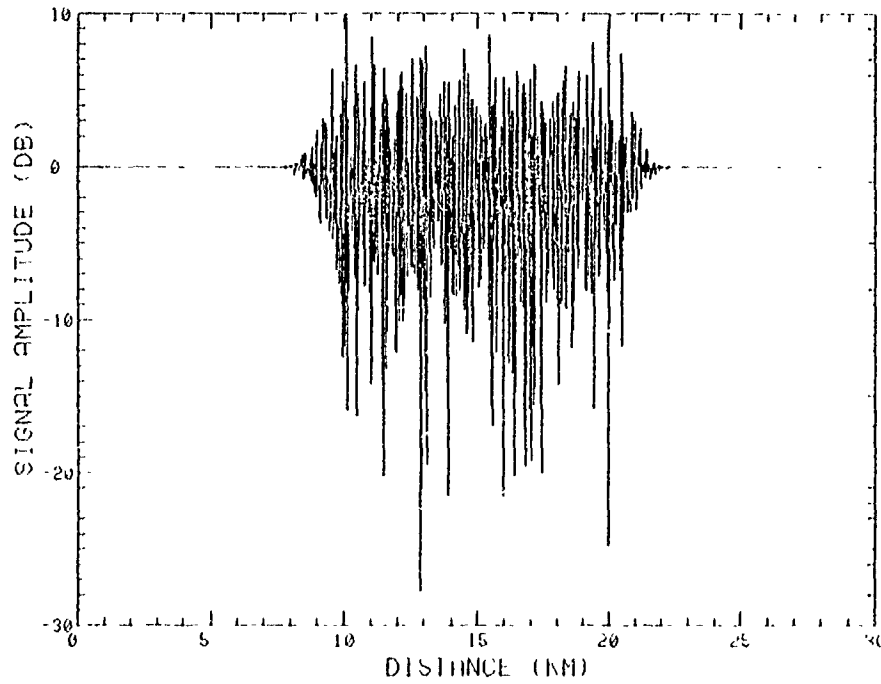


Figure 4-2. Signal amplitude and phase at a propagation distance of 1 km.

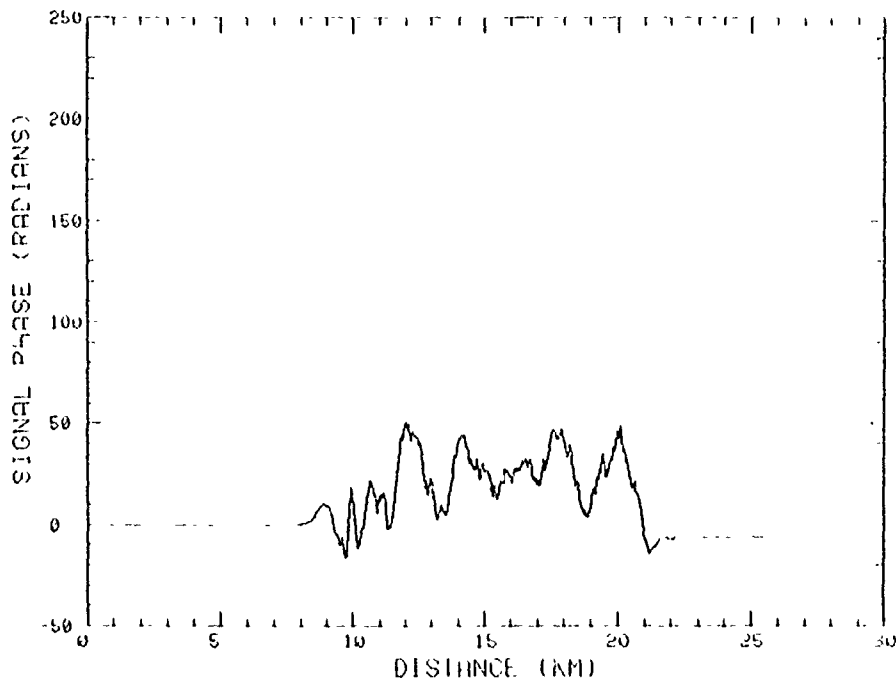
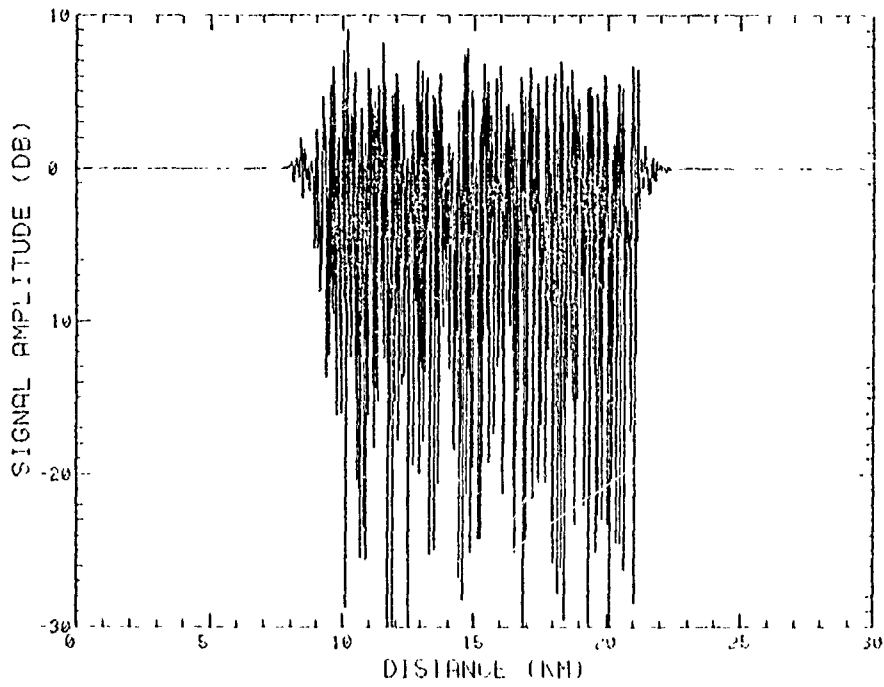


Figure 4-3. Signal amplitude and phase at a propagation distance of 4 km.

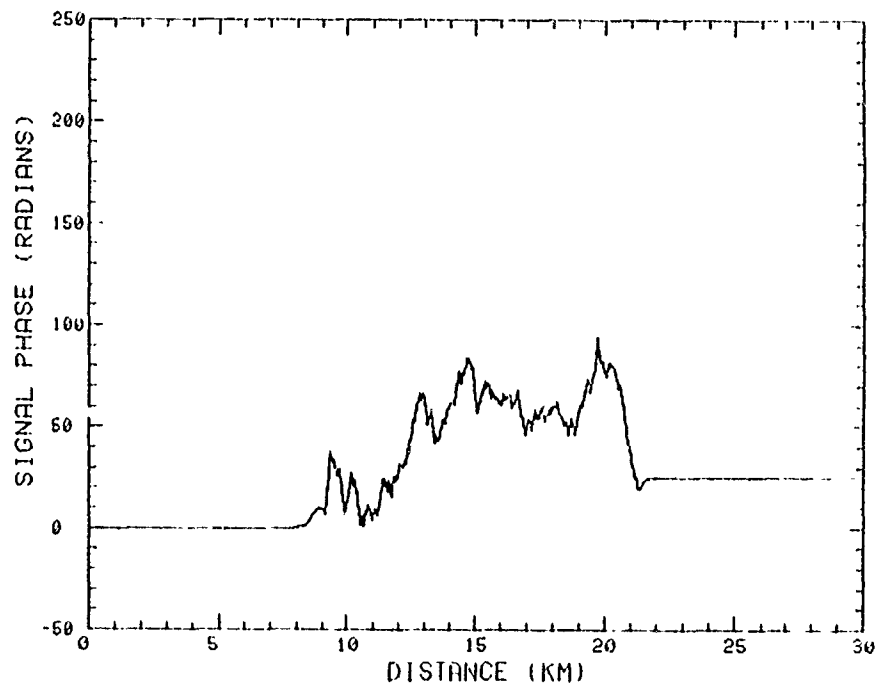
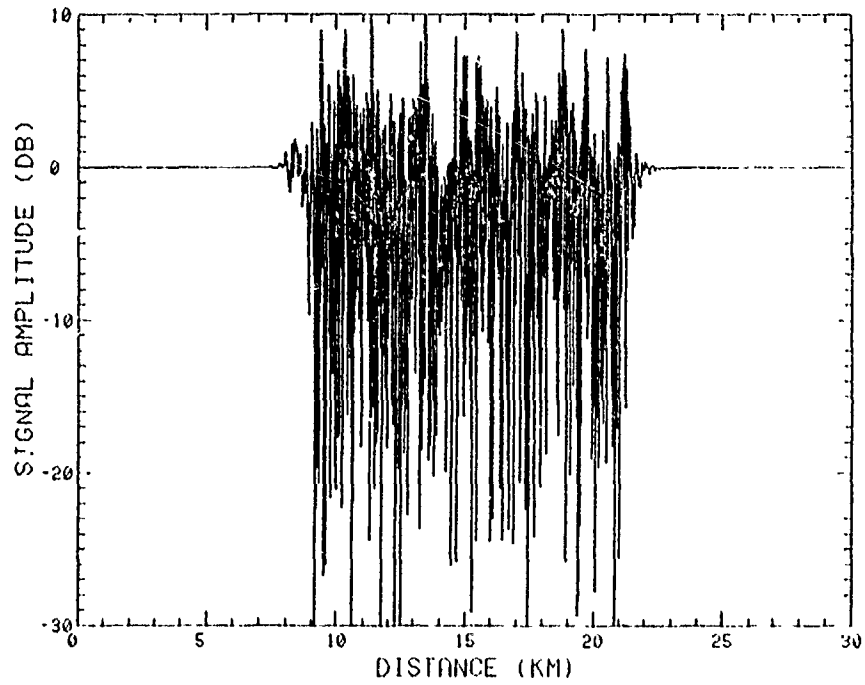


Figure 4-4. Signal amplitude and phase at a propagation distance of 10 km.

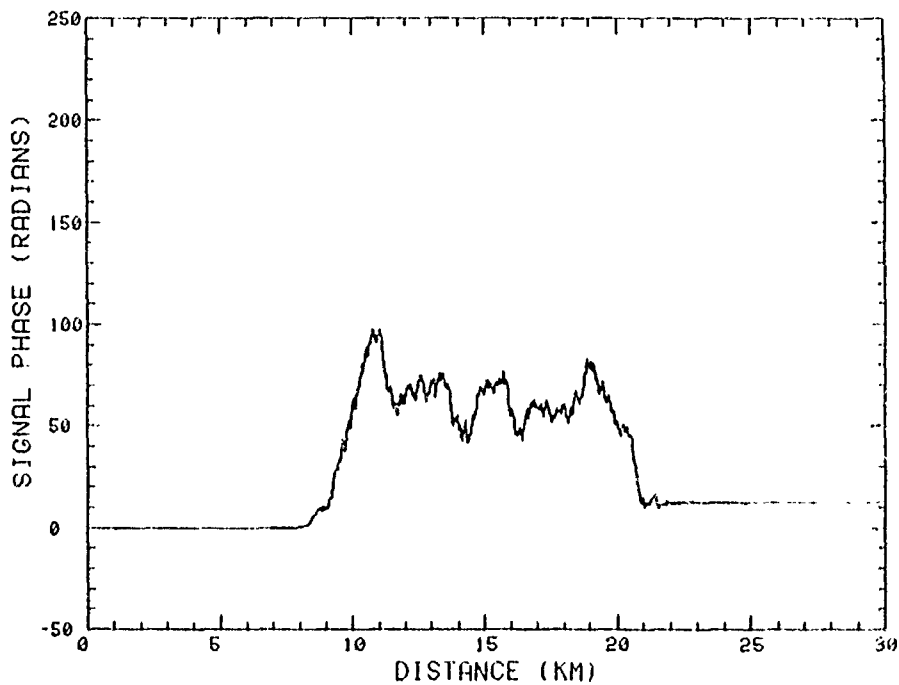
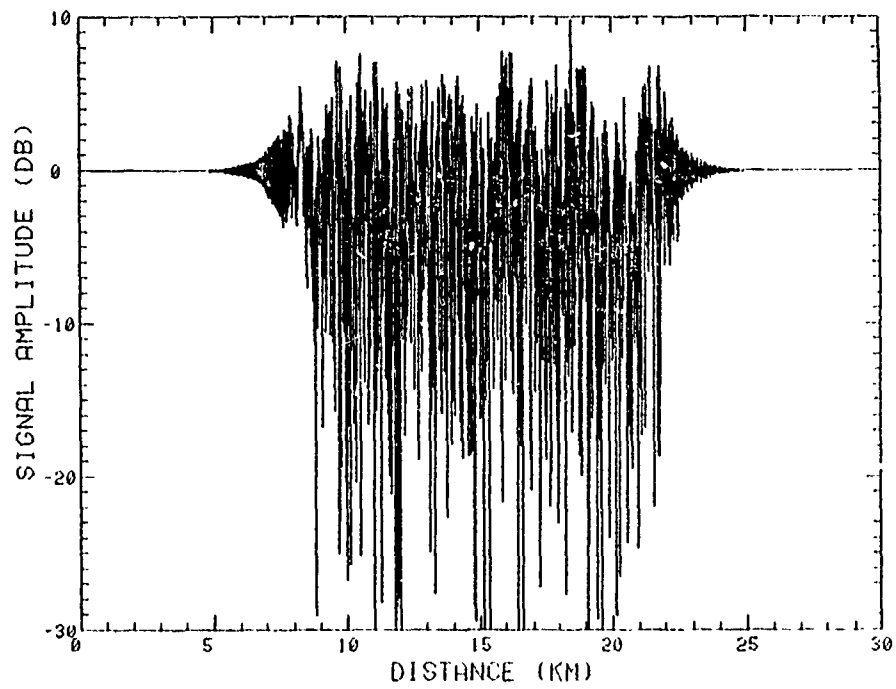


Figure 4-5. Signal amplitude and phase at a propagation distance of 30 km.

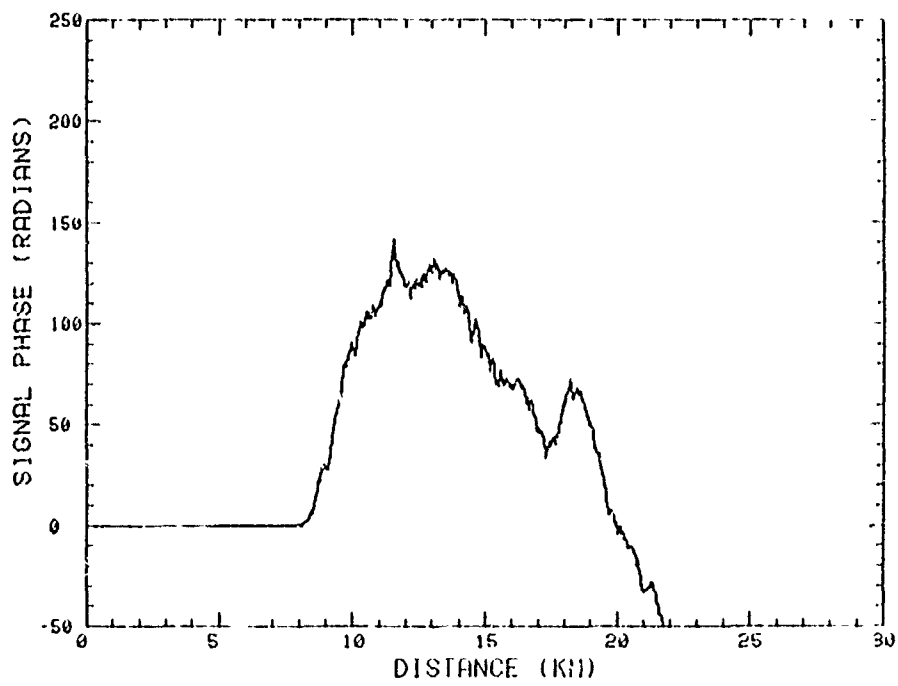
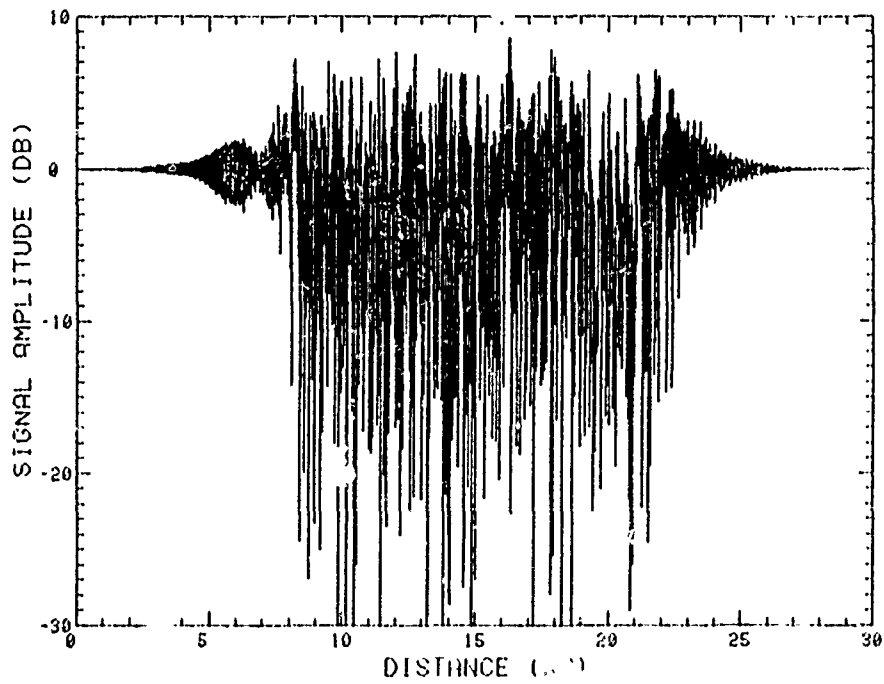


Figure 4-6. Signal amplitude and phase at a propagation distance of 50 km.

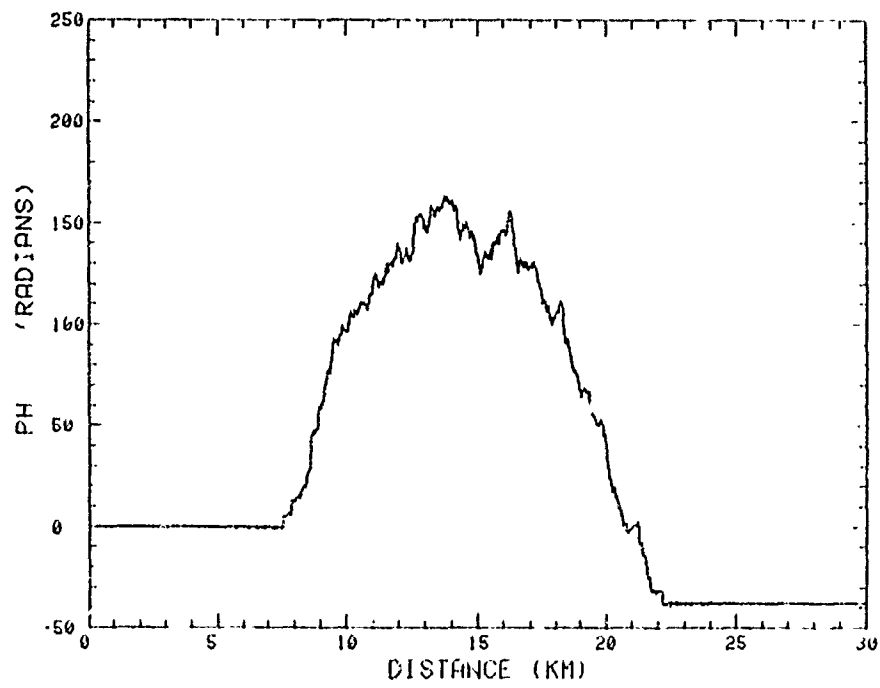
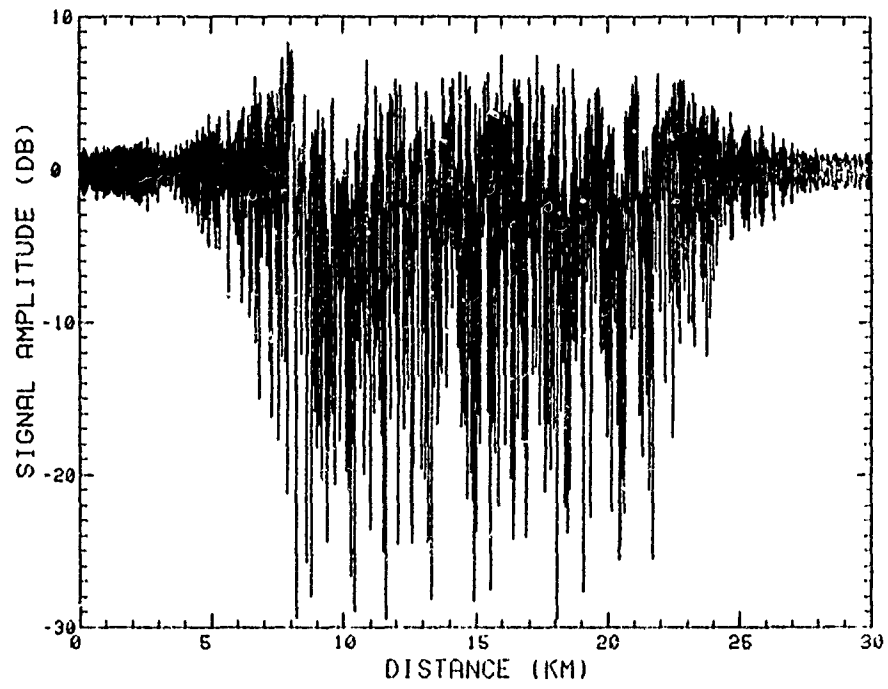


Figure 4-7. Signal amplitude and phase at a propagation distance of 100 km.

It is seen in Figures 4-2 to 4-7 that the signal phase starts at zero radians at an abscissa value of zero on the plots but does not return to zero at a distance of 30 km. This behavior is caused by rapid phase changes during deep fades which have faster variation than allowed for in the grid sampling. When the phase is reconstructed from the quadrature components in the simulation, there is a finite probability of missing  $2\pi$  changes in the phase and these  $2\pi$  shifts are reflected by deviations from zero radians at the end of the grid. Since these rapid phase changes occur during deep fades where there is relatively little signal power, they have no significant effect on any results presented here.

Figure 4-8 shows the signal amplitude and phase at a propagation distance of 100 km for a deterministic or mean barium cloud only. As can be seen, the deterministic model of Esther (a gaussian with no striations) causes only a slight defocusing even at a frequency of 150 MHz.

Figures 4-9 to 4-14 show the received signal amplitude at a propagation distance of 100 km. These six figures utilize the full barium cloud models of Esther and Fern as tabulated in Table 4-1. That is, both mean cloud and striations are used to obtain these results. For these figures no explicit inner scale was used in the MPS phase PSD, so that the effective inner scale size was 0.58 m as determined from the grid point spacing (a 30 km grid with 16384 points). A comparison of Figure 4-7 (inner scale of 10 m) and Figure 4-9 (inner scale of 0.58 m) shows that the effect of decreasing the inner scale size is to increase the amount of angular scattering.

Figures 4-9 to 4-11 show the received signal amplitude for Esther at frequencies of 150, 200 and 250 MHz. The next three figures show received signal amplitude for Fern for the same three frequencies. It is apparent from the figures that Esther poses a more severe propagation environment than does Fern. Of course the figures simply reflect the barium cloud modeling parameters listed in Table 4-1 where  $\sigma_\phi$  for Esther is almost twice as

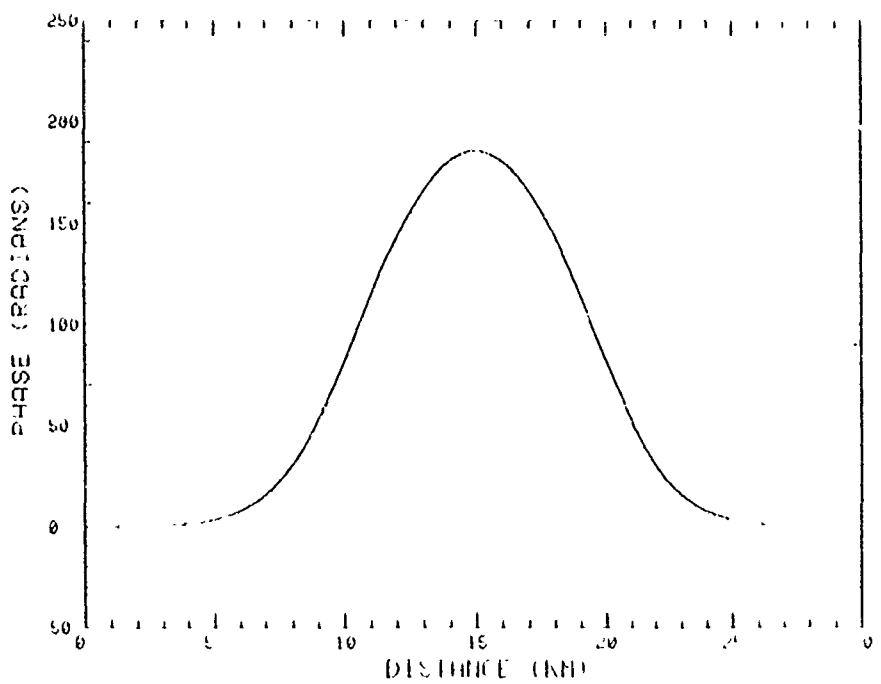
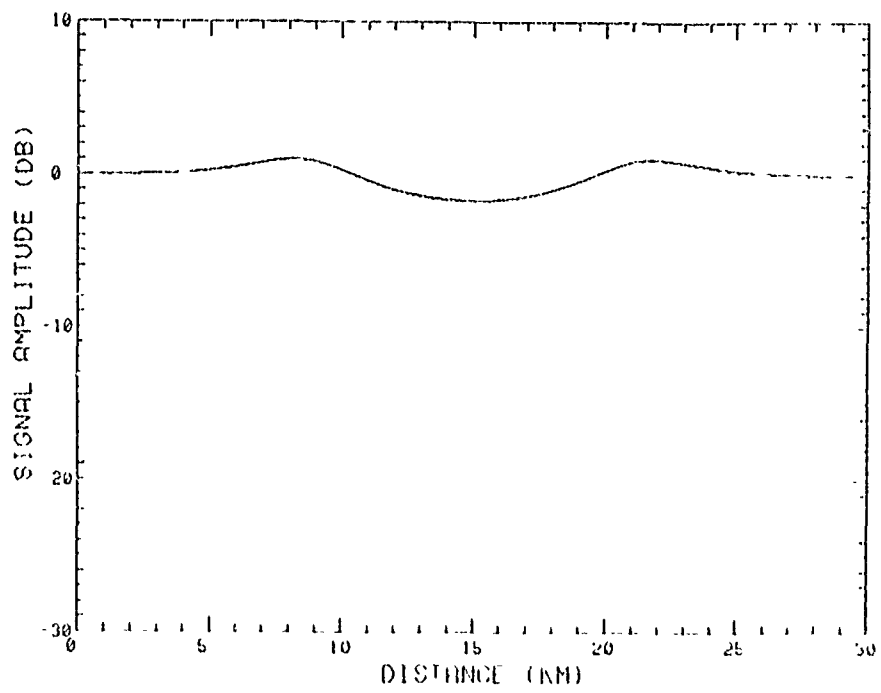


Figure 4-8. Signal amplitude and phase due to deterministic Esther barium cloud at 150 MHz.

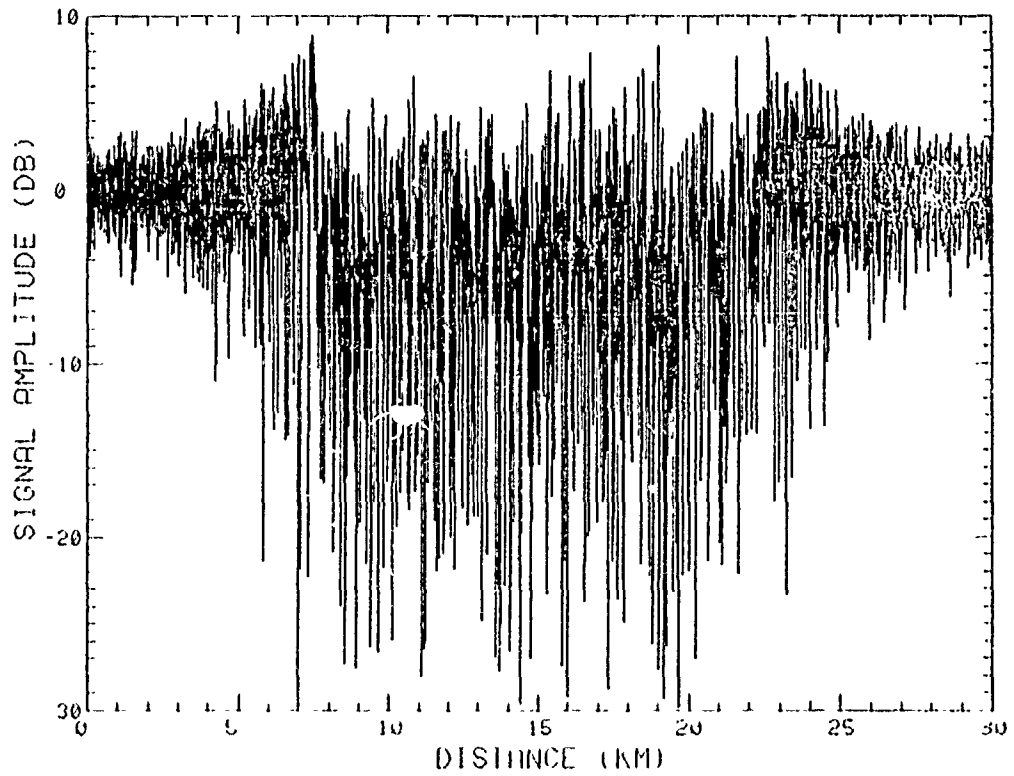


Figure 4-9. Signal amplitude for complete model of Esther at a frequency of 150 MHz.

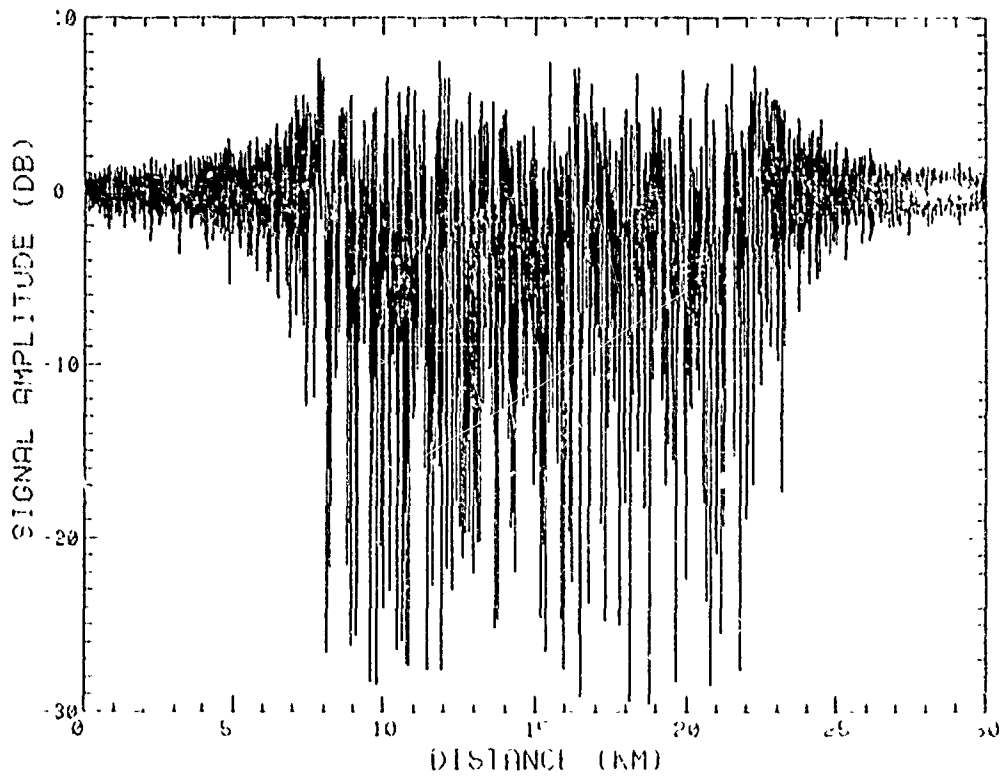


Figure 4-10. Signal amplitude for complete model of Esther at a frequency of 200 MHz.

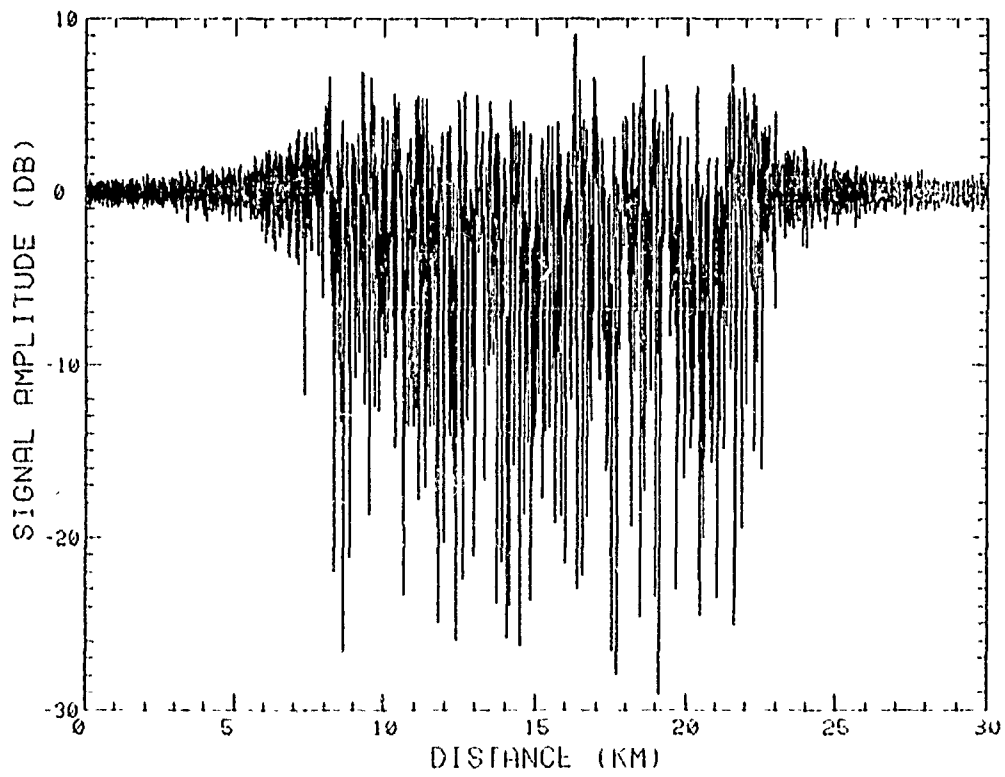


Figure 4-11. Signal amplitude for complete model of Esther at a frequency of 250 MHz.

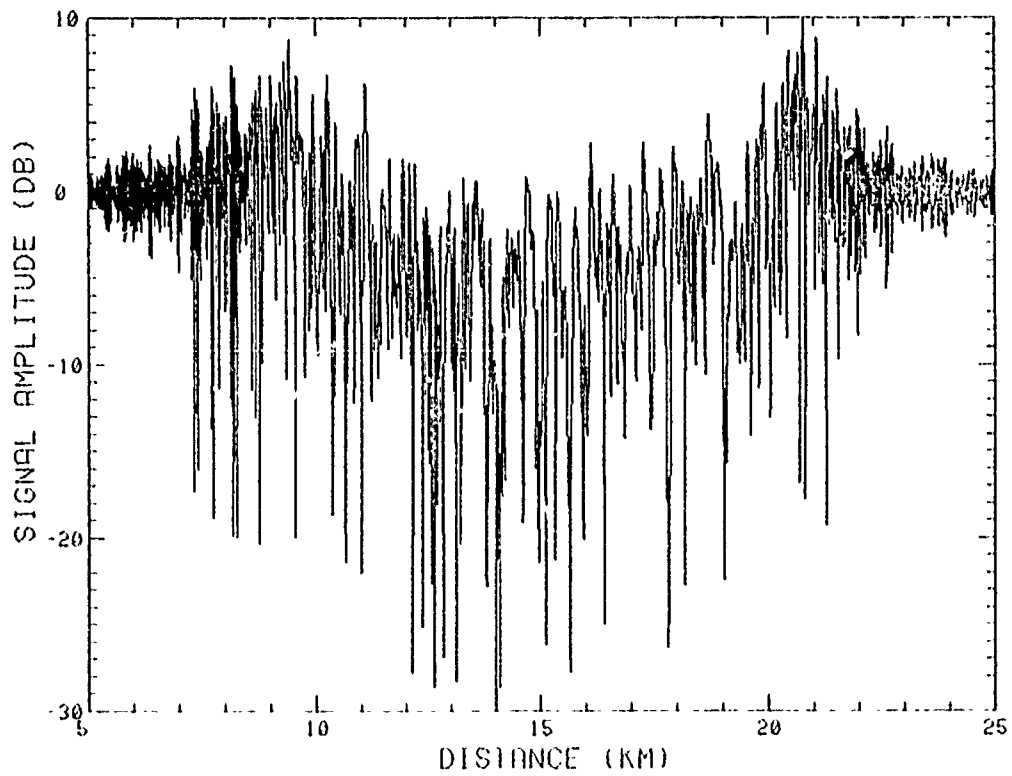


Figure 4-12. Signal amplitude for complete model of Fern at a frequency of 150 MHz.

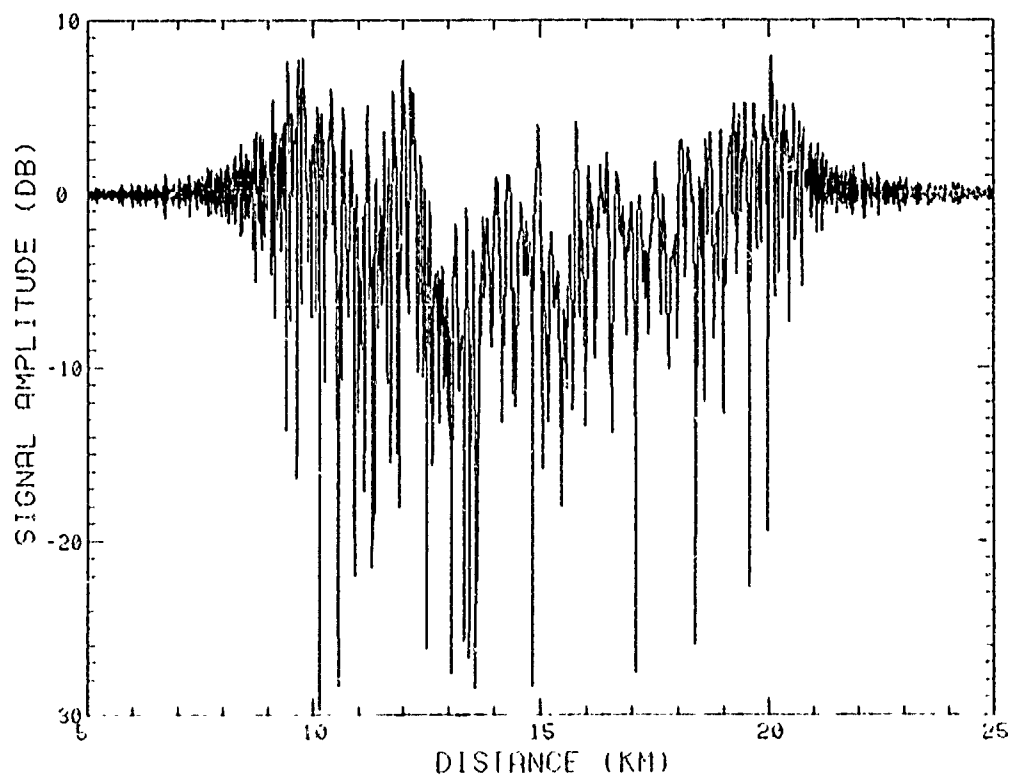


Figure 4-13. Signal amplitude for complete model of Fern at a frequency of 200 MHz.

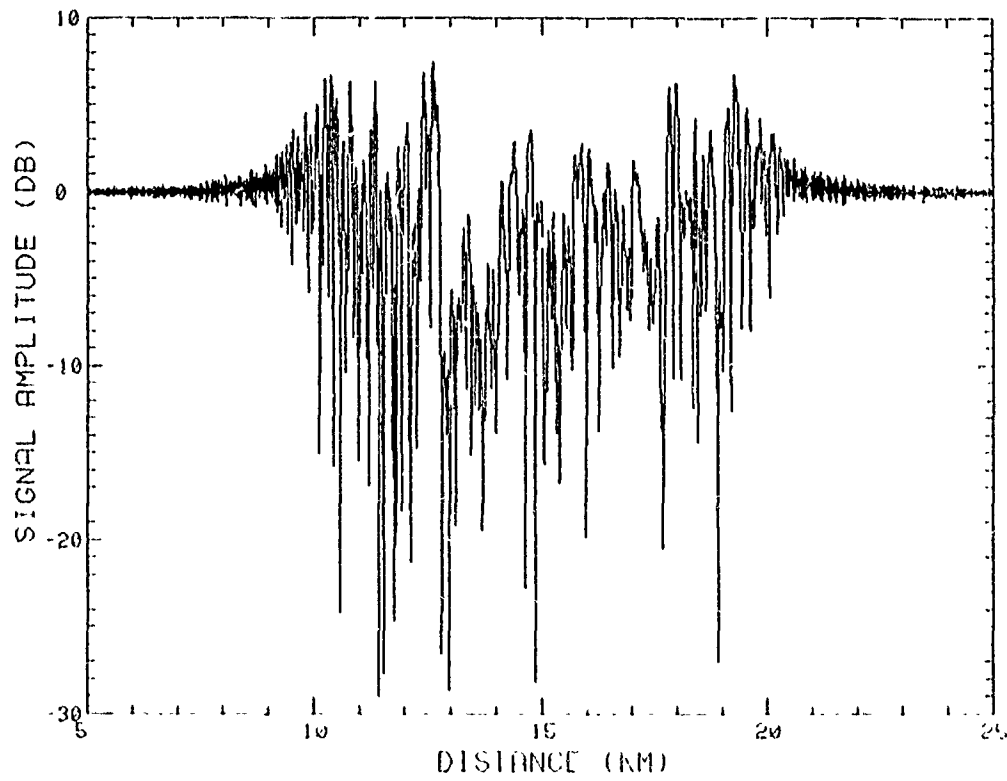


Figure 4-14. Signal amplitude for complete model of Fern at a frequency of 250 MHz.

large as  $\sigma_\phi$  for Fern. From the figures, it is evident that the large gaussian shape used to model the deterministic portions of the barium cloud causes a large defocusing region below the center of the cloud. This defocusing is stronger for Fern than for Esther because the Fern cloud is narrower with a larger mean phase variation. That is, from Table 4-1,  $r_0$  is smaller and  $\phi_0$  is larger for Fern than for Esther.

Work is currently in progress to relate the propagation results described above to analytical formulations for mean time delay, time delay jitter, and signal temporal broadening. These results will be presented in a subsequent report.

#### 4.2.2 Frequency-Selective Propagation Results

In this subsection, some examples of the PN code correlation function development with time are presented. The effect of inner scale variation is shown pictorially as well as the effect of changing the carrier frequency from 150 to 200 MHz.

As illustrated in Section 3 of this report, the PN code correlation function provides a measure of the impact of frequency-selective fading on the operation of the X-set code tracking loop. In the absence of frequency-selective effects, the envelope of the PN code correlator output is triangular in shape and the code loop has little difficulty tracking the peak, provided sufficient signal power is available.

Figure 4-15 shows a three-dimensional plot of the envelope of the PN code correlator output for Esther at 48 minutes after release at a carrier frequency of 150 MHz. The PN code chip rate (10.23 Mbps) is much larger than the fading rate here so that propagation conditions remain unchanged during the many chip durations associated with the calculation of any one of the PN code correlator output traces shown. Subsequent calculations of the correlator

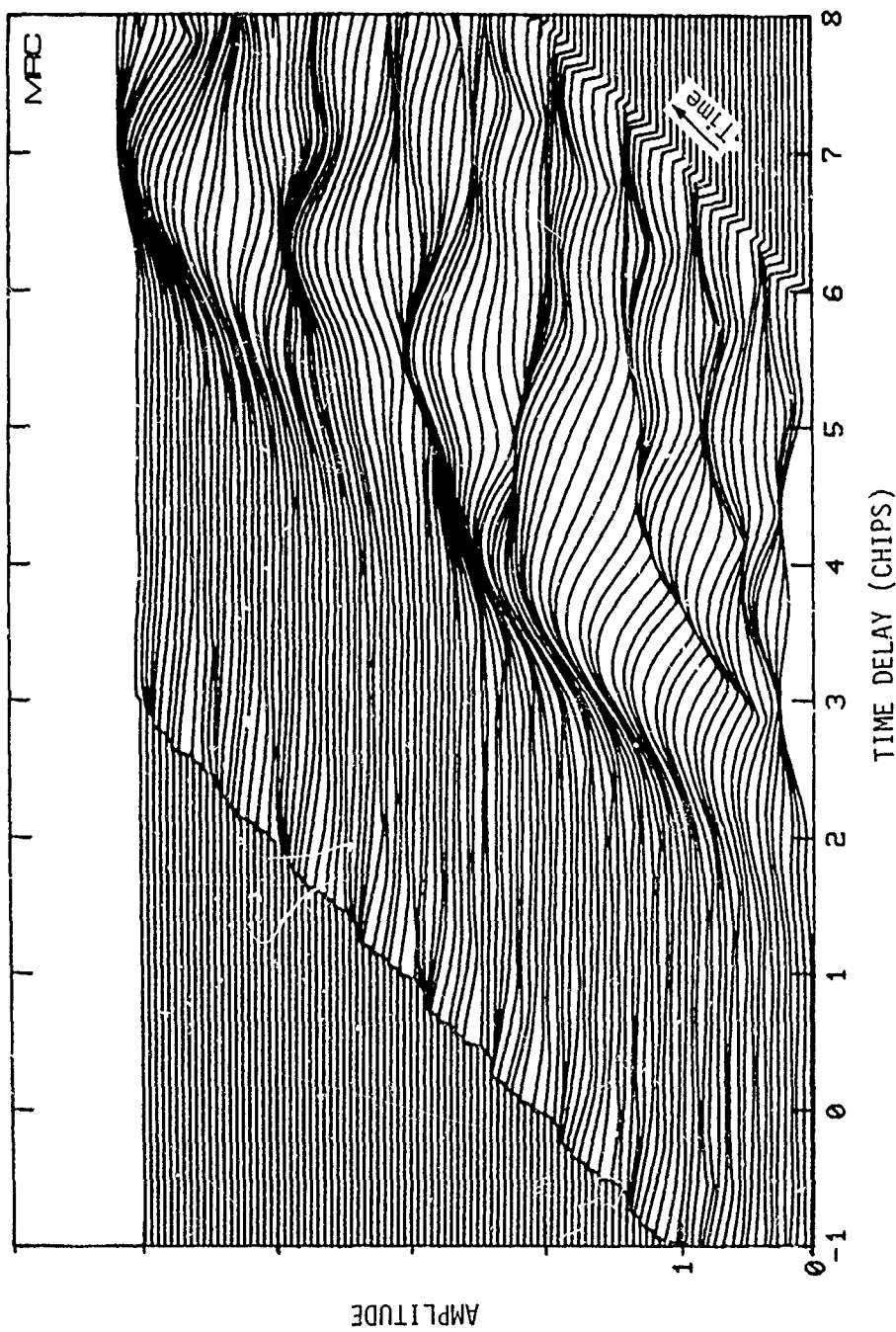


Figure 4-15. PN code correlator output envelope for Esther at a carrier frequency of 150 MHz (inner scale of 0.58 m).

output, corresponding to successive points in the MPS grid, are shown plotted behind previous calculations in the figure. Figure 4-15 shows the received PN code correlation envelope as a function of time delay in code chips (1 chip duration is 97.75 nsec). The plot shows 101 successive correlator output traces corresponding to 101 successive points in the MPS grid separated by 1.831 m. At an aircraft velocity of 250 m/sec these 101 points would correspond to a time interval of about 0.7 seconds. The time domain signal was reconstructed from 16 frequencies propagated over a bandwidth of 20.46 MHz so that  $\Delta f$  is 1.27875 MHz. The unambiguous period of the reconstructed output waveforms is then  $1/\Delta f = 7.82 \times 10^{-7}$  sec (8 chips). The complete barium cloud model listed in Table 4-1 for Esther at 48 minutes was used to obtain the results shown in Figure 4-15. The effective inner scale here is 0.58 m. The 101 successive points shown in the figure are located almost directly beneath the center of the barium cloud, i.e., near the 15 km distance in Figure 4-9. (Figure 4-9 shows one of the 16 frequencies used in the DFT algorithm to reconstruct the time domain signal.) The mean total electron content (TEC) through the center of this cloud causes a time delay of about 2 chips at 150 MHz. The delay due to mean TEC is further increased by frequency-selective scattering as shown in Figure 4-15.

Figure 4-16 shows the same portion of the PN code correlator output envelope as the previous figure, except the inner scale is changed to 10 m. Again the effect of the larger inner scale size is to decrease the amount of angular scattering and consequently produce smoother time domain waveforms. As discussed in Section 3, the frequency-selective propagation environment acts to distort, lengthen and delay the signal as shown in the figure.

In both Figures 4-15 and 4-16 the abscissa scales include the additional signal delay due to propagation through the mean barium cloud as noted above. The selection of the unambiguous plotting interval (DFT window) for these two figures is somewhat erroneous. The signal energy

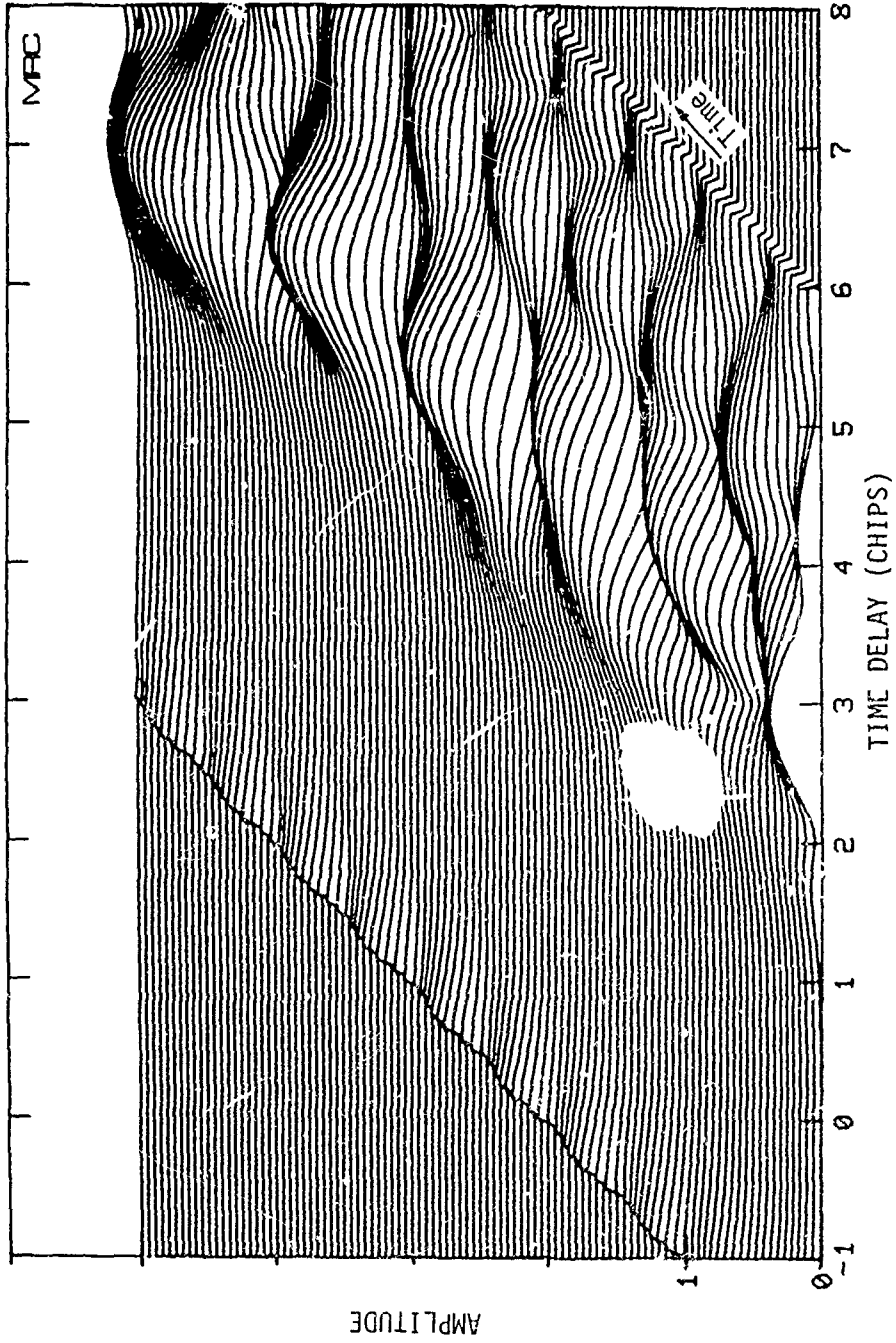


Figure 4-16. PN code correlator output envelope for Esther at a carrier frequency of 150 MHz (inner scale of 10 m).

appearing at the left hand side of each plot should have been plotted at the right hand side so that all energy is delayed relative to the onset of the PN code correlator output.

Figures 4-17 and 4-18 show a comparison of the PN code correlator outputs for carrier frequencies of 150 and 200 MHz for Esther at 48 minutes after release. In both of these cases the propagation simulation included only the effects of the striations, with no deterministic barium cloud. Thus the abscissa scales shown in these two figures do not include the mean TEC delay. A value of 10 m was used for the inner scale. Again the 101 MPS points shown correspond to the same locations approximately beneath the center of the barium cloud striations. (See Figure 4-1 for the phase screen representation of the barium cloud striations at 150 MHz.) For the two figures, 32 frequencies were used over a bandwidth of 20.46 MHz with a smaller  $\Delta f$  and a larger unambiguous time interval of 16 chips. This finite bandwidth, which corresponds to the first null-to-first null width of the PN signal spectrum, causes a slight rounding in the triangular shape of the autocorrelation function and a power reduction of 0.89 dB at the peak. A very small amount of additional spreading is introduced by mean dispersive effect due to an assumed total electron content of  $5 \times 10^{16}$  electrons/m<sup>2</sup>. Both effects are included in the two figures, although the mean TEC time delay is not included.

The effect of increasing the carrier frequency and thus reducing the angular scattering is evident from the figures. At 150 MHz energy is delayed up to about 5 chips as shown in Figure 4-17; at a carrier frequency of 200 MHz very little energy is delayed more than 3 to 4 chips.

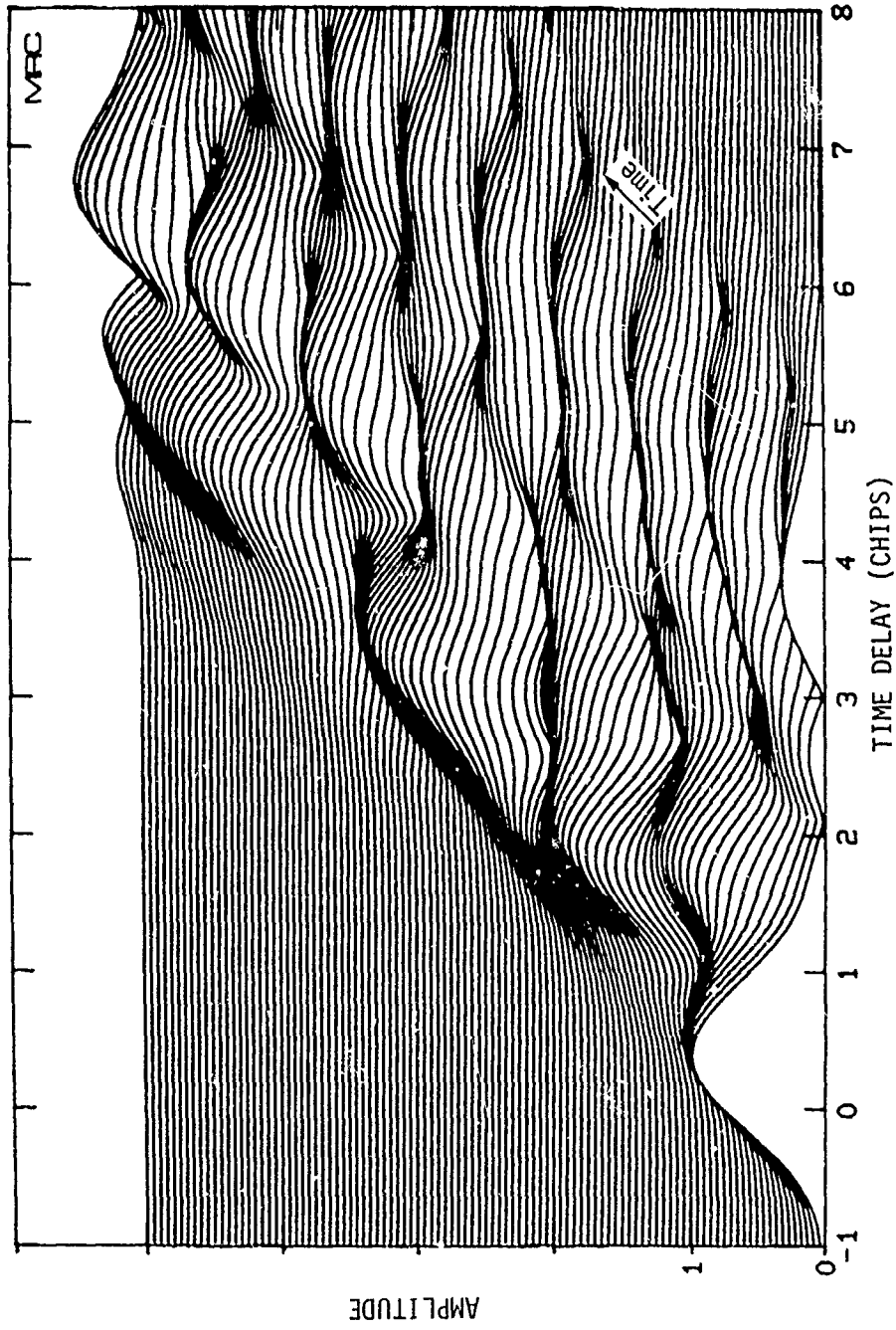


Figure 4-17. PN code correlator output envelope for Esther at a carrier frequency of 150 MHz.

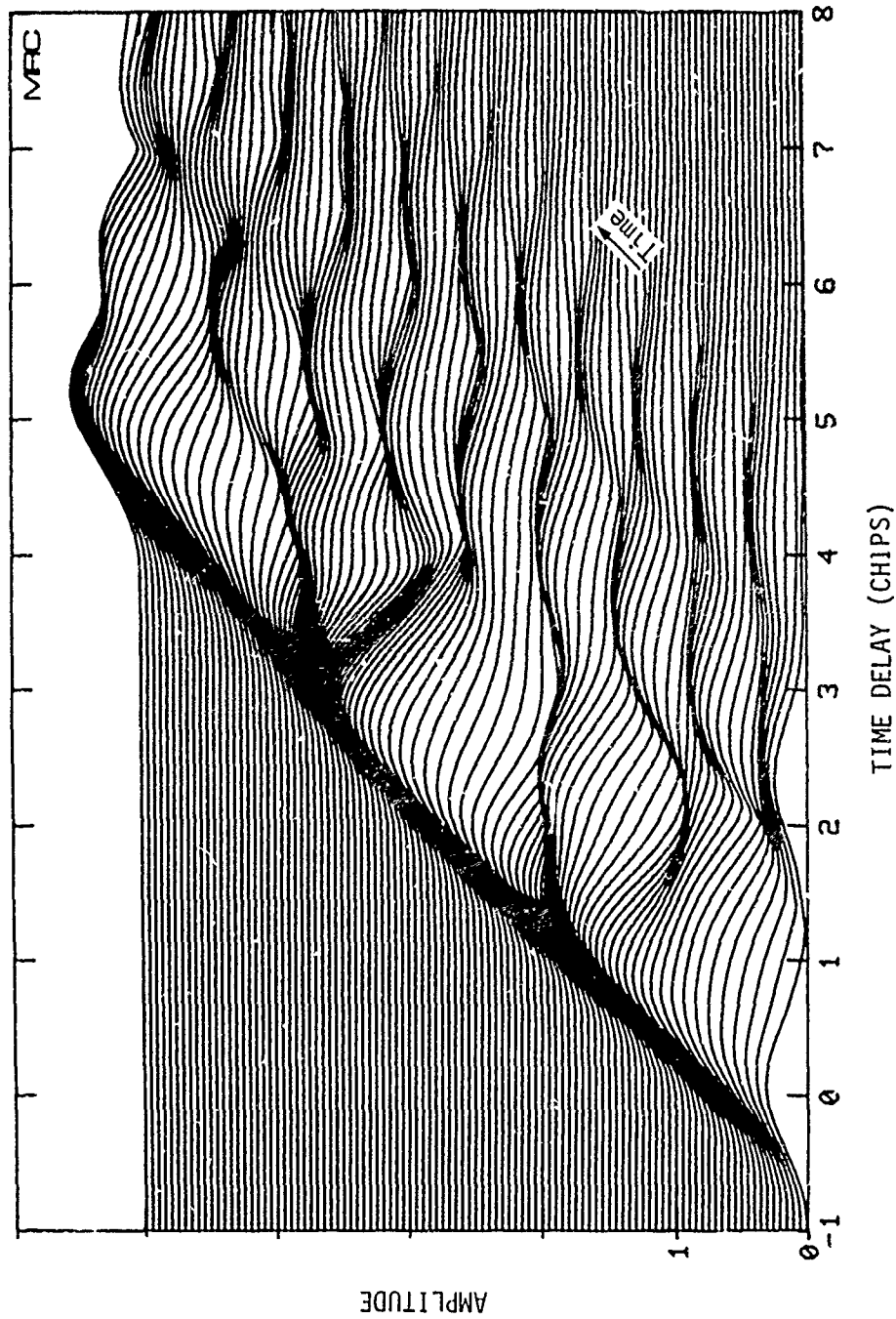


Figure 4-18. PN code correlator output envelope for Esther at a carrier frequency of 200 MHz.

#### 4.3 X-SET PERFORMANCE RESULTS

Results presented in Reference 4-3 illustrate the performance of the X-set receiver under both normal and disturbed nonselective signal conditions. In this section the X-set simulation, modified as described in Section 3 to include frequency-selective effects, is exercised with MPS calculations of signal structures to investigate receiver performance under disturbed, frequency-selective propagation conditions. A variety of X-set simulations have been performed for both Esther and Fern at frequencies from 150 to 250 MHz. The examples shown here are confined to the 32 frequency MPS calculations of Esther at 150 and 200 MHz, portions of which are shown in Figures 4-17 and 4-18. No deterministic barium cloud is present in these examples, the inner scale is 10 m and the striations occupy only the center portion of the MPS grid (as shown in Figure 4-1).

Of the entire 30 km long MPS grid, only a small portion (3.75 km) was available for utilization in the X-set receiver simulation. This 3.75 km length extended from 11.25 km to 15 km on the abscissa scale shown in Figure 4-1 and consequently included the region near the center of the striated cloud where angular scattering effects are most severe. For use in the receiver simulation, a velocity of 250 m/sec is assumed and the 3.75 km stretch of data is converted to a 15 second time period. This period is too short to accumulate statistics on receiver performance. However, the variety of short simulation runs that have been performed do provide valuable insight into the manner in which frequency-selective propagation disturbances impact X-set receiver operation.

##### 4.3.1 Receiver Design Parameters

Except where otherwise noted, results presented in this section are obtained using receiver design parameter values listed in Table 4-2. These parameters are discussed in Reference 4-3 and many results are presented there using this baseline set of design values.

As shown in Table 4-2, the third-order Costas loop bandwidth is 21.3 Hz, the second-order AFC loop bandwidth is 3.3 Hz and the first-order code loop bandwidth is 0.1 Hz. Doppler (velocity) aiding from the carrier tracking loop is applied to the code tracking loop. These and the other design values listed in the table are all inputs to our X-set simulation program.

With one important exception, the values shown in Table 4-2 are obtained primarily from GPS Phase I specification documents (References 4-4, 4-5, 4-6) and from the Draper Laboratory report by Stonestreet (Reference 4-7). The major exception is that we have gone back to the 250/sec AFC/Costas loop iteration rate used by Cahn (Reference 4-8) for the baseline design, instead of the 50/sec rate stated in Reference 4-7. This is done for two reasons: (1) at the larger Costas loop bandwidths of interest, the 250/sec loop iteration rate provides better X-set performance, and (2) discussions with GPS JPO personnel indicate that this iteration rate may be reinstated in Phase II or Phase III (Reference 4-9).

Table 4-2. Nominal design values used in X-set simulation.

AFC/COSTAS/PN GPS X-SET RECEIVER OPERATION IN SIMULATED BARIUM CLOUD ENVIRONMENT			
RECEIVER DESIGN PARAMETERS			
CARRIER FREQUENCY (HZ)	2.50000E+08	AGC UPDATE RATE (HZ)	2.50000E+02
PN CODE CHIP RATE (BPS)	1.02300E+07	AGC TIME CONSTANT (SEC)	1.00000E+00
NAV DATA BIT RATE (BPS)	5.00000E+01	AGC RESOLUTION (DB)	1.00000E+00
A/D SAMPLING RATE (HZ)	2.50000E+02	AGC DESIGN C/N0 (DB-HZ)	3.50000E+01
PARITY ENCODING OPTION	2	AGC MEASUREMENT MODE	AUTO
A/D QUANTIZATION (BITS)	8	CODE UPDATE TIME (SEC)	2.40000E-01
A/D SCALE FACTOR (BITS)	5	CODE LOOP ORDER	1
VCO RESOLUTION (RAD)	9.81748E-02	CODE BANDWIDTH (HZ)	1.00000E-01
VCO RESOLUTION (CHIP)	1.56250E-02	CODE DAMPING FACTOR	
BACKGROUND DELAY (SEC)	0.00000E-01	CODE LOOP LIMIT (CHIP)	2.50000E-01
COSTAS/AFC TRACK MODE	YES	CODE LOOP DOPPLER AIDED	YES
COSTAS UPDATE RATE (HZ)	2.50000E+02	AFC UPDATE RATE (HZ)	2.50000E+02
COSTAS LOOP ORDER	3	AFC LOOP ORDER	2
COSTAS BANDWIDTH (HZ)	2.13333E+01	AFC BANDWIDTH (HZ)	3.30000E+00
COSTAS DAMPING FACTOR		AFC DAMPING FACTOR	7.07107E-01
COSTAS LOCK TIME (SEC)	2.40000E-01	AFC LOCK TIME (SEC)	9.60000E-01
COSTAS LOCK THRESHOLD	2.50000E-01	AFC LOCK THRESHOLD	2.00000E-01
COSTAS/AFC ALGORITHM	MEAN	AFC SWITCH POSITION	AUTO OFF

The carrier loop iteration rate is one of the design excursions investigated in several disturbed propagation cases in this section. Of the various AFC/Costas loop filter implementations tested previously at 50/sec iteration rate with nominal 21.3 Hz Costas loop bandwidth, one implementation stood out as by far the best choice. This implementation employs the "mean-value" algorithm, which simply represents a specific method of choosing loop filter coefficients, in conjunction with lumping the foreground portion of the filter output and constraining the foreground delay to be in the 0 to 4 ms range. With this specific implementation of the Costas loop, fairly good X-set performance is obtained at 50/sec loop iteration. There is still noticeable degradation of carrier and code tracking performance compared to that obtained with 250/sec carrier loop iteration, but the degradation is not nearly as serious as with other implementations tested. Reference 4-3 contains detailed information on this subject.

The values shown in Table 4-2 for the Costas and AFC lock detection filter integration times and threshold settings are somewhat speculative on our part. These parameters are discussed in Reference 4-3 and are based in part on information in References 4-7 and 4-8. The Costas lock detection filter is used to enable the AFC loop when Costas lock is lost and to disable the AFC when Costas lock is detected. This is the automatic AFC switching mode assumed here for the baseline design with 250/sec AFC/Costas loop iteration rate. The Costas lock detection filter state also determines the AGC measurement mode. The AGC operates coherently when Costas lock is detected and noncoherently when loss of Costas lock is sensed.

The AFC lock detection filter provides simulation output indicating loss or reacquisition of frequency lock, but has no internal effect on simulation operation here. In the actual X-set receiver, it is our understanding that indication of AFC out-of-lock might initiate a code reacquisition procedure. If this is the case, the AFC lock indicator is an important operational consideration. The AFC lock integration time shown in Table 4-2

actually corresponds to a 1.2 sec interval because one of every five A/D samples straddles a data bit edge and is not used in the AFC lock detection accumulation. The 1.2 sec integration period is based on results obtained in previous investigations where it was found that a shorter integration time caused the filter to indicate loss of lock during brief fades when AFC lock was actually maintained. The integration interval should not be too large because long, deep signal fades can indeed cause loss of AFC and code lock.

The AGC design value of  $C/N_0$  shown in Table 4-2 is used in the simulation to scale input signal amplitude and noise samples to the nominal design level. In effect, this parameter initializes the AGC gain adjustment in the simulation. To avoid possibly large AGC transients at the beginning of each simulation trial here, the AGC is initialized to the mean input signal level at the start of each case. Thereafter, the AGC loop operates in a normal manner.

A detailed description of the GPS navigation data formatting and error-detection encoding is contained in Reference 4-6. The data bit rate is 50 bps. A complete data message (called a frame) consists of 1500 bits, and is divided into five subframes. Each subframe consists of ten 30-bit words. Thus a word is transmitted in 0.6 sec, a subframe in 6 sec, and a complete data frame in 30 sec. Data transmission is continuous, and frames are therefore repeated at 30 sec intervals.

All data is encoded using a (32,26) Hamming code, which is a single error-correction, double error-detection code. The X-set receiver simulation incorporates the GPS data formatting and encoding described in Reference 4-6. The error-correction capability of the Hamming code is very limited and is not used. However, the error-detection capability is quite useful. Also, the (32,26) Hamming code provides resolution of the  $\pi$  phase ambiguity inherent in Costas phase tracking.

#### 4.3.2 X-Set Performance at 150 MHz

A few graphical examples of X-set receiver simulation results are presented to provide insight into the effects of signal scintillation on receiver operation.

Figure 4-19 shows the input signal amplitude and phase over a 15 second simulation time interval at a carrier frequency of 150 MHz. Signal amplitude is plotted in decibels relative to the mean signal level. The corresponding signal phase is plotted in radians. The time scale here results from a 250 m/sec conversion of the distance scale used in the numerical propagation algorithm. This signal realization is the sixteenth member of the thirty-two frequency comb used as receiver input to construct the received time domain signal at the PN code correlator output.

Figures 4-20 through 4-22 compare the resulting phase, frequency, and code tracking performance of the simulated X-set receiver for two different values of mean carrier power-to-noise density ratio ( $C/N_0$ ), 35 and 32 dB-Hz.

Figure 4-20 shows the phase tracking error time history for the two values of mean  $C/N_0$  for the 15 second simulation period. This phase tracking error is obtained in the simulation by differencing the incoming value of the signal phase with the estimated phase developed in the AFC/Costas loop and, as such, is not available to the receiver itself. Three adjacent equilibrium phase tracking states are shown on the plot at 0 and  $\pm\pi$  radians. The upper figure, with a mean  $C/N_0$  value of 35 dB-Hz exhibits much fewer phase slips, and only two brief periods of loss of phase-lock at about 7.5 seconds and at about 12 seconds. In both cases, this temporary loss of phase-lock is associated with simultaneous large receiver estimates of Doppler frequency shown in the top of Figure 4-21. The lower portion of Figure 4-20, at a mean  $C/N_0$  value of 32 dB-Hz is characterized by very

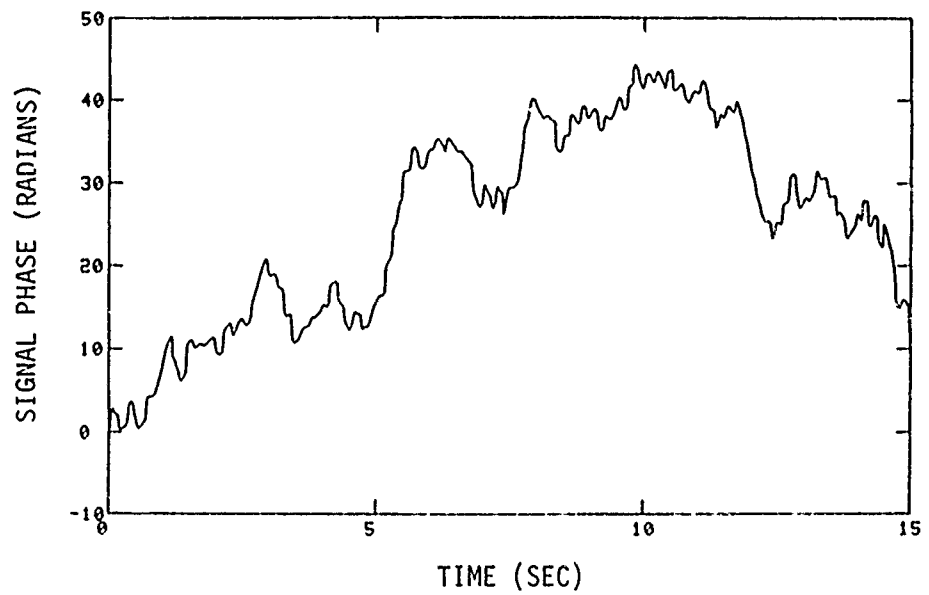
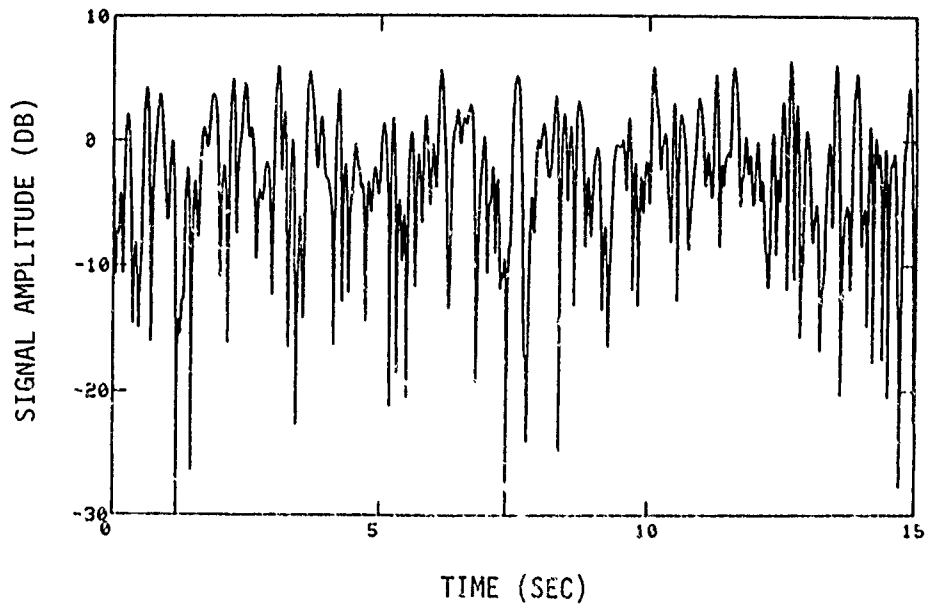


Figure 4-19. Received signal amplitude and phase for Esther at a carrier frequency of 150 MHz.

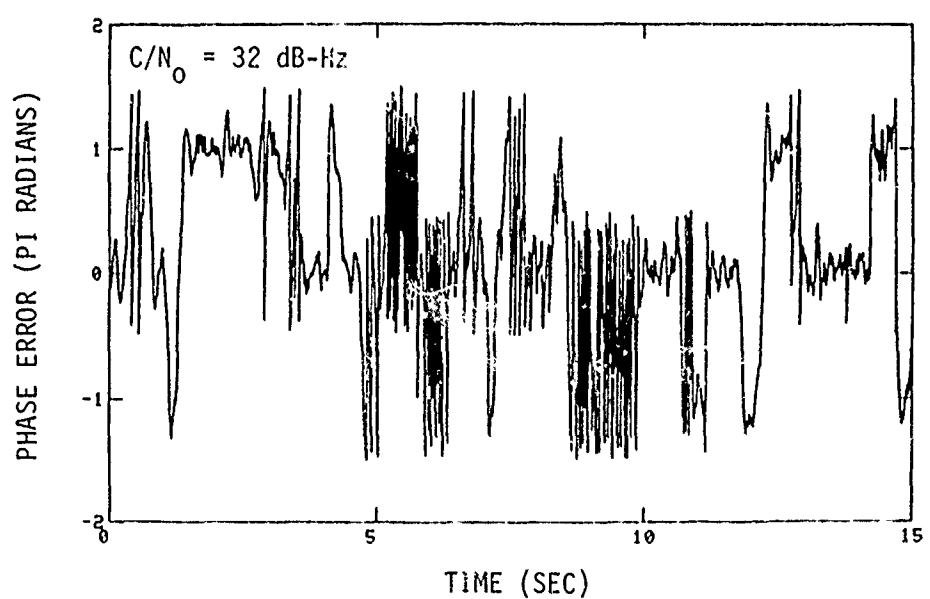
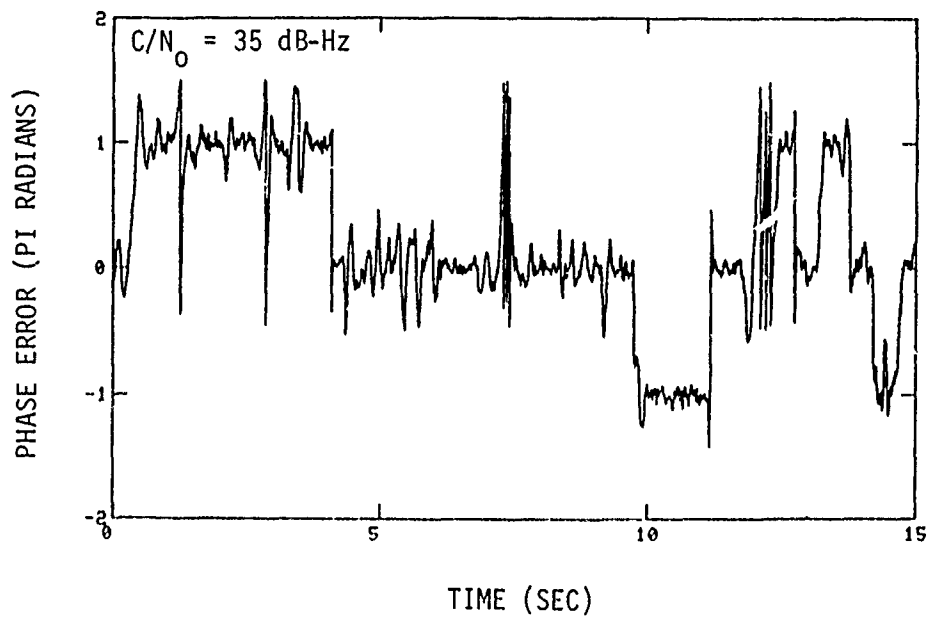


Figure 4-20. Esther at 150 MHz: phase tracking error time history.

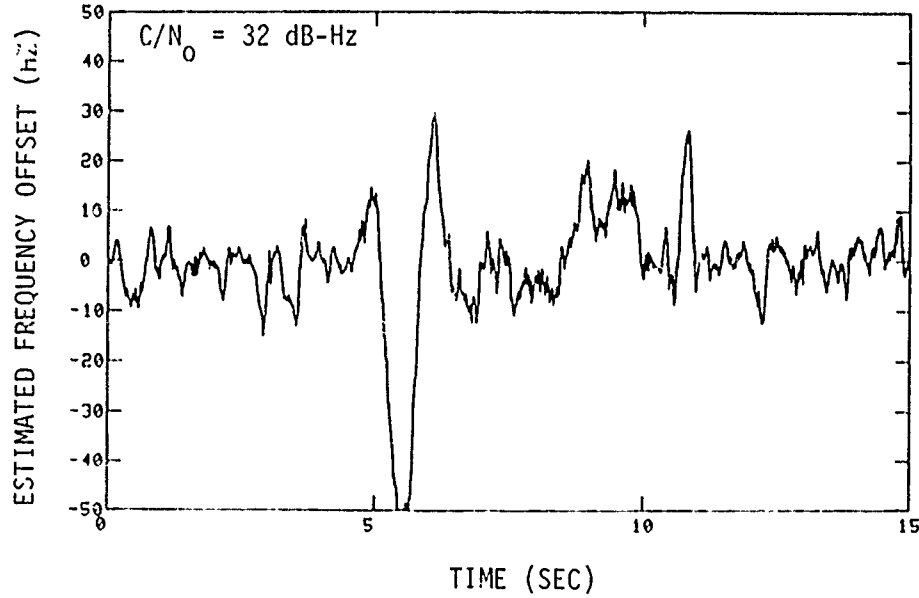
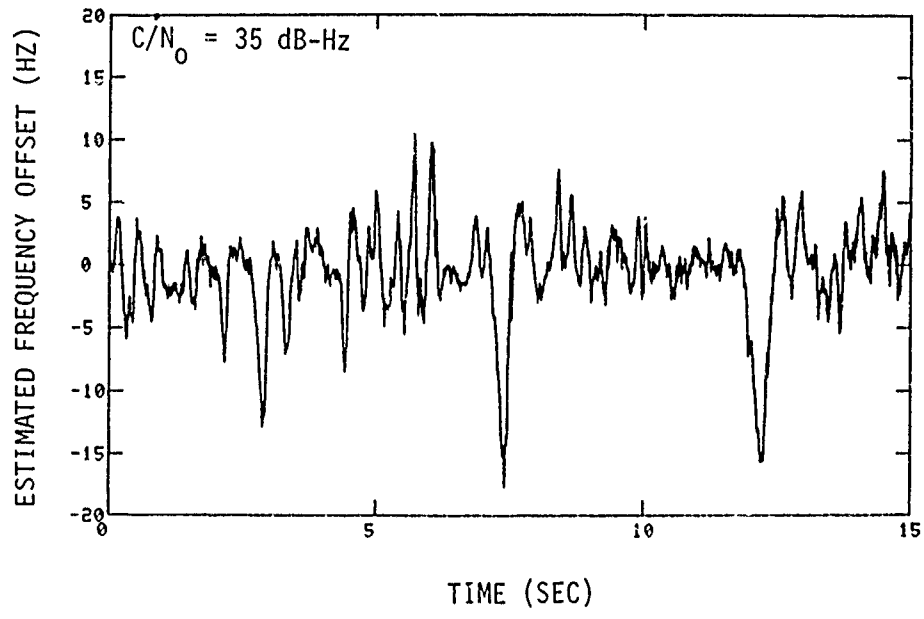


Figure 4-21. Esther at 150 MHz: AFC/Costas loop Doppler frequency estimate.

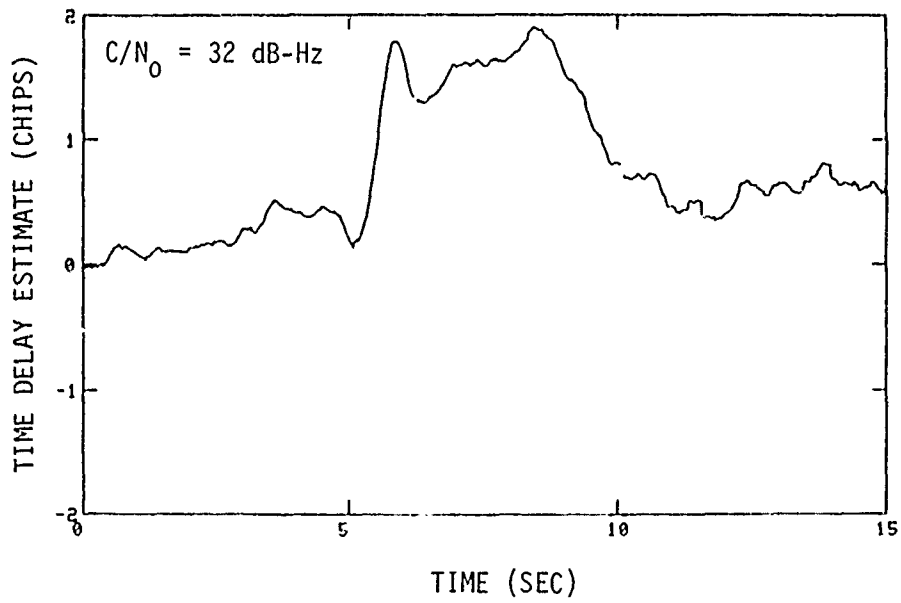
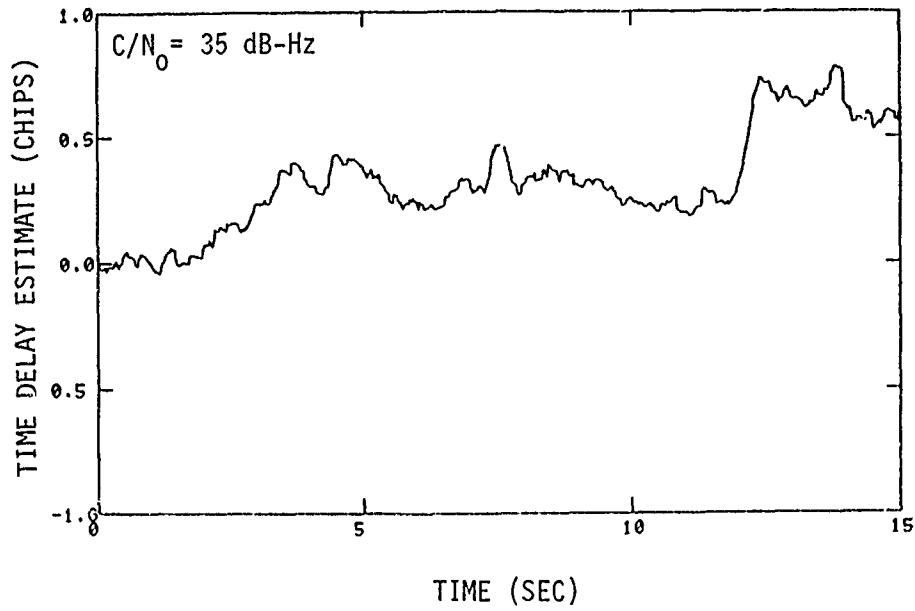


Figure 4-22. Esther at 150 MHz: PN code loop time delay estimate.

rough phase tracking and two extended periods of loss of phase-lock which are caused by a quite complicated interaction of the AFC/Costas loop and the code tracking loop discussed below. Overall, the phase tracking performance for this highly disturbed barium environment can be characterized as quite noisy with many phase slips. This poor phase tracking is reflected in poor data demodulation performance and hence large word error rates.

Figure 4-21 shows a comparison of the estimated Doppler frequency developed in the X-set AFC/Costas loop filter. The lower figure, for a mean  $C/N_0$  value of 32 dB-Hz exhibits much greater frequency deviations (note that the ordinates are different for the upper and lower plots) and rougher track. In particular, note the large, negative frequency deviation occurring between 5 and 6 seconds simulation time. This large excursion indicates that the AFC/Costas loop is out of phase lock (as shown in the previous figure) and also temporarily out of frequency lock. This in turn influences the code tracking loop, which is Doppler aided from the AFC/Costas loop.

Figure 4-22 shows a comparison of the code tracking performance of the X-set at the two values of mean  $C/N_0$ . Again note that the ordinate scales are different. As will be shown, the X-set at 35 dB-Hz  $C/N_0$  adequately tracks the peak of the PN code correlation envelope. At about 12 seconds in the upper plot and around 10 seconds in the lower plot there is a rapid change in the estimated code delay caused by Doppler aiding from the AFC/Costas loop. Note the corresponding large frequency excursions at these times in Figure 4-21. On the bottom plot of Figure 4-22, similar Doppler "aiding" to the code loop, at about 5 seconds simulation time, acts to drive the code delay estimate off the main correlation peak to an extended sidelobe. The code loop then tracks this sidelobe for about 5 seconds before reacquiring the main peak at about 10 seconds simulation time.

Figure 4-23 shows a comparison of the receiver code correlator amplitude for the two cases. The amplitude scale is decibels relative to the nominal correlator output level. (Under ideal conditions, and perfect code tracking, the code correlator amplitude takes on a value of 0 dB corresponding to the peak of the PN code autocorrelation function envelope.) Except for the period between 5 and 10 seconds, the two plots are almost identical. As discussed above, the differences are caused by tracking of a sidelobe by the code loop during this interval. During the sidelobe tracking period, less power appears at the correlator output and consequently the X-set performs as if the mean  $C/N_0$  were reduced.

Figures 4-24 through 4-26 show successive plots of the PN code correlator output envelope for three brief periods in the 15 second simulation. Each plot shows about 0.73 seconds of simulation time. Figure 4-24 shows the period between 6.60 sec and 7.33 sec. Figure 4-25 shows the period from 10.26 sec to 10.99 sec and Figure 4-26 shows the interval from 13.93 sec to 14.66 sec. Note the increasingly large distortion of the PN code correlation envelope as the simulation time increases to 15 seconds (Figure 4-26), at which point the observer is almost directly below the center of the barium cloud striations and thus subject to angular scattering arising from striations on either side of the cloud center. As the distance from the point below the cloud center increases (with decreasing simulation time) the angular scattering effects are less severe, as may be seen by comparing Figures 4-24 and 4-26.

Also shown in Figures 4-24 through 4-26 as a series of arrows is the X-set estimated time delay as it is tracked in the receiver delay-lock loop for the two values of  $C/N_0$  of 35 and 32 dB-Hz. These estimated time delays in the code loop are the same delay estimates plotted in Figure 4-22. In Figure 4-24, for the 35 dB-Hz  $C/N_0$  case the code loop can be seen to track the first major peak of the PN code envelope quite well at a time delay of

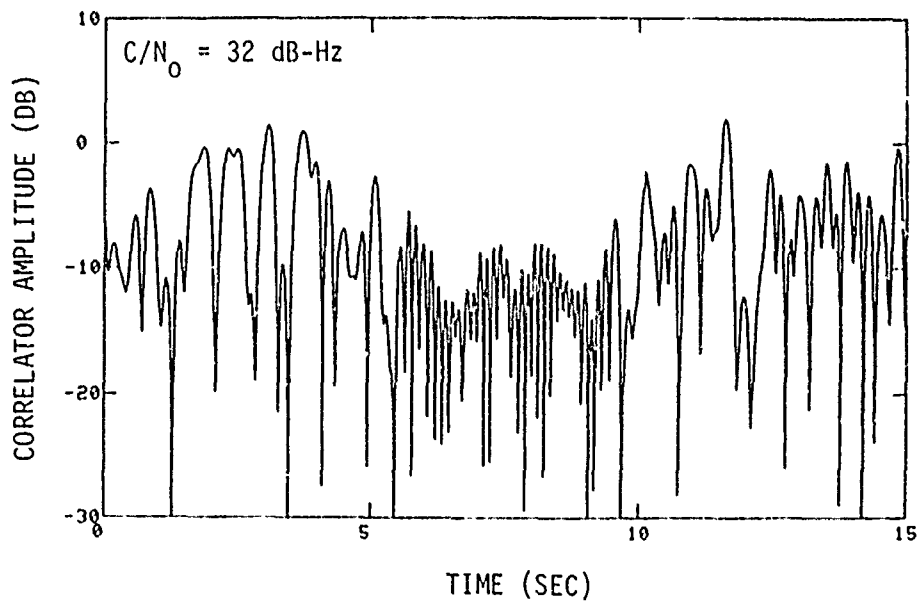
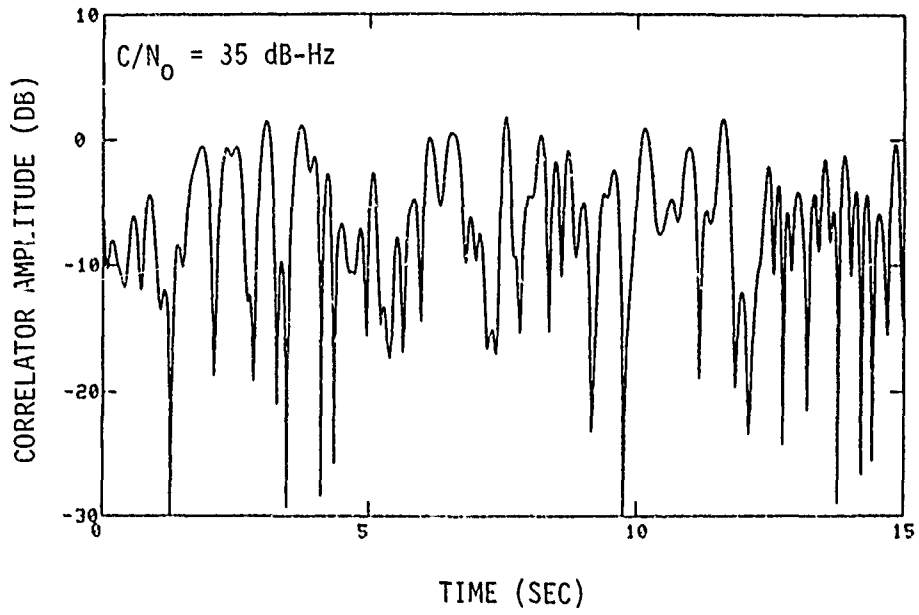


Figure 4-23. Esther at 150 MHz: X-set code correlator amplitude time history.

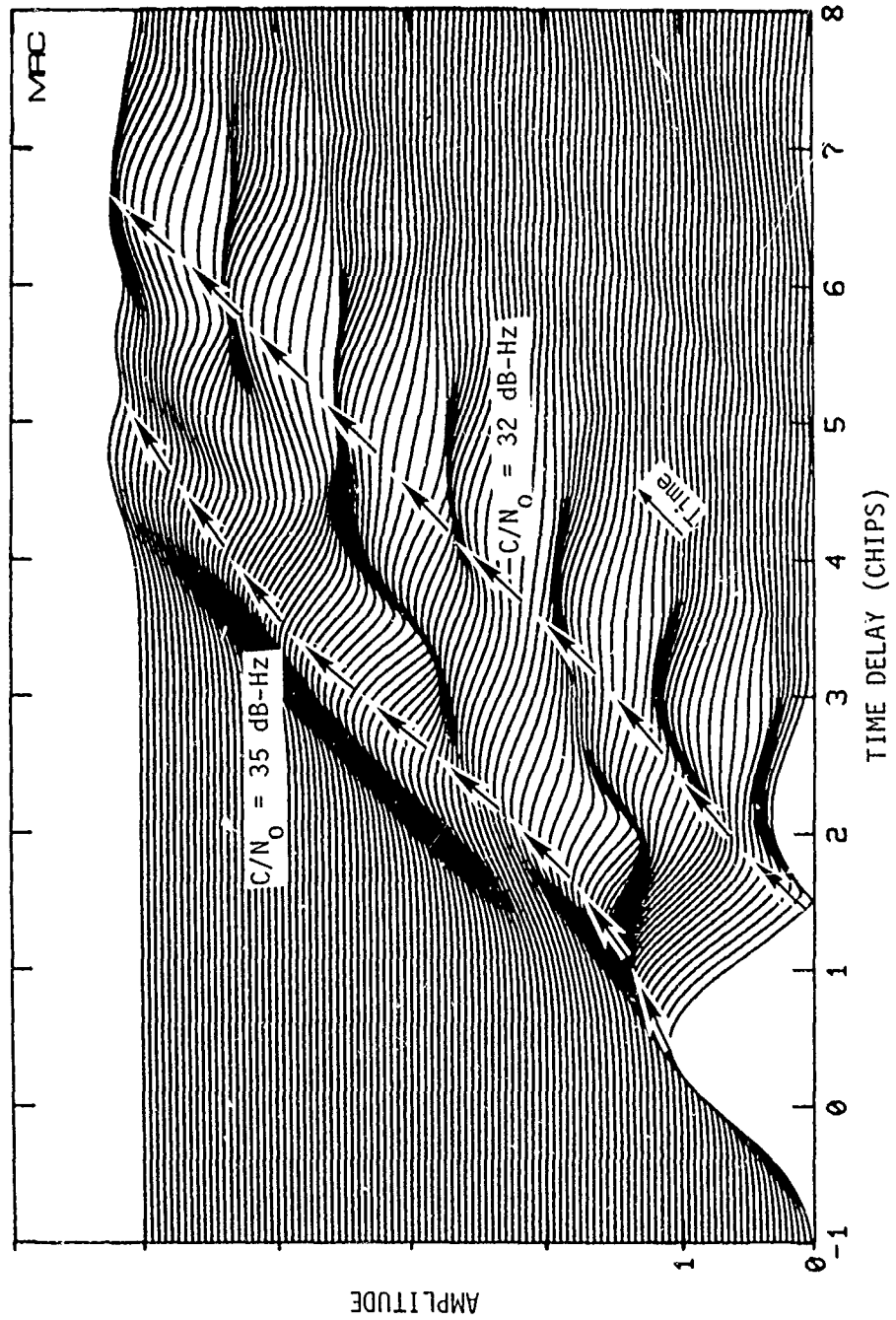


Figure 4-24. Esther at 150 MHz: PN code envelope and code tracking history for simulation time from 6.60 to 7.33 seconds.

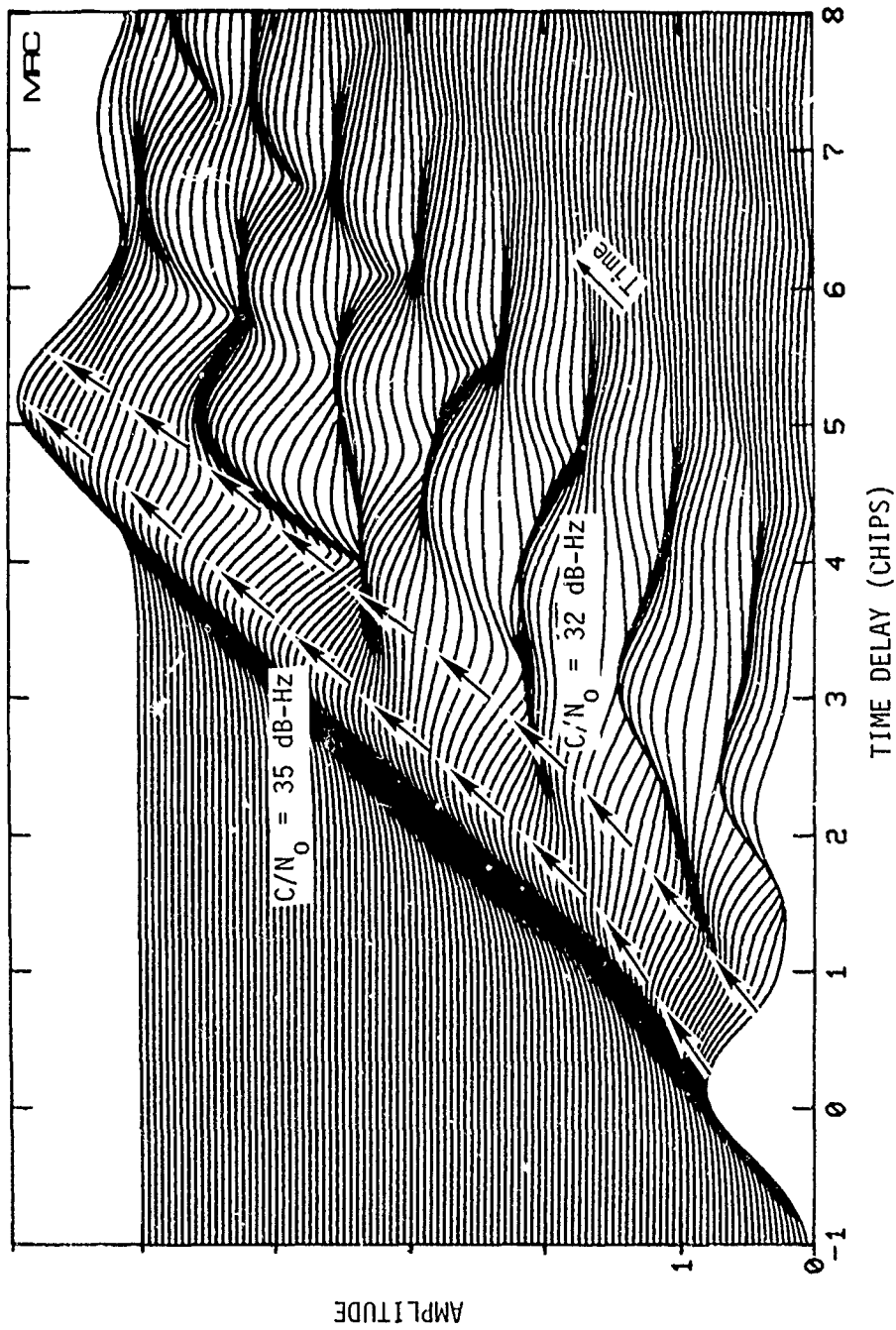


Figure 4-25. Esther at 150 MHz: PN code envelope and code tracking history for simulation time from 10.26 to 10.99 seconds.

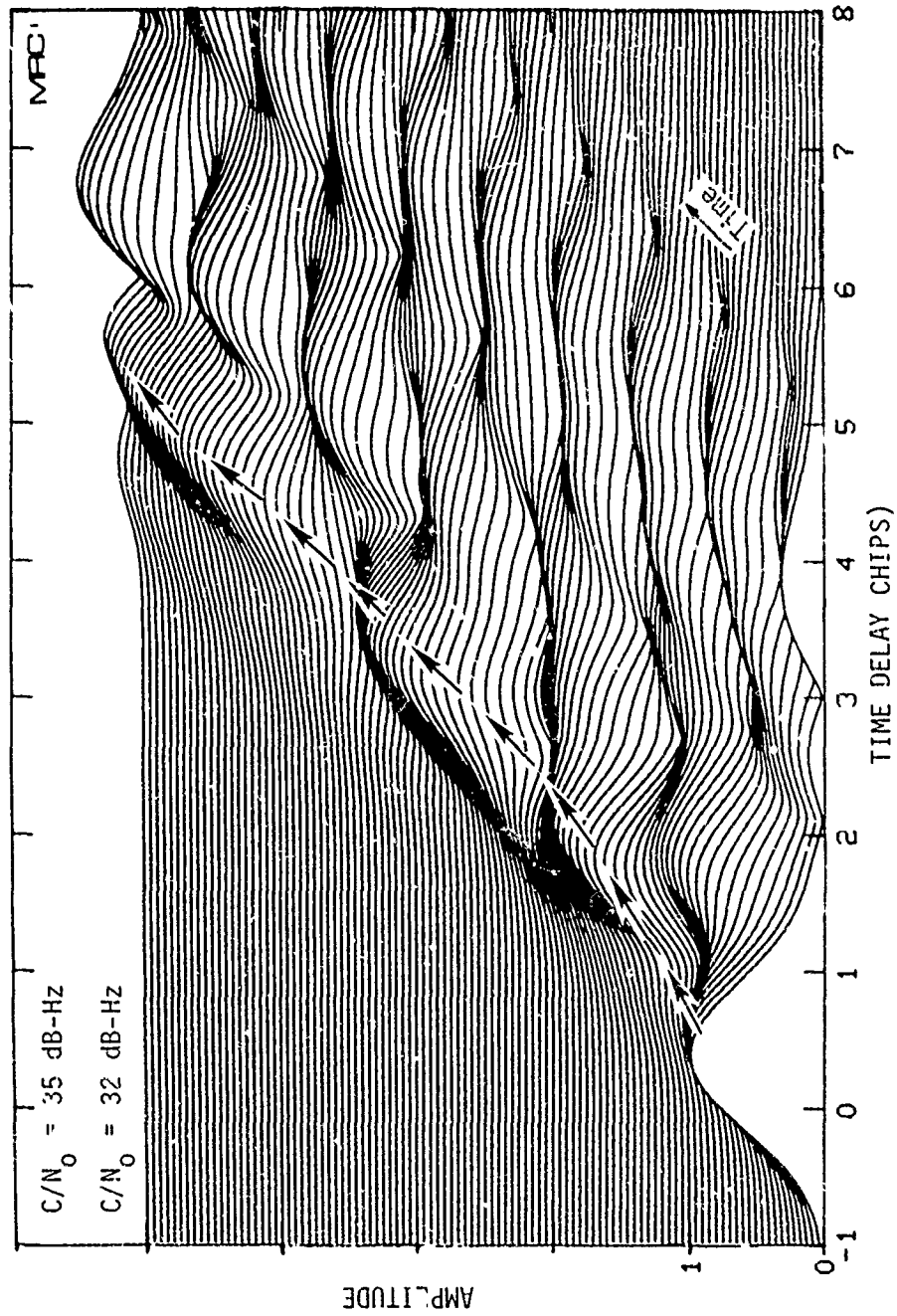


Figure 4-26. Esther at 150 MHz: PN code envelope and code tracking history for simulation time from 13.93 to 14.66 seconds.

about 0.3 chips throughout the 0.73 seconds of simulation time shown. For the 32 dB-Hz  $C/N_0$  case, erroneous Doppler aiding from the AFC/Costas loop has caused the code loop to lock onto a sidelobe at around 1.3 to 1.5 chips time delay.

In Figure 4-25, at a simulation time interval from 10.26 to 10.99 sec, the X-set operating at a mean  $C/N_0$  value of 35 dB-Hz is tracking the peak quite well. At  $C/N_0$  of 32 dB-Hz, the receiver is still recovering from the extended 5 second period during which the code loop was tracking a correlation sidelobe.

A little later in the 15 second simulation, the code loop reacquires the peak and each of the two values of  $C/N_0$  give the same code tracking performance. During the brief interval shown in Figure 4-26, the X-set operation at 32 dB-Hz  $C/N_0$  is comparable to the operation at 35 dB-Hz, at least as far as frequency and code tracking is concerned.

Other measures of X-set performance are also degraded at the lower value of mean  $C/N_0$ . During the 15 second simulation interval, 25 30-bit words are received and decoded using the (32,26) Hamming code described in Reference 4-6. For a  $C/N_0$  value of 35 dB-Hz, 16 of the 25 words are received with one or more bit errors, giving a word error rate of 0.64. For the lower  $C/N_0$  value of 32 dB-Hz, only one word is received free of errors, for a word error rate of 0.96. For 35 dB-Hz mean  $C/N_0$  the rms time-delay error is 0.37 chips corresponding to a position error of 10.8 meters (1 chip of the 10.23 Mbps P code equals approximately 29.305 meters); for the 32 dB-Hz mean  $C/N_0$  case the rms time-delay error is 0.92 chips corresponding to a position error of 26.96 meters.

Similar 15 second simulations were performed with the 50/sec AFC/Costas loop iteration rate for mean  $C/N_0$  values of 44, 38, and 32 dB-Hz. For this lower iteration rate with worse phase and frequency tracking performance than the 250/sec rate, loss of frequency lock in the AFC/Costas

loop was found to drive the code loop out of lock because of the Doppler aiding applied in the code loop. All three values of  $C/N_0$  exhibited this same loss of frequency and code lock condition. No effort was made to investigate code reacquisition in this work.

#### 4.3.3 X-Set Performance at 200 MHz

Three 15 second simulations at a carrier frequency of 200 MHz were performed for the same barium model of Esther (without the deterministic cloud) as those described in Section 4.3.2. X-set performance was investigated for a value of mean  $C/N_0$  of 35 dB-Hz with AFC/Costas iteration rates of 250/sec and 50/sec, and for a mean  $C/N_0$  value of 32 dB-Hz with an iteration rate of 250/sec. In general, code tracking performance was quite good, with no problems for the higher iteration rate at either value of  $C/N_0$ . For the slower 50/sec AFC/Costas iteration rate, incorrect Doppler aiding from the frequency tracking loop drove the code loop briefly out of lock twice, but recovery occurred rapidly each time. For the 250/sec iteration rate the word error rates were 0.48 and 0.64 for  $C/N_0$  of 35 dB-Hz and 32 dB-Hz, respectively. For the 50/sec iteration rate at a mean  $C/N_0$  value of 35 dB-Hz, the word error rate was 0.68.

#### 4.3.4 Summary of X-Set Performance

In addition to the results discussed in the preceding subsections, simulations also have been performed for carrier frequencies of 150, 200, and 250 MHz for the full barium models of both Esther and Iern (deterministic barium cloud included) with an effective inner scale of 0.58 m. For these cases, the major effect of the deterministic cloud is to cause large scale defocusing which acts to reduce the signal level in the central region immediately below the center of the cloud. (See Figures 4-8 through 4-14.) This defocusing is, of course, equivalent to a reduction in the mean  $C/N_0$  level and causes a resulting degradation in X-set performance. For these

six simulations and the previously described simulation results, it is found that loss of code lock or degraded code tracking was usually caused by erroneous Doppler aiding from the AFC/Costas loop. Even with good code tracking, Costas phase tracking and data demodulation is severely degraded in the barium environment with word error rates for the 30-bit navigation data word found to be as large as 0.6 to 1.0.

In the operational Global Positioning System, large error rates may be tolerable because of redundant transmission of data frames every 30 seconds. Perhaps a more important consideration is the undetected error rate. With the GPS (32,26) Hamming code and receiver parity check algorithm, very few words with errors pass the parity check. Hence the undetected error rate is quite low. Of the 350 words transmitted during 210 seconds of simulation time here only one word incorrectly passed the receiver parity check.

## REFERENCES

- 4-1. Knepp, D. L., Multiple Phase-Screen Propagation Analysis for Defense Satellite Communications System, DNA 4424T, MRC-R-332, Mission Research Corporation, September 1977.
- 4-2. Briggs, B. H., and I. A. Parkin, "On the Variation of Radio Star and Satellite Scintillations with Zenith Angle," J. Atmos. Terr. Phys. Vol. 25, pp. 339-365, 1963.
- 4-3. Bogusch, R. L., and D. L. Knepp, Propagation Effects on GPS Receiver Model X, Mission Research Corporation, January 1978 (Unpublished).
- 4-4. System Specification for the NAVSTAR Global Positioning System—Phase 1, SS-GPS-101B, SAMSO/YEN, 30 December 1975.
- 4-5. System Segment Specification for the Space Vehicle System Segment of the NAVSTAR Global Positioning System—Phase I, SS-SVS-101A, SAMSO/YEN, February 1975.
- 4-6. Space Vehicle Navigation Subsystem and NTS PRN Navigation Assembly/ User System Segment and Monitor Station, ICD MH08-00002-400, Rev. E, Prepared by Rockwell International for SAMSO/YE, September 1975.
- 4-7. Stonestreet, W. M., A Functional Description of the NAVSTAR GPS Receiver Model X, R-981, The Charles Stark Draper Laboratory, Inc., Final Report for SAMSO Contract FO4701-75-C-0212, Volume 1, 26 April 1976, Revised February 1977.
- 4-8. Cahn, C. R., A Composite AFC/Costas Loop for Transition Between Frequency and Phase Tracking, Magnavox Research Laboratories Technical Report, MX-TM-3165-75, 24 January 1975.
- 4-9. Technical discussions with the GPS JPO and Aerospace Inc., arranged by J. Luse of SAMSO/YE, 9 August 1977.

## SECTION 5

### SUMMARY AND RECOMMENDATIONS

In this work, results have been presented for the performance of the GPS X-set receiver operating in a striated barium environment at carrier frequencies from 150 to 250 MHz. These results were obtained as a simulation of an airborne receiver passing beneath a barium cloud and flying perpendicular to the projection of the striations at a velocity component of 250 m/sec. The barium cloud striations were represented by a statistical model obtained from the analysis of back-propagation results from the STRESS barium release experiment.

The receiver simulation results presented here, together with earlier studies of X-set performance in a disturbed environment (Reference 5-1), give reliable predictions of X-set operation in both nonselective and severe frequency-selective propagation environments. Detailed simulation examples, showing the complex interaction between the coupled X-set AFC/Costas and code tracking loops, have been presented. At a carrier frequency of 150 MHz, the X-set, with 250/sec AFC/Costas iteration rate, performs the critical function of tracking the PN code quite well. However, erroneous Doppler aiding from the frequency tracking loop can force loss of code lock for mean carrier power-to-noise density ratios below about 35 dB-Hz. Word error rates for the 30-bit navigation data words are found to be as large as 0.6 to 1.0, even with good code tracking.

Because of problems associated with the transmittal of large amounts of propagation results required for the frequency-selective receiver simulation, it was difficult to obtain X-set simulation results of sufficiently

long duration for statistical significance. This difficulty has been alleviated and future work should include the compilation of more results for X-set performance. Further predictions should be made for a carrier frequency of 100 MHz with consideration of the planned PLACES rocket geometry.

Work is currently in progress to relate the propagation calculations presented here to analytical results for mean time delay, time delay jitter, and broadening of the received waveform. These issues will be addressed in a separate report.

#### REFERENCES

- 5-1. Bogusch, R. L., and D. L. Knepp, Propagation Effects on GPS Receiver Model X, Mission Research Corporation, January 1978 (Unpublished).

## DISTRIBUTION LIST

### DEPARTMENT OF DEFENSE

Assistant Secretary of Defense  
Comm., Cmd, Cont., & Intell  
ATTN: Dir of Intelligence Systems, J. Babcock  
ATTN: C3IST&CCS, M. Epstein

Assistant to the Secretary of Defense  
Atomic Energy  
ATTN: Executive Assistant

Defense Advanced Rsch. Proj. Agency  
ATTN: TIO

Defense Communications Engineer Center  
ATTN: Code R410, P. Craighill  
ATTN: Code R720, J. Worthington  
ATTN: Code R123

Defense Nuclear Agency  
ATTN: DDST  
ATTN: STVL  
3 cy ATTN: RAAE  
4 cy ATTN: TITL

Defense Technical Information Center  
12 cy ATTN: DD

Field Command  
Defense Nuclear Agency  
ATTN: FCPR

Field Command  
Defense Nuclear Agency  
Livermore Division  
ATTN: FCPRL

Undersecretary of Defense for Rsch. & Engrg.  
ATTN: Strategic & Space Systems (OS)

WWMCCS System Engineering Org.  
ATTN: R. Crawford

### DEPARTMENT OF THE ARMY

BMD Advanced Technology Center  
Department of the Army  
ATTN: ATC-R, D. Russ  
ATTN: ATC-O, W. Davies  
ATTN: ATC-T, M. Capps

Harry Diamond Laboratories  
Department of the Army  
ATTN: DELHD-N P

U.S. Army Nuclear & Chemical Agency  
ATTN: Library

U.S. Army Satellite Comm. Agency  
ATTN: Document Control

### DEPARTMENT OF THE NAVY

Joint Cruise Missile Project Office  
Department of the Navy  
ATTN: JCM-G-70

### DEPARTMENT OF THE NAVY (Continued)

Naval Ocean Systems Center  
ATTN: Code 532, J. Bickel  
ATTN: Code 5322, M. Paulson  
3 cy ATTN: Code 5324, W. Moler

Naval Research Laboratory  
ATTN: Code 6700, T. Coffey  
ATTN: Code 7500, B. Wald  
ATTN: Code 6780, S. Ossakow  
ATTN: Code 7550, J. Davis

Naval Surface Weapons Center  
ATTN: Code F31

Office of Naval Research  
ATTN: Code 465  
ATTN: Code 421  
ATTN: Code 420

Strategic Systems Project Office  
Department of the Navy  
ATTN: NSP-43  
ATTN: NSP-2141  
ATTN: NSP-2722, F. Wimberly

### DEPARTMENT OF THE AIR FORCE

Air Force Avionics Laboratory  
ATTN: AAD, W. Hunt  
ATTN: AAD, A. Johnson

Air Force Geophysics Laboratory  
ATTN: OPR-1, J. Ulick  
ATTN: PHP, J. Aarons  
ATTN: LKB, K. Champion  
ATTN: OPR, A. Stair  
ATTN: OPR, H. Gardiner  
ATTN: PHI, J. Buchau  
ATTN: PHP, J. Mullen

Air Force Weapons Laboratory  
ATTN: SLE  
ATTN: DYC

Assistant Chief of Staff  
Studies & Analyses  
Department of the Air Force  
ATTN: AF/SASC, G. Zank  
ATTN: AF/SASC, W. Adams

Ballistic Missile Office  
Air Force Systems Command  
ATTN: MNHL  
ATTN: MNH, M. Baran

Deputy Chief of Staff  
Operations Plans and Readiness  
Department of the Air Force  
ATTN: AFXOKT  
ATTN: AFXOXFD  
ATTN: AFXOKS  
ATTN: AFXOKCD

DEPARTMENT OF THE AIR FORCE (Continued)

Deputy Chief of Staff  
Research, Development, & Acq.  
Department of the Air Force  
ATTN: AFRDS  
ATTN: AFRDQ  
ATTN: AFRDSS  
ATTN: AFRDSP

Electronic Systems Division  
Department of the Air Force  
ATTN: DCKC, J. Clark

Electronic Systems Division  
Department of the Air Force  
ATTN: XRW, J. Deas

Electronic Systems Division  
Department of the Air Force  
ATTN: YSEA  
ATTN: YSM, J. Kobelski

Headquarters Space Division  
Air Force Systems Command  
ATTN: E. Butt

Strategic Air Command  
Department of the Air Force  
ATTN: DCX  
ATTN: XPFS  
ATTN: OOKSN  
ATTN: DCXT  
ATTN: DCXF  
ATTN: NRT  
ATTN: DCXT, T. Jorgensen

DEPARTMENT OF ENERGY CONTRACTORS

Los Alamos Scientific Laboratory  
ATTN: Document Control for D. Simons

Sandia Laboratories  
ATTN: Document Control for Space Project Div.  
ATTN: Document Control for Org. 1250, W. Brown  
ATTN: Document Control for 3141  
ATTN: Document Control for D. Dahlgren  
ATTN: Document Control for Org. 4241, T. Wright  
ATTN: Document Control for D. Thornbrough

EG&G, Inc.  
ATTN: Document Control for D. Wright  
ATTN: Document Control for J. Colvin

DEPARTMENT OF DEFENSE CONTRACTORS

Aerospace Corp.  
ATTN: N. Stockwell  
ATTN: V. Josephson  
ATTN: D. Olsen  
ATTN: I. Garfunkel  
ATTN: T. Salmi  
ATTN: S. Bower  
ATTN: F. Morse  
ATTN: R. Slaughter

Physical Dynamics, Inc.  
ATTN: E. Fremouw

DEPARTMENT OF DEFENSE CONTRACTORS (Continued)

BDM Corp.  
ATTN: L. Jacobs  
ATTN: T. Neighbors

Berkeley Research Associates, Inc.  
ATTN: J. Workman

Comsat Labs  
ATTN: R. Taur  
ATTN: G. Hyde

Electrospace Systems, Inc.  
ATTN: H. Logston

ESL, Inc.  
ATTN: J. Marshall  
ATTN: C. Prettie  
ATTN: J. Roberts

General Electric Company—TEMPO  
ATTN: W. Knapp  
ATTN: T. Stevens  
ATTN: W. McNamara  
ATTN: M. Stanton  
ATTN: DASIAC  
ATTN: D. Chandler

General Research Corp.  
ATTN: J. Garbarino  
ATTN: J. Ise, Jr.

IBM Corp.  
ATTN: F. Ricci

University of Illinois  
ATTN: K. Yeh

Institute for Defense Analyses  
ATTN: J. Bengston  
ATTN: H. Wolfhard  
ATTN: E. Bauer  
ATTN: J. Aein

M.I.T. Lincoln Lab  
ATTN: L. Laughlin  
ATTN: D. Towle

Mission Research Corp.  
ATTN: F. Fajen  
ATTN: D. Sowle  
ATTN: R. Kilb  
ATTN: R. Bogusch  
ATTN: R. Hendrick  
ATTN: S. Gutsche  
ATTN: D. Sappenfield  
ATTN: D. Knepp  
5 cy ATTN: Document Control

Mitre Corp.  
ATTN: C. Callahan  
ATTN: B. Adams  
ATTN: A. Kymel  
ATTN: G. Harding

R&D Associates  
ATTN: L. Delaney  
ATTN: B. Yoon

DEPARTMENT OF DEFENSE CONTRACTORS (Continued)

Mitre Corp.

ATTN: M. Horrocks  
ATTN: W. Foster  
ATTN: W. Hall  
ATTN: J. Wheeler

R&D Associates

ATTN: R. Turco  
ATTN: C. Greifinger  
ATTN: W. Karzas  
ATTN: B. Gabbard  
ATTN: W. Wright, Jr.  
ATTN: M. Gantsweg  
ATTN: C. MacDonald  
ATTN: F. Gilmore  
ATTN: H. Ory  
ATTN: R. Lelevier

DEPARTMENT OF DEFENSE CONTRACTORS (Continued)

Rand Corp.

ATTN: C. Crain  
ATTN: E. Bedrosian

Science Applications, Inc.

ATTN: D. Sachs  
ATTN: L. Linson

Science Applications, Inc.

ATTN: D. Divis

SRI International

ATTN: W. Chesnut  
ATTN: C. Rino  
ATTN: A. Burns